**U.S. Department of Energy**
**FreedomCAR and Vehicle Technologies, EE-2G**
**1000 Independence Avenue, S.W.**
**Washington, D.C. 20585-0121**

*FY 2006*

# FREEDOMCAR
# ADVANCED TRACTION DRIVE MOTOR DEVELOPMENT
# PHASE I

***Prepared by:***

**Oak Ridge National Laboratory**

**Mitch Olszewski, Program Manager**

***Submitted to:***

Energy Efficiency and Renewable Energy
FreedomCAR and Vehicle Technologies
Vehicle Systems Team

Susan A. Rogers, Technology Development Manager

September 2006

ORNL/TM-2006/UQM

UQM Technologies, Inc.

*-Final Report Submitted to-*
**Oak Ridge National Laboratories**

# FreedomCAR Advanced Traction Drive Motor Development Phase I

Josh Ley
Jon Lutz
UQM Technologies, Inc.

Revision 1 Draft Release 6-27-06
Revision 2, 8-04-06

## TABLE OF CONTENTS

## LIST OF TABLES

**Tables:**

## LIST OF FIGURES

**Figures:**

# 1. INTRODUCTION

## 1.1 BACKGROUND

The overall objective of this program is to design and develop an advanced traction motor that will meet the FreedomCAR and Vehicle Technologies (FCVT) 2010 goals and the traction motor technical targets. The motor specifications are given in Section 1.3. Other goals of the program include providing a cost study to ensure the motor can be developed within the cost targets needed for the automotive industry. The program has focused on using materials that are both high performance and low costs such that the performance can be met and cost targets are achieved. In addition, the motor technologies and machine design features must be compatible with high volume manufacturing and able to provide high reliability, efficiency, and ruggedness while simultaneously reducing weight and volume. Weight and volume reduction will become a major factor in reducing cost, material cost being the most significant part of manufacturing cost at high volume.

Many motor technology categories have been considered in the past and present for traction drive applications, including: brushed direct current (DC), PM (PM) brushless dc (BLDC), alternating current (AC) induction, switched reluctance and synchronous reluctance machines. Of these machine technologies, PM BLDC has consistently demonstrated an advantage in terms of power density and efficiency. As rare earth magnet cost has declined, total cost may also be reduced over the other technologies. Of the many different configurations of PM BLDC machines, those which incorporate power production utilizing both magnetic torque as well as reluctance torque appear to have the most promise for traction applications. There are many different PM BLDC machine configurations which employ both of these torque producing mechanisms: however, most would fall into one of two categories—some use weaker magnets and rely more heavily on reluctance torque (reluctance-dominant PM machines), others use strong PMs and supplement with reluctance torque (magnet-dominant PM machines). This report covers a trade study that was conducted in this phase I program to explore which type of machine best suits the FCVT requirements.

## 1.2 SUMMARY

Over the course of this program, UQM Technologies, Inc. (UQM) narrowed in on a propulsion motor design that meets and in many cases exceeds the FCVT 2010 technical targets for electrical machines and advanced propulsion motors. The program began with a trade study of three different motor configuration categories as well as a cost study for the evaluation of magnet prices across the spectrum of NdFeB magnet materials. Both of these studies pointed toward the selection of a magnet-dominant internal PM (IPM) design configuration with supplemental reluctance torque. A major lesson learned was that taking advantage of as much magnetic torque and reluctance torque as possible leads to the most compact motor design for a given set of specifications. A more compact design reduces space claim and overall material cost of the motor. Since weaker magnets lead to lower magnetic torque, there is no reason to use weaker magnets than what is necessary to survive at the required operating temperatures. Also, optimizing the shape of flux barriers and minimizing bridge sizes leads to high levels of reluctance torque even with a single flux barrier, sintered magnet machine. Table 1 summarizes the relevant predicted quantities for the FCVT motor design that is a result of the efforts to design a motor to meet the FCVT requirements. The FCVT motor requirement and targets are listed in full in the next section. In Table 1, the FCVT target/requirement is listed next to the predicted value for the FCVT design. For reference, the section in this report that discusses the analysis that led to each of these predictions is also listed in Table 1.

**Table 1. Summary of predicted quantities for FCVT motor design**

| Description | Predicted Quantity | Target/Requirement | Analysis Section |
|---|---|---|---|
| Peak power | 55–110 kW (1) | 55 kW | 6.4 |
| Duration at 55 kW | 40 s | 18 s | 6.6.2 |
| Continuous power | 30 kW | 30 kW | 6.6.1 |
| **Quantities Based on Active Materials** | | | |
| Power density (based on 55 kW) | 11–15.8 kW/Liter (2) | >12.5 kW/Liter | 6.8 |
| Power density (based on 110 kW) | 22–31.6 kW/Liter (2) | >12.5 kW/Liter | 6.8. 6.4 |
| Specific power (based on 55 kW) | 3 kW/kg | >2.75 kW/kg | 6.8 |
| Specific power (based on 110 kW) | 6 kW/kg | >2.75 kW/kg | 6.8. 6.4 |
| Cost per kW (based on 55 kW) | 3.4–6.8 $/kW | <$3.2/kW | 8 |
| Cost per kW (based on 110 kW) | 1.7–3.4 $/kW | <$3.2/kW | 8 |
| **Quantities Based on Full Motor Package** | | | |
| Power density (based on 55 kW) | 6.6 kW/Liter | >5 kW/Liter | 7 |
| Power density (based on 110 kW) | 13.3 kW/Liter | >5 kW/Liter | 7 |
| Specific power (based on 55 kW) | 1.74 kW/kg | >1.3 kW/kg | 7 |
| Specific power (based on 110 kW) | 3.47 kW/kg | >1.3 kW/kg | 7 |
| Cost per kW (based on 55 kW) | 5–9.5 $/kW (3) | <$7/kW | 8 |
| Cost per kW (based on 110 kW) | 2.5–4.8 $/kW (3) | <$7/kW | 8 |
| **Other Motor Requirements** | | | |
| Maximum current | 400 Arms | 400 Arms | 6.2 |
| back-EMF | 480 V | <600 V | 5.4. 6 |
| Efficiency | 94.8–96.5% | >93% | 5.4 |
| Characteristic current | 344.6 Arms | <400 Arms | 5.4 |
| Maximum coolant temperature | 105 C | 105 C | 6.6 |

(1) Peak power is 55 kW at 2000 rpm, 82.5 kW at 3000 rpm, and 110 kW at 4000 rpm
(2) The low end of the range is based on the most conservative volume calculation and the high end of the range is based on the least conservative volume calculation explained in Fig. 4.
(3) Range refers to the cost at 100k/yr to the cost at 1M/yr quantities.

It is explained in Section 6.4, that although 55 kW is the peak power at 2000 rpm, the base speed can be increased to provide up to 110 kW of peak power. For this reason, some of the quantities in Table 1 have been calculated using 55 kW as well as 110 kW, the actual peak power.

## 1.3 FCVT MOTOR SPECIFICATIONS

Tables 2 and 3 are from the solicitation for the Advanced Traction Motor Development program have been reproduced from the original document and provided in this section for reference. All aspects of this program were focused on meeting or exceeding the requirements listed in these tables. As the analysis and results are discussed in the later sections of this report, these tables are referenced to illustrate how the results compare to the specifications.

**Table 2. FCVT performance goals and targets for a 2010 electric propulsion system**

| **FreedomCAR Goals** | |
|---|---|
| Peak Power | 55 kW for 18 seconds |
| Continuous Power | 30 kW |
| Lifetime | > 15 years or 150,000 miles |
| Cost | < $12/peak kW (< $660) |
| **FreedomCAR Technical Targets** | |
| Peak Power to Weight Ratio | > 1.2 kW/kg (< 46 kg) |
| Peak Power to Volume Ratio | > 3.5 kW/liter (< 16 liters) |
| Efficiency (10 to 100% speed at 20% rated torque) | > 90% |

**Table 3. FCVT technical targets for power electronics and electric machines**

| **Power Electronics (inverter and controller)** | **2010 Target** |
|---|---|
| Peak Power to Weight Ratio (kW/kg) | > 12 |
| Peak Power to Volume Ratio (kW/liter) | > 12 |
| Cost/Peak Power ($/kW) | < 5 |
| Efficiency (%) | 97 |
| Coolant Inlet Temperature (°C) | 105 |
| Lifetime (years) | 15 |
| **Traction Motor** | **2010 Target** |
| Peak Power to Weight Ratio (kW/kg) | > 1.3 |
| Peak Power to Volume Ratio (kW/liter) | > 5 |
| Cost/Peak* ($/kW) | < 7 |
| Efficiency (%) | > 93 @ 10% to 100% of max. speed |
| Nominal Voltage (volts) | 325 |
| Maximum Current ($A_{rms}$) | 400 |

(*Includes active material, motor gears, and housing)

Table 4 reiterates the advanced traction motor specifications for the FCVT motor design and development program. The motor design generated in this program was designed specifically to meet or exceed the metrics listed in this table.

**Table 4. Advanced traction motor specifications**

| Requirement | Target Specification |
|---|---|
| Minimum top speed (rpm) (see note 2) | 10,000 |
| Peak power at 20% of maximum speed for 18 seconds and nominal voltage (kW) | 55 |
| Continuous power at 20–100% of maximum speed and nominal voltage (kW) (see note 1) | 30 |
| Battery operating voltage (Vdc) | Nominal: 325<br>Range: 200–450 |
| Maximum current at motor (A) | 400 |
| Characteristic current ($\psi_{mag}/L_d$) (A) (see note 2) | < Maximum Current |
| Efficiency at 10–100% of maximum speed for 20% of rated torque (final check: may use FTP-75 or equivalent drive cycle) | > 93 |
| Back-electromotive force (EMF) at 100% of maximum speed, peak line-to-line voltage (V) (see note 3) | < 600 |
| Torque pulsations – not to exceed at any speed, percent of peak torque (%) | < 5 |
| Peak power to weight ratio for active materials (see note 4) only (kW/kg) | > 2.75 |
| Peak power to volume ratio for active materials (see note 4) only (kW/liter) | > 12.5 |
| Life (years) | > 15 |
| Motor cost of active materials at peak power ($/kW) | < 3.2 |
| Ambient (outside container) operating temperature (°C) | -40 to +105 |
| Storage temperature (°C) | -50 to +125 |
| Coolant inlet temperature (°C) | 105 |
| Maximum coolant flow rate (liters/min) | 10 |
| Maximum coolant pressure drop (psi) | 2 |
| Maximum coolant inlet pressure (psi) | 20 |
| Minimum isolation impedance – terminal to ground (M ohm) | 1 |
| Minimum insulation impedance – terminal to ground (M ohm) | 20 |

Table Notes: (1) address scalability issues in your proposal for motors rated between 20 kW and 70 kW continuous power; (2) alternative approaches will be considered if system requirements and targets are met; (3) higher values may be considered if system requirements are met; and (4) active material consists of stator core, rotor core, stator windings and magnets.

Table 4 states that the motor must make 55 kW of power for at least 18 seconds at 20% of maximum speed (2000 rpm) to the maximum speed (10 krpm). This translates to 262.65 Nm of peak torque at 2000 rpm and below. Figure 1 interprets this specification graphically to give a peak operating profile in terms of torque vs. speed and power vs. speed.

UQM initially interpreted this peak operating profile (Fig. 1) to be required at 325 V supply and above. However, UQM later learned that this interpretation was incorrect and peak power is necessary across the entire voltage range, down to 200 V. Peak power operation at 200 V, while operating under 400 Arms of leg current, became a driving design specification for the motor development effort. Vector analysis discussed in later sections was used to determine if 200 V operation was possible at many different points along this operating curve.

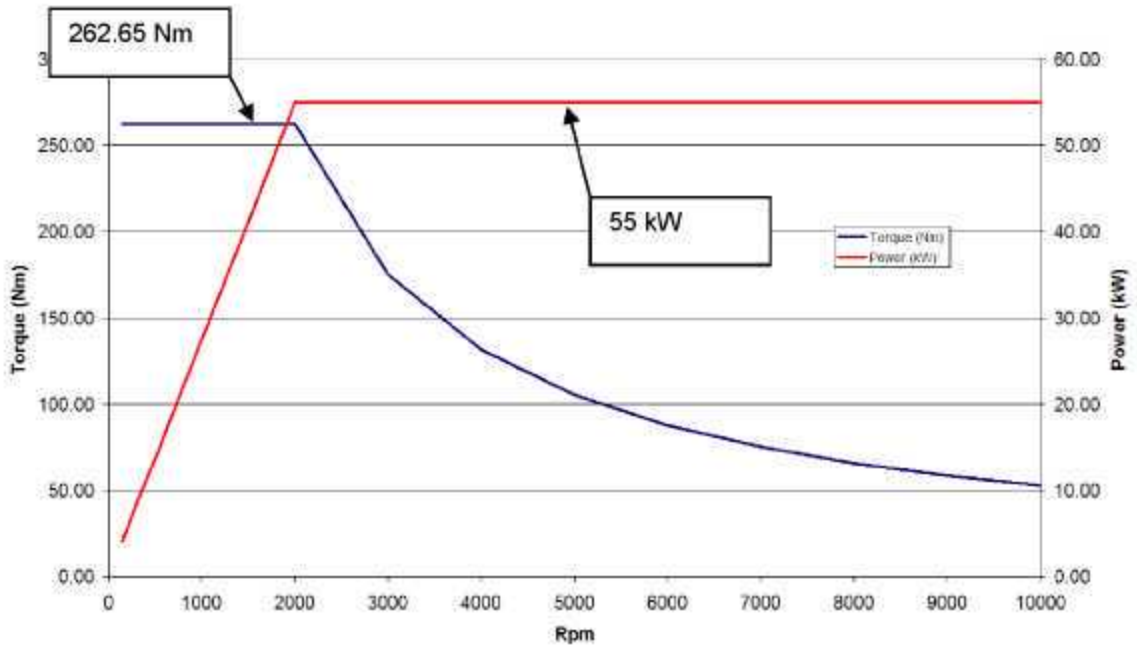


**Fig. 1. Peak operating profile, FCVT specification.**

Table 4 also states that the motor must produce 30 kW from 20–100% of maximum speed on a continuous basis. Figure 2 illustrates the interpreted operating profile for continuous motor operation.

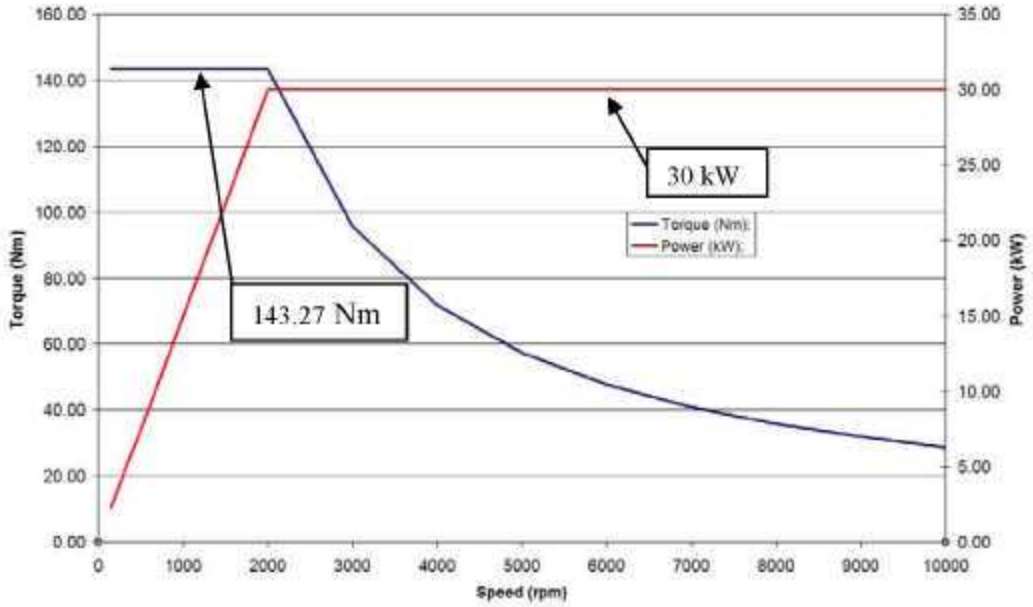


**Fig. 2. Operating profile for continuous operation.**

The requirement for efficiency states that the machine must be over 93% efficient at 20% of its rated torque (20% of 262 Nm = 52 Nm) from 10–100% of maximum speed or from 1000 rpm to 10 krpm.

During development, all of the efficiency data was calculated for evaluation at this 52 Nm operating requirement between 1000 rpm and 10 krpm as shown in Fig. 3.

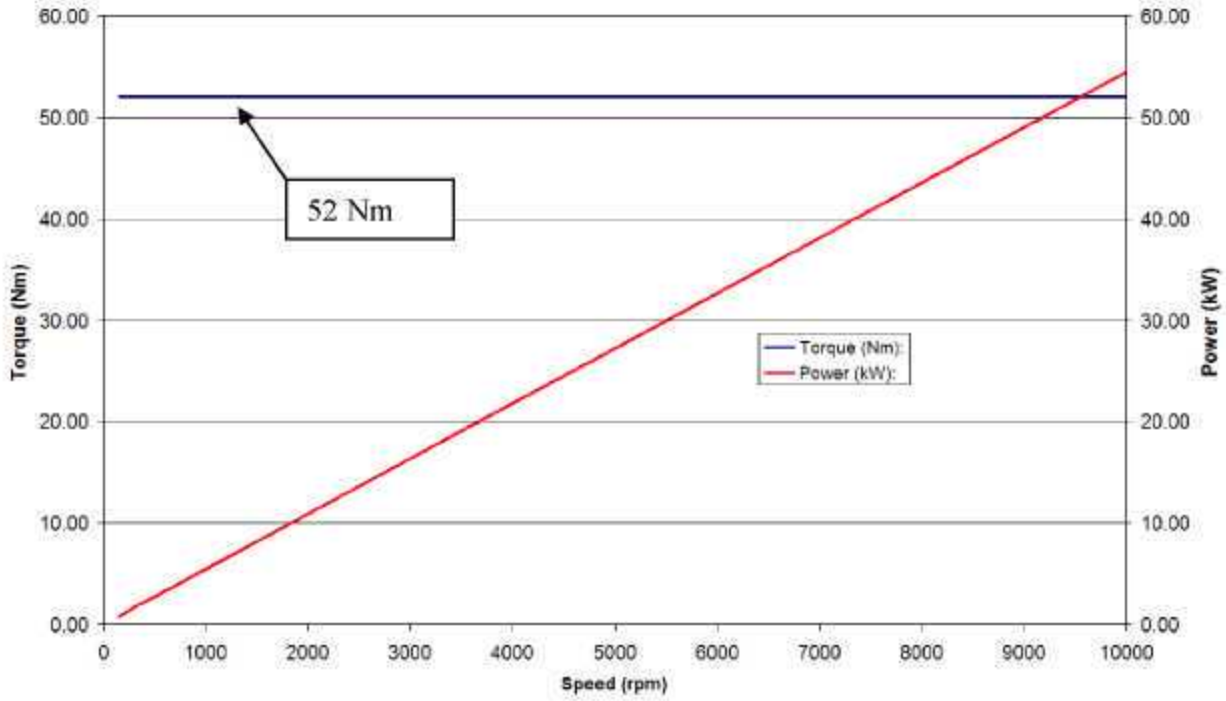


**Fig. 3. Operating profile for efficiency requirements.**

## 1.4 VOLUME CALCULATIONS FOR POWER AND TORQUE DENSITY

Due to the fact that power density >12.5 kW/L is a specification in Table 4, it necessary to clarify how volume is calculated to avoid confusion. The power density specification in this table refers to a note which defines the active materials of a motor, "(4) active material consists of stator core, rotor core, stator windings and magnets." Due to the fact that the calculation of volume for these active materials can be interpreted in several different ways, we decided to illustrate what we believe to be the most conservative and the least conservative volume calculations.

The most conservative volume calculation consists of calculating the volume of a simple cylinder which has a diameter to the outer diameter of the stator and a length over the end-turns of the winding. This is considered to be a most conservative interpretation because it encompasses some air around the end-turns and in the center of the rotor, which obviously are not considered active materials. Because this calculation is simple, we chose this method to evaluate early iterations and design comparisons.

The least conservative volume calculation consists of adding the volume of three torriods (donut shapes). Two of the torroids are composed of the end-turns on each end. The last torroid is the volume from the inner diameter of the rotor to the outer diameter of the stator, bounded axially by the stack length. This method does not involve subtracting the volume of the air inside the air gap; however, the volume inside the air gap would be minimal (see Fig. 4). This method is probably the most fitting interpretation of the specifications because it is more representative of the actual active materials. The volumes and power density for both methods have been calculated for the final design.

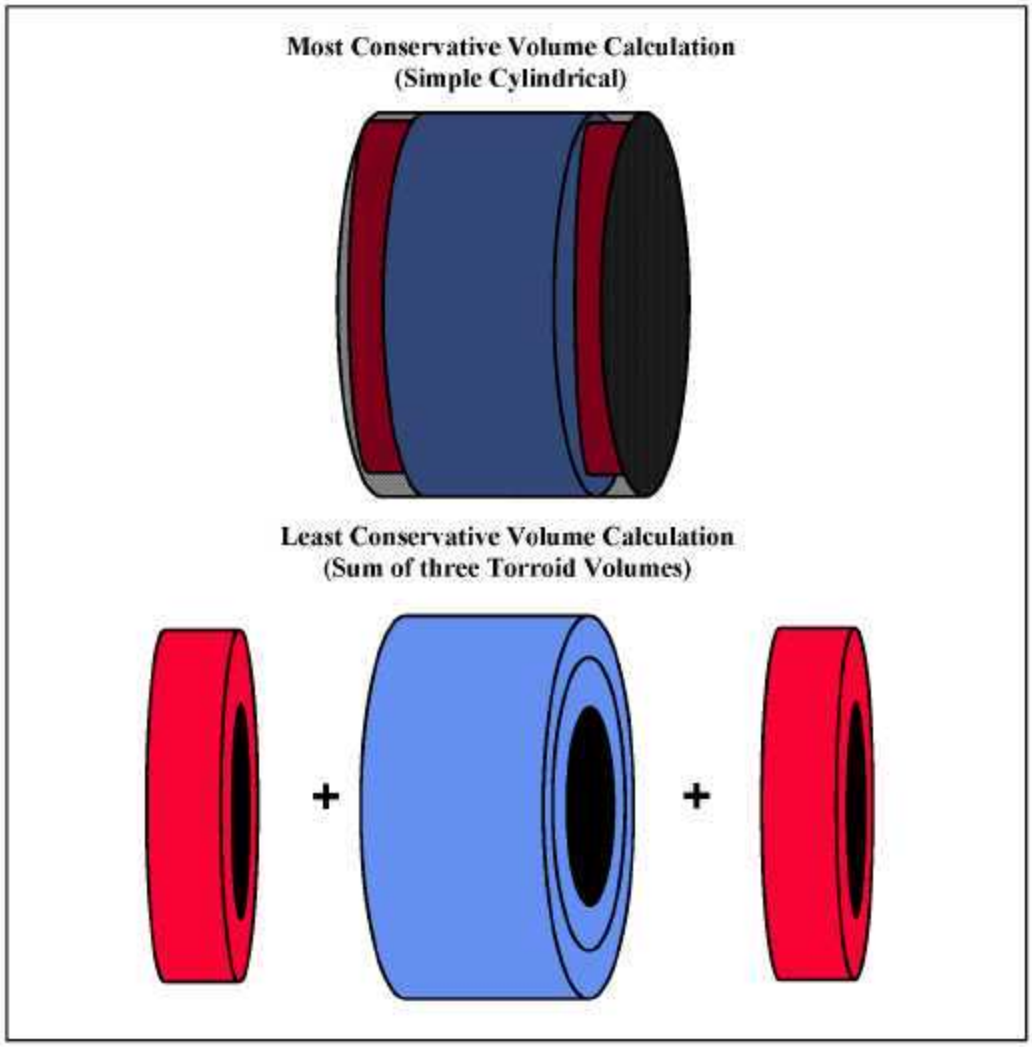


**Fig. 4. Volume calculations.**

# 2. THREE DESIGN TRADE STUDY

## 2.1 DESCRIPTION OF THE THREE DESIGN TOPOLOGIES

The purpose of the three design trade study was to determine the motor configuration that is best suited to meet the motor requirements for the FCVT advanced traction motor specifications discussed in Section 1.3. The three motor configurations that were evaluated in this trade study are a magnet-dominant internal PM machine (IPM), a reluctance-dominant IPM, and a surface-mounted PM machine. The geometry and characteristics of each machine design were chosen based on motors currently being produced in industry and published motor design papers. Some of the defining characteristics for these motor configurations as implemented in this trade study are as follows….

Magnet-dominant IPM Characteristics, see Fig. 5(C)

1. Utilizes strong PMs such as sintered NdFeB embedded in the rotor such that saliency is achieved. (Br = 1.15 T magnets were chosen for this trade study.)
2. The rotor configuration for this study was modeled based on the Prius motor with a single V-shaped flux barrier and with two magnets per pole embedded in the rotor.
3. The stator configuration was also modeled from the Prius motor with four-pole pairs and six slots per pole.

Reluctance-dominant IPM Characteristics, see Fig. 5(B)…

1. Utilizes weak PMs that can be molded into complex shapes, such as bonded NdFeB magnets. These magnets are assumed to be molded into flux barriers that hold complex shapes. (The properties of a typical bonded NdFeB magnet were used for the design, Br = 0.6 T.)
2. The stator configuration also has four-pole pairs and six slots per pole.
3. High reluctance designs generally tend to have multiple flux barriers to maximize reluctance torque and utilize more magnet material. This design configuration has three flux barriers.

Surface-mounted Motor Characteristics, see Fig. 5(A)…

1. Utilizes strong PMs such as sintered NdFeB, placed on the outer diameter of the rotor, and contained with a nonmagnetic sleeve that retains them on the machine. (Br = 1.15 T magnets were chosen for this trade study.)
2. A higher pole count, eight-pole pairs and three slots per pole, was chosen to make up for the fact that reluctance torque will not be significant with this machine configuration.

Some characteristics common to each design in the trade study include:

1. The properties of nonoriented 29 gage (.014) M19 steel were assumed for the rotor and stator.
2. The overall wire fill factor was held constant at 77% based on the square area over the outer insulation of the wire. This is an aggressive fill factor; however, less than 82% is estimated for the Prius motor.
3. For each winding, 24 gage inverter grade wire was assumed. The appropriate number of conductors per turn and the number of turns varied between the designs, but each design conformed to the 77% fill factor assumption in (2).

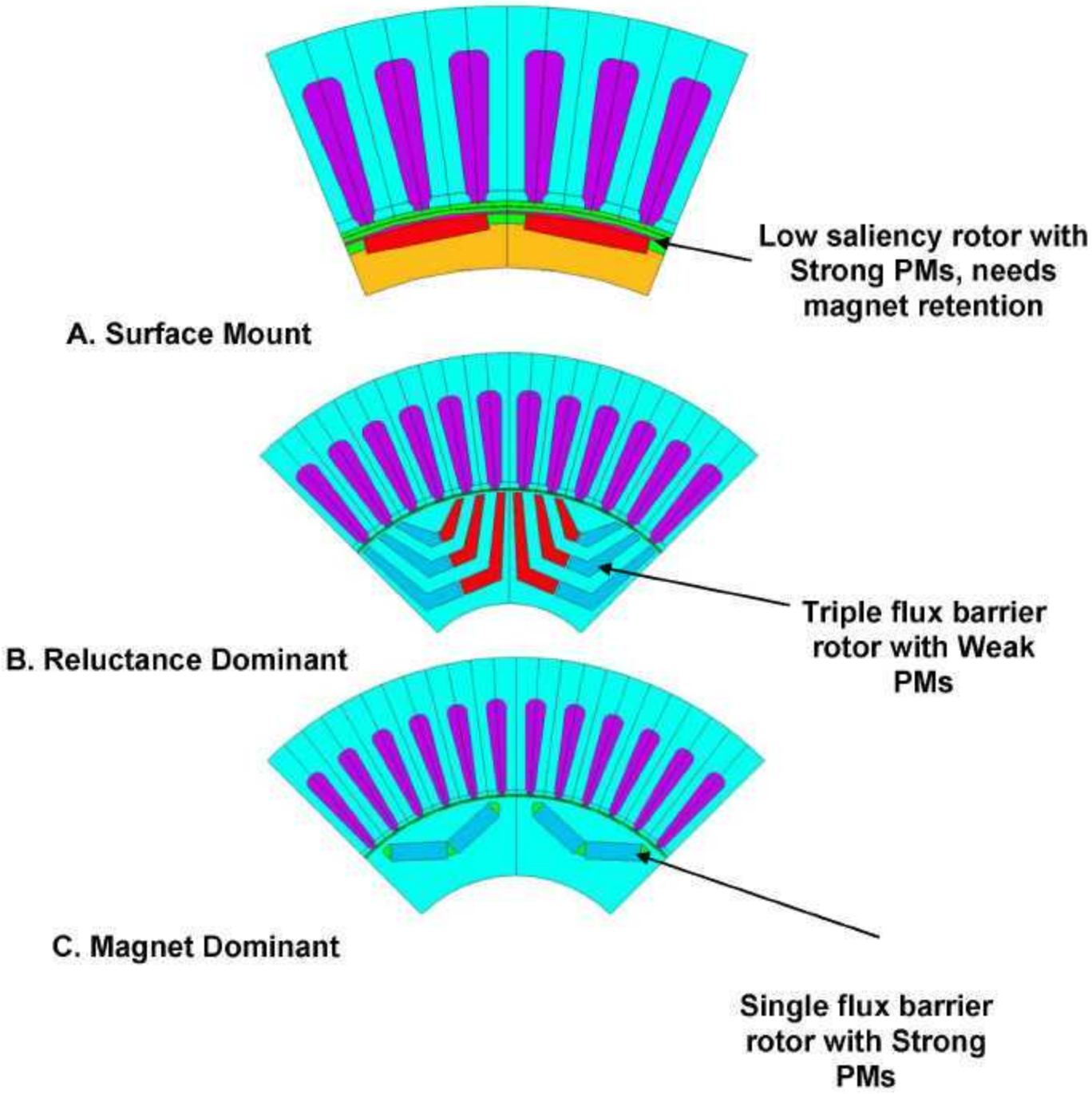


**Fig. 5. Physical topology, three designs.**

## 2.2 APPROACH

Parametric finite-element models that define the geometry of each configuration were created such that the geometry for each design could be quickly manipulated and reevaluated. Finite-element analysis (FEA) was used to evaluate the motor parameters such as the back-EMF constant (Ke) as well as the quadrature axis (q-axis) and the direct axis (d-axis) inductance at a variety of currents. The flux density

in the stator teeth and return path was also evaluated for use in calculating the iron losses. The winding resistance was calculated analytically. The FEA generated flux-density maps from the three designs are displayed below in Fig. 6.

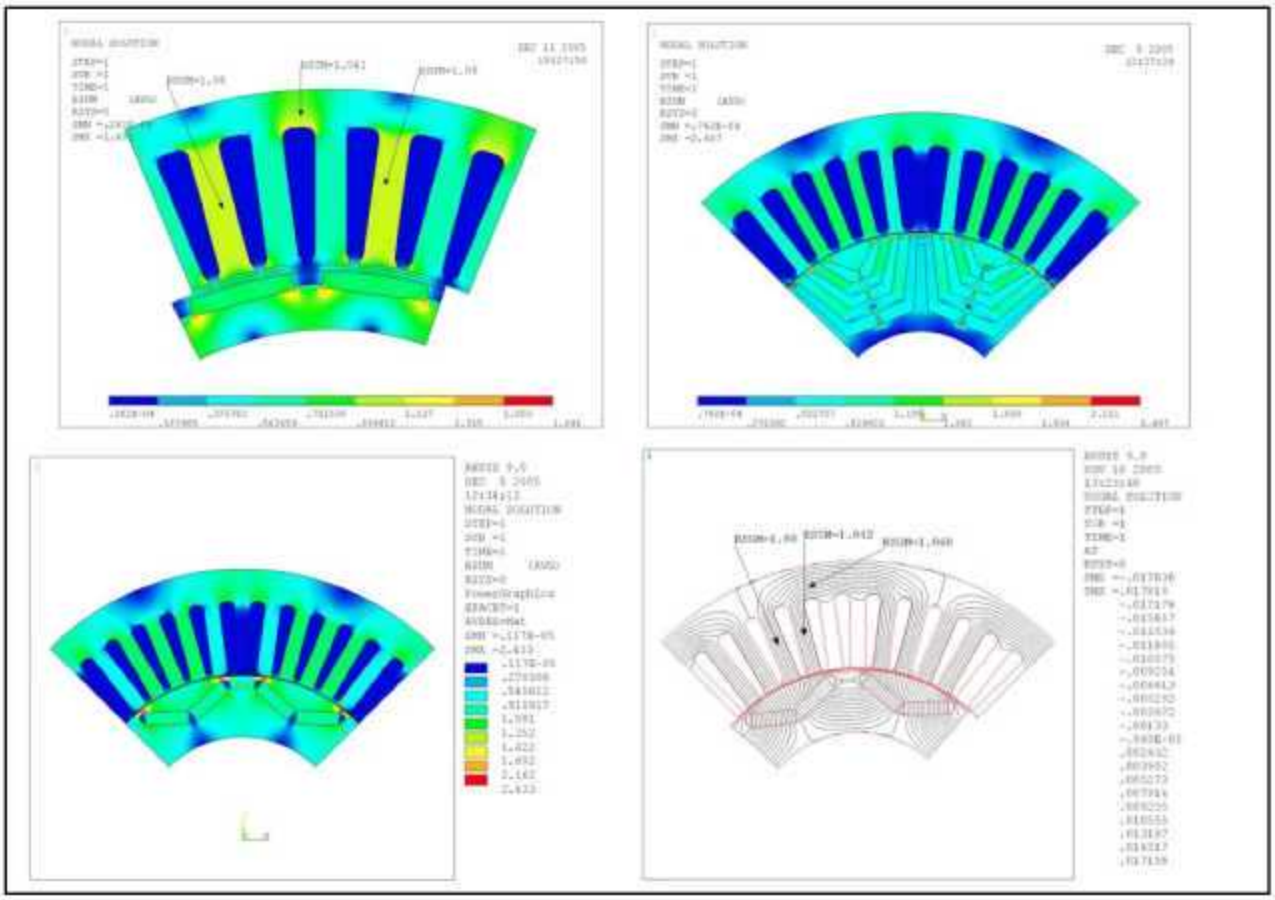

**Fig. 6. FEA results from trade study.**

After the machine parameters were evaluated with FEA, a Mathcad model was used to simulate performance. The Mathcad model is based on the motor design equations and the equations for electric machine vector analysis. This model was used to predict motor performance by inputting the motor parameters that were determined by FEA. This sequence of design iteration was chosen to provide a quick yet accurate method of design evaluation, given the geometry dependence on the motor parameters. The designs were iterated until each could meet as many of the FCVT motor requirements as possible. The three designs were not designed with the intention of operating at full power down to 200 Vdc supply (see Section 1.3).

The design equations for power and torque that account for both magnetic torque and reluctance torque are displayed in Fig. 7 for reference.

$$P_{out} := I_q \cdot E_{pm} + I_q \cdot I_d \cdot \left(L_q - L_d\right) \cdot \omega$$

$$T := pp \left[ \Lambda_{pm} \cdot I_q + \left(L_q - L_d\right) \cdot I_d \cdot I_q \right]$$

**Fig. 7. Motor design equations.**

The block diagram in Fig. 8 describes how the Mathcad model functioned. First, the motor parameters were input into the model. Then the model calculated the efficiency of an operating point along one of the three performance curves of interest Fig. 1, Fig. 2, or Fig. 3. The q-axis and d-axis currents (Iq and Id) were iterated until the maximum efficiency was determined at each point using a peak detection technique. Next, the voltage vectors are summed to determine whether the required voltage exceeds the supply voltage. If the voltage requirement is exceeded, then the d-axis current (Id) is increased until the vector diagram model is satisfied. Now that the necessary Id and Iq have been determined for each point on the operating curve, the efficiency and losses are also calculated for each point and plotted vs. frequency (w). One last iterative process was required to increase accuracy and account for magnetic saturation. After the total current for the operating point was calculated, the inductance values were adjusted to indicate the appropriate level of magnetic saturation.

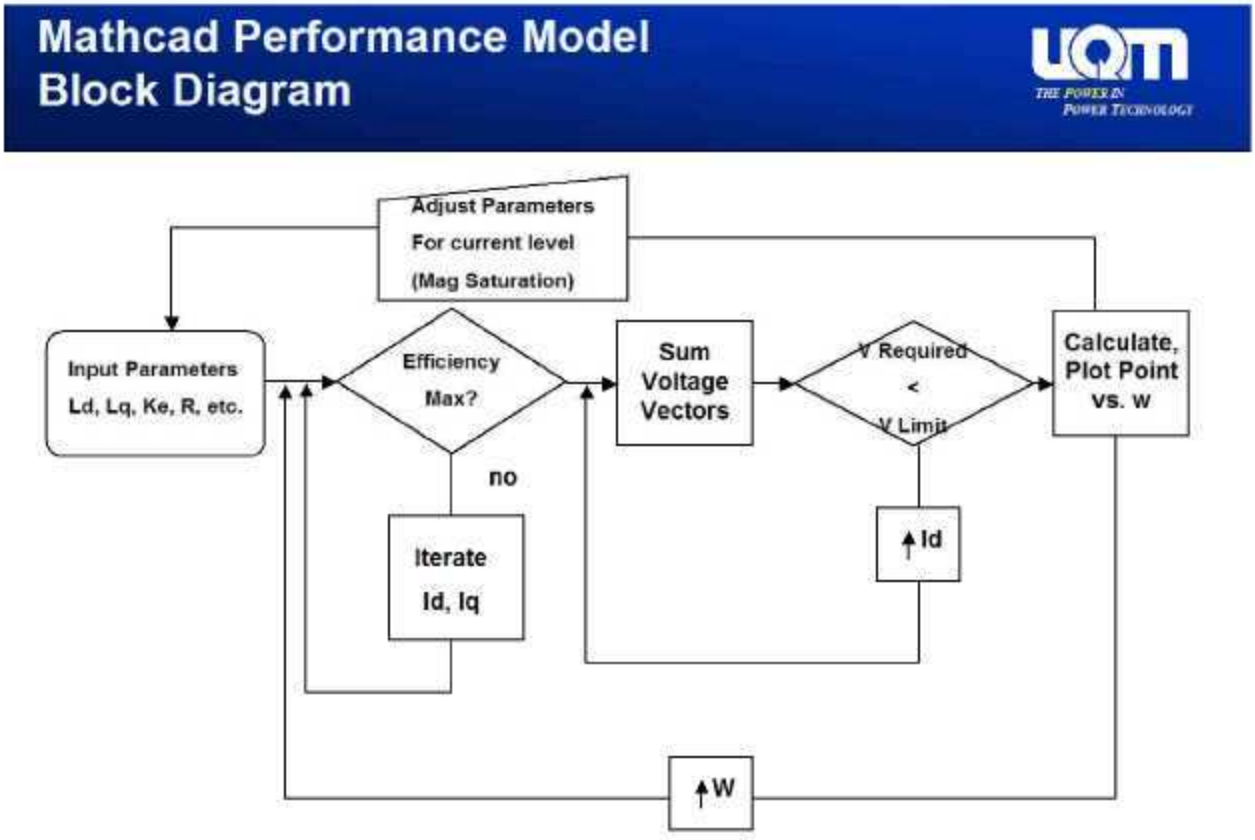


**Fig. 8. Analysis approach for trade study.**

For expediency, electromagnetic analysis was the only type of analysis completed on these designs for this trade study. It is highly possible that structural analysis would indicate that one or more of these designs would not be feasible at high speed.

## 2.3 INDUCTANCE ANALYSIS

Due to magnetic saturation, the inductance values Iq and Id vary greatly with the current load. These values were calculated at many different current levels using FEA to predict how they vary with current, having non-linearity due to magnetic saturation.

Figure 9 charts the results of the FEA analysis for inductance of the reluctance-dominant design at winding currents up to 600 A. Figure 10 indicates the inductance vs. current for the magnet-dominant machine.

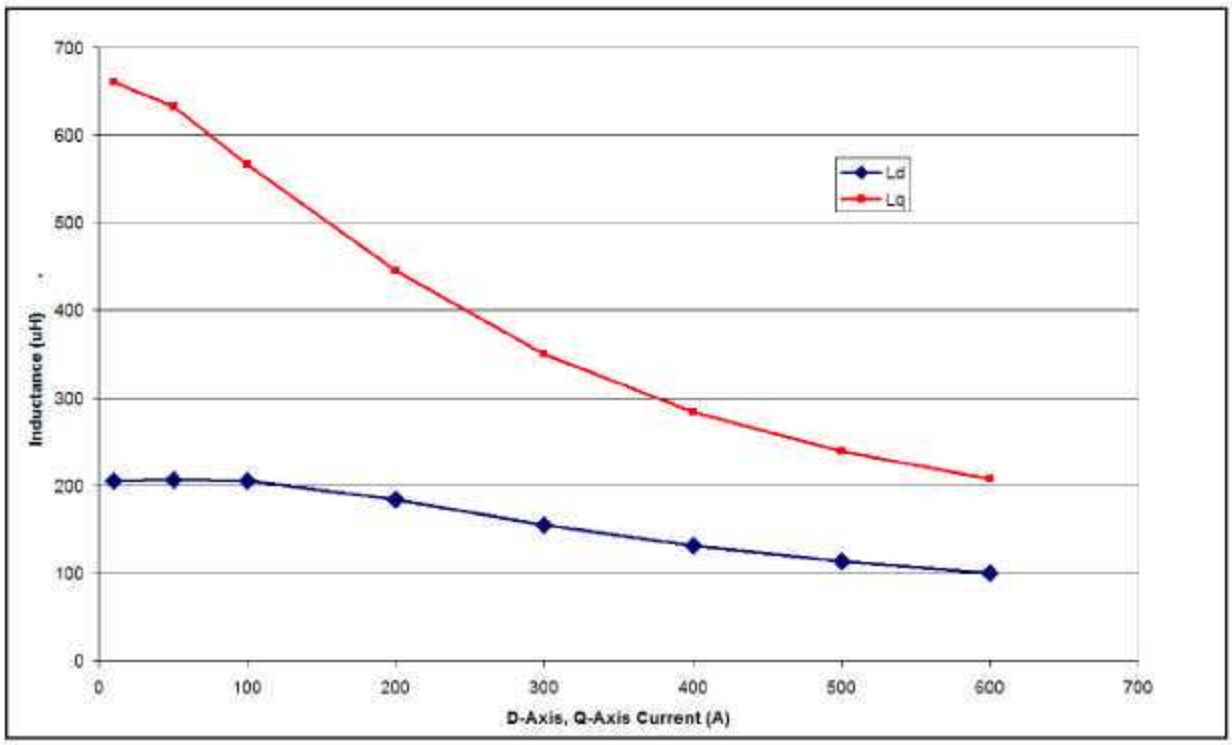


**Fig. 9. Inductance vs. current (reluctance-dominant design).**

Notice the wide difference in q-axis and d-axis inductance at low currents for both designs. At low currents, the saliency ratio for the reluctance-dominant design is higher >3.5:1, as opposed to 2.3:1 for the magnet-dominant design. However, at higher currents where peak power and torque is generated, the saliency ratio for both designs is about 2:1. This is calculated at 500 A for the magnet-dominant design and 600 A for the reluctance-dominant design. The magnet-dominant design inductance analysis was only calculated out to 500A because it required less current than the reluctance-dominant design.

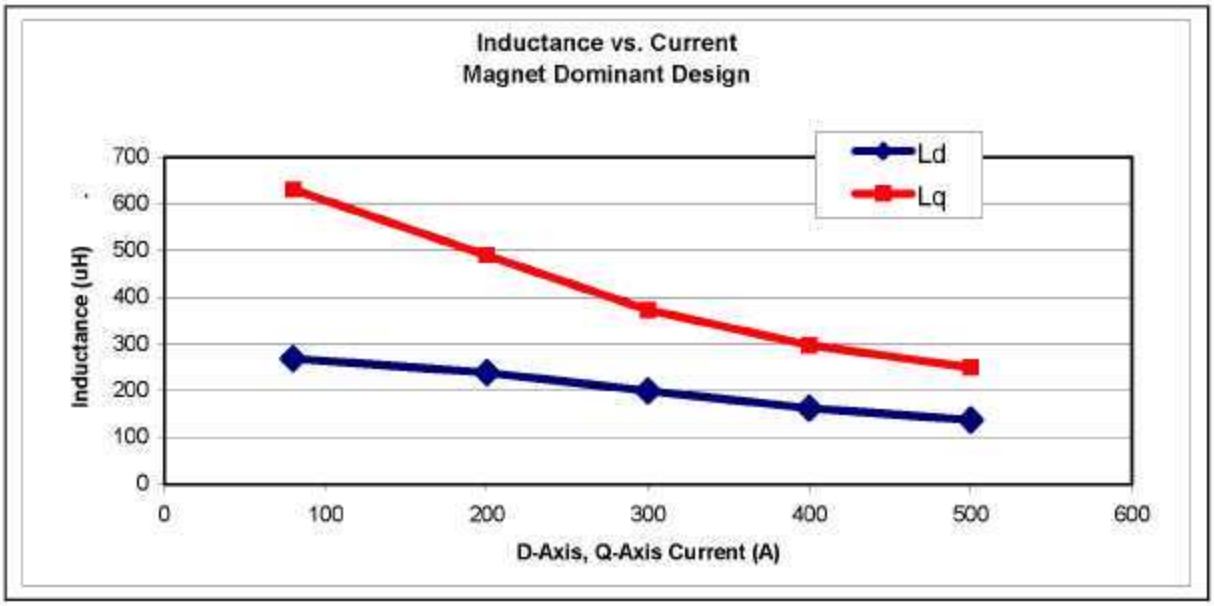


**Fig. 10. Inductance vs. current (magnet-dominant design).**

## 2.4 PREDICTED MACHINE PERFORMANCES

The results of the performance analysis for the three designs in this trade study are displayed throughout this section. Figures 11–13 plot the magnetic torque and the total torque for the three designs as they operate within the required peak power curve specified in Fig. 1. These plots are displayed to illustrate the amount of magnetic torque and reluctance torque utilized by each design. The vertical distance between the red line (total torque) and the blue line (magnetic torque) represents the reluctance torque at any given speed. Note that the gap between the red line and the blue line is the greatest for the reluctance-dominant machine, indicating that it utilizes the most reluctance torque. In the constant torque region (0–2000 rpm), the reluctance-dominant machine produces nearly 1:1 reluctance torque vs. magnetic torque (140 Nm magnetic torque and 122 Nm reluctance torque), see Fig. 13. The reluctance torque vs. magnetic torque ratio would be even higher at lighter loads where saturation has not affected the saliency to such an extent.

The magnet-dominant design produces a greater portion of magnetic torque, 204 Nm, supplemented by 58 Nm of reluctance torque (see Fig. 12). The surface-mount design produces very little reluctance torque as indicated by the red and blue lines being very close together. Approximately 4 Nm of reluctance torque is produced by the surface-mount design in the constant torque region between 0 and 2000 rpm (see Fig. 11).

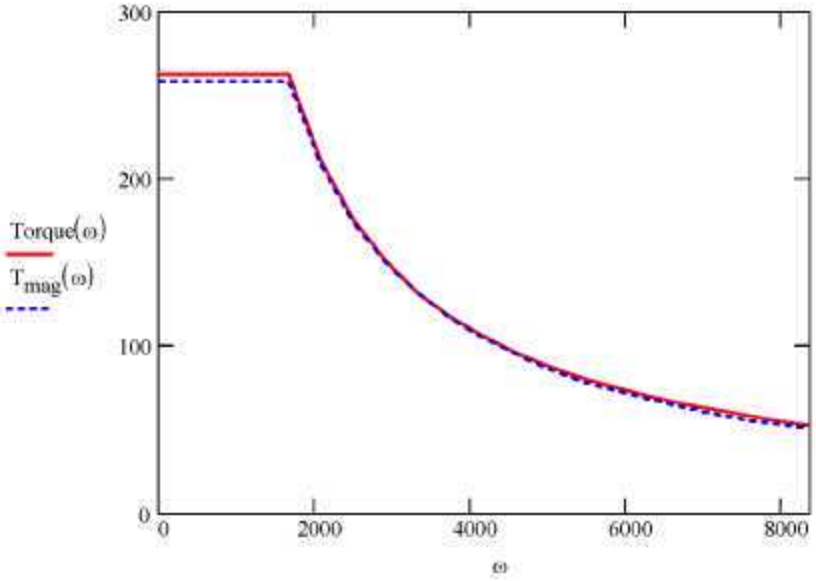


$\text{Torque}(\omega_{base}) = 262.655$ $\quad$ $\text{Torque}(\omega_{max}) = 52.531$

$T_{mag}(\omega_{base}) = 257.949$ $\quad$ $T_{mag}(\omega_{max}) = 50.532$

**Fig. 11. Surface mount, magnetic vs. reluctance torque.**

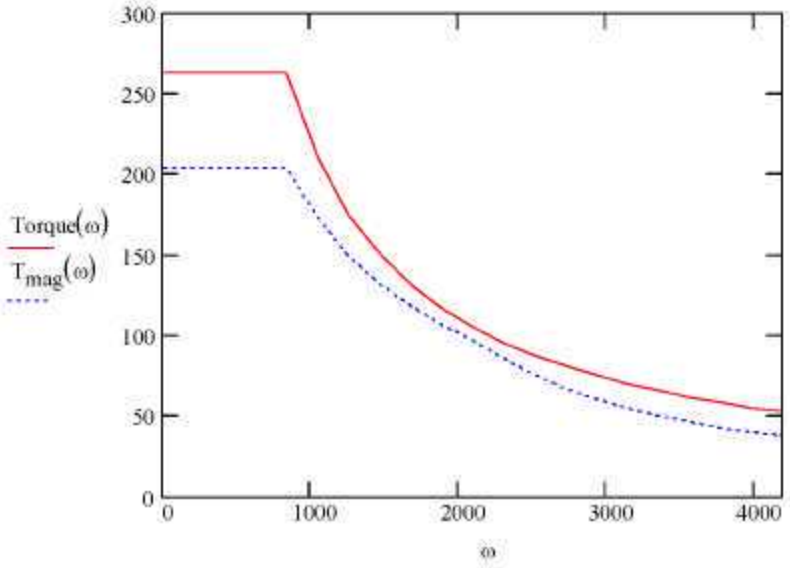


$\text{Torque}(\omega_{base}) = 262.655$ $\quad$ $\text{Torque}(\omega_{max}) = 52.531$

$T_{mag}(\omega_{base}) = 204.027$ $\quad$ $T_{mag}(\omega_{max}) = 37.595$

**Fig. 12. Magnet dominant, magnetic vs. reluctance torque.**

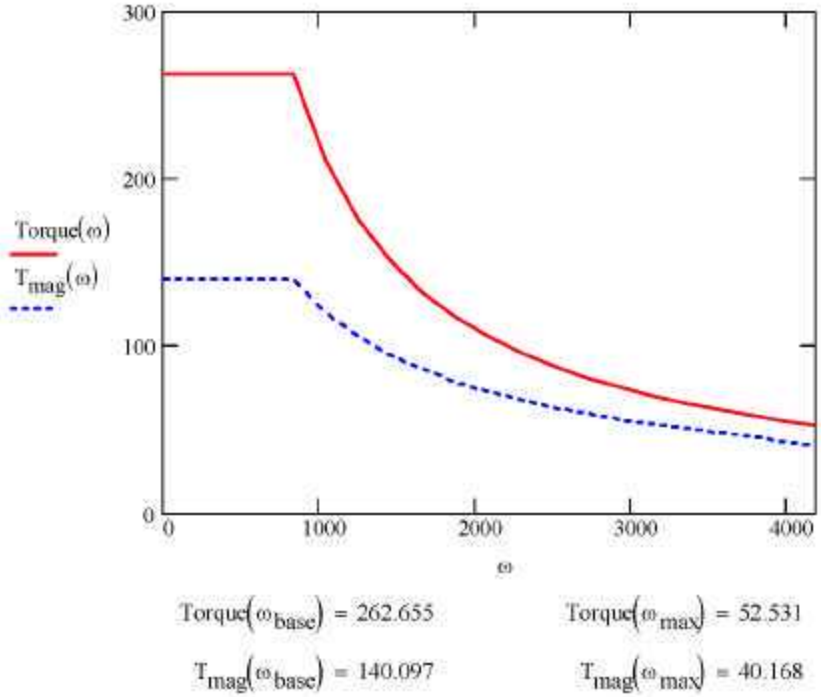


**Fig. 13. Reluctance dominant, magnetic vs. reluctance torque**

Figures 14–16 plots the efficiency and losses for each of the three designs operating on the profile from Fig. 3. As can be inferred from Fig. 14, the surface-mount machine has the highest iron losses of the three designs. At 10 krpm, this machine design is predicted to have 3033 W of iron loss bringing the efficiency at this point down to 92.6%, just shy of the 93% requirement. Its efficiency at 1000 rpm is 95% and the peak efficiency is 95.6%.

The magnet-dominant machine fully satisfied the >93% efficiency requirement with 93.9 % efficiency at 1000 rpm, 95.5 % at 10 krpm, and a peak efficiency of 96.2%; see Fig. 15. The reluctance-dominant machine (Fig. 16) narrowly satisfied the efficiency requirement with 93.0% efficiency at 1000 rpm owing to the high current, relative to the other designs, necessary for this machine to make torque. On the other hand, it did produce the highest efficiency at 10 krpm of the three designs, 97%. The high efficiency at high speeds is due to the weak magnets, inducing less stator flux, and therefore less iron losses. The iron losses for the reluctance-dominant design were 1162 W at 10 krpm.

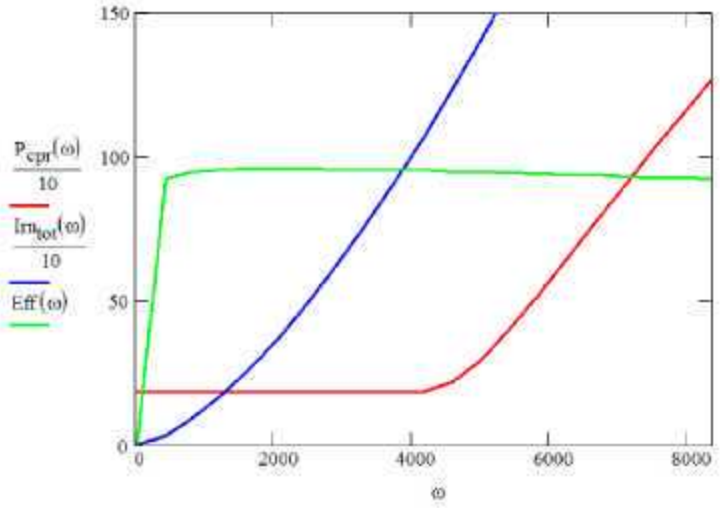


$P_{cpr}(.1\omega_{max}) = 190.077$ $P_{cpr}(\omega_{base}) = 190.077$ $P_{cpr}(\omega_{max}) = 1270.827$

$Irn_{tot}(.1\omega_{max}) = 95.912$ $Irn_{tot}(\omega_{base}) = 271.28$ $Irn_{tot}(\omega_{max}) = 3033.002$

$Eff(.1\omega_{max}) = 95.009$ $Eff(\omega_{base}) = 95.935$ $Eff(\omega_{max}) = 92.674$

**Fig. 14. Surface mount, efficiency and losses.**

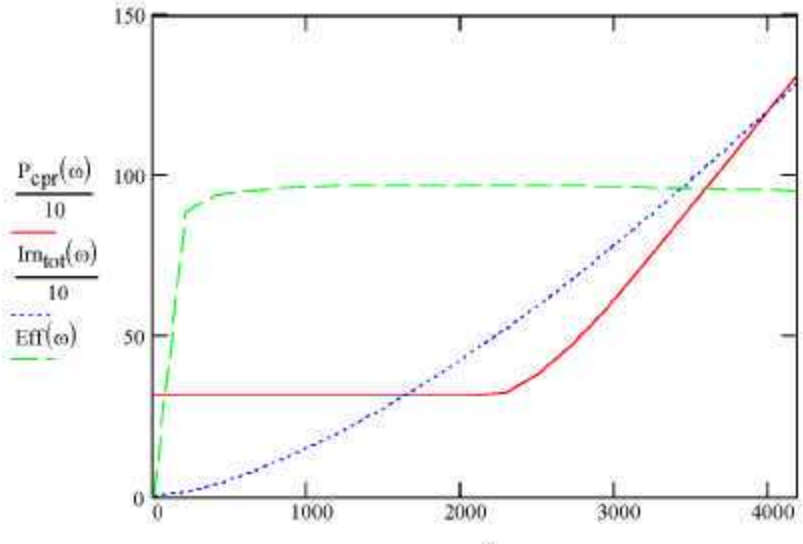


$P_{cpr}(.1\omega_{max}) = 315.317$ $P_{cpr}(\omega_{base}) = 315.317$ $P_{cpr}(\omega_{max}) = 1312.009$

$Irn_{tot}(.1\omega_{max}) = 40.791$ $Irn_{tot}(\omega_{base}) = 115.375$ $Irn_{tot}(\omega_{max}) = 1289.929$

$Eff(.1\omega_{max}) = 93.861$ $Eff(\omega_{base}) = 96.195$ $Eff(\omega_{max}) = 95.439$

**Fig. 15. Magnet dominant, efficiency, and losses.**

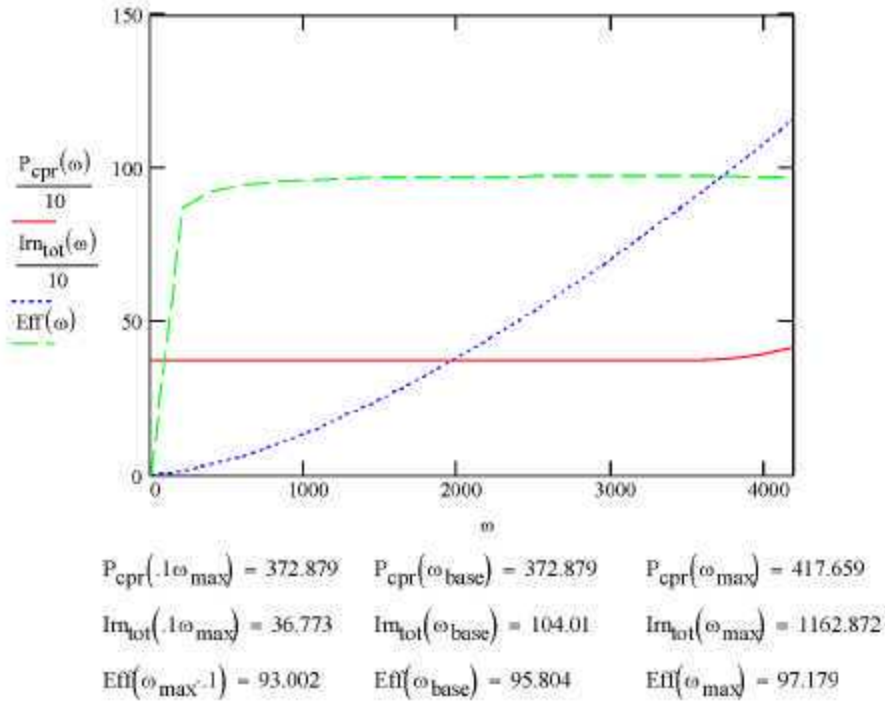


**Fig. 16. Reluctance dominant, efficiency, and losses.**

Figures 17–19 illustrate the predicted voltage and current required, from the Mathcad simulation, to commutate each of the three designs along the operating profile as displayed in Fig. 1. The q-axis, d-axis, and total current are all displayed in terms of root-mean square (RMS) values on each plot. The required voltage at the motor leads is also displayed in terms of the RMS voltage per phase. This and the other simulations for the trade studies were accomplished assuming a 325 V buss voltage. The RMS voltage per phase (effective line-to-neutral voltage at the motor leads) that corresponds to 325 Vdc supply is 126 Vrms per phase. This value also assumes a reasonable voltage drop across the inverter. In each plot, the voltage required (magenta line) continues to increases until it reaches 126 Vrms. At this point, the d-axis current must be raised sharply in order to keep the required voltage below the buss voltage.

Note that for the surface-mount machine in Fig. 17, the q-axis current nearly accounts for the total current until the voltage requirement reaches buss voltage. This is because there is very little saliency and therefore the optimum phase for making torque is aligned with the q-axis, nearly 0 phase angle. Also, note that the surface-mount design does require more current, 428 Arms, to make the maximum torque 262 Nm. The specification states that 400 Arms is the maximum current.

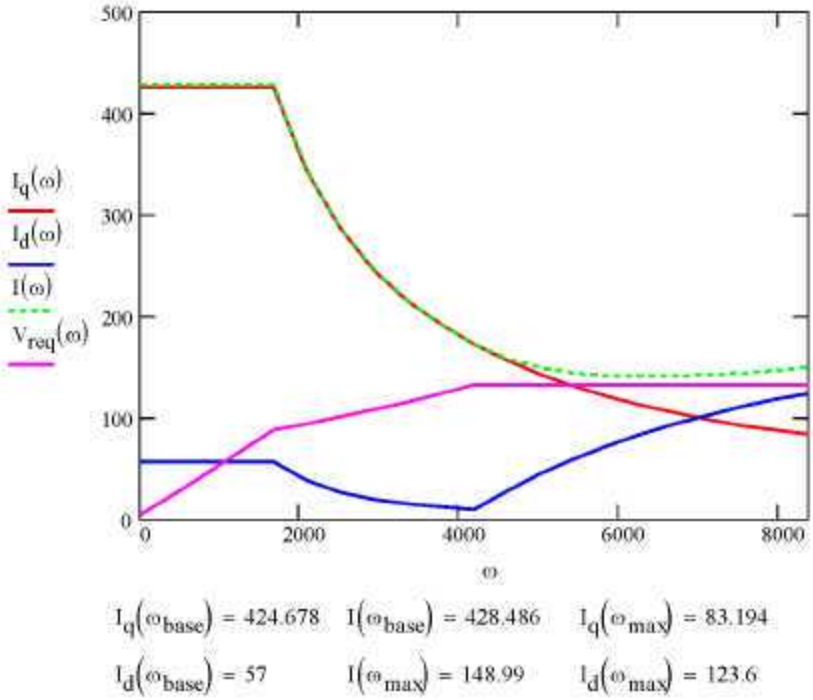


$I_q(\omega_{base}) = 424.678$ $I(\omega_{base}) = 428.486$ $I_q(\omega_{max}) = 83.194$

$I_d(\omega_{base}) = 57$ $I(\omega_{max}) = 148.99$ $I_d(\omega_{max}) = 123.6$

**Fig. 17. Surface mount, voltage, and current requirements.**

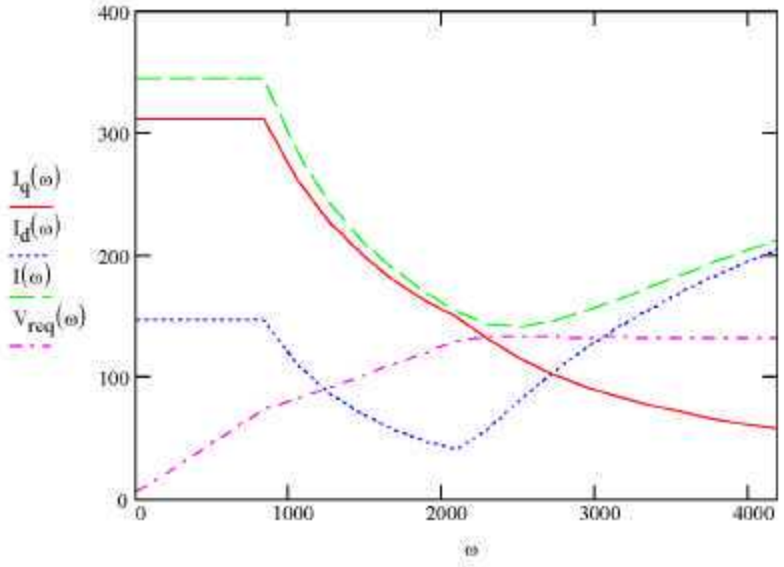


$I_q(\omega_{base}) = 311.459$ $I(\omega_{base}) = 344.578$ $I_q(\omega_{max}) = 57.39$

$I_d(\omega_{base}) = 147.4$ $I(\omega_{max}) = 211.726$ $I_d(\omega_{max}) = 203.8$

**Fig. 18. Magnet dominant, voltage, and current requirements.**

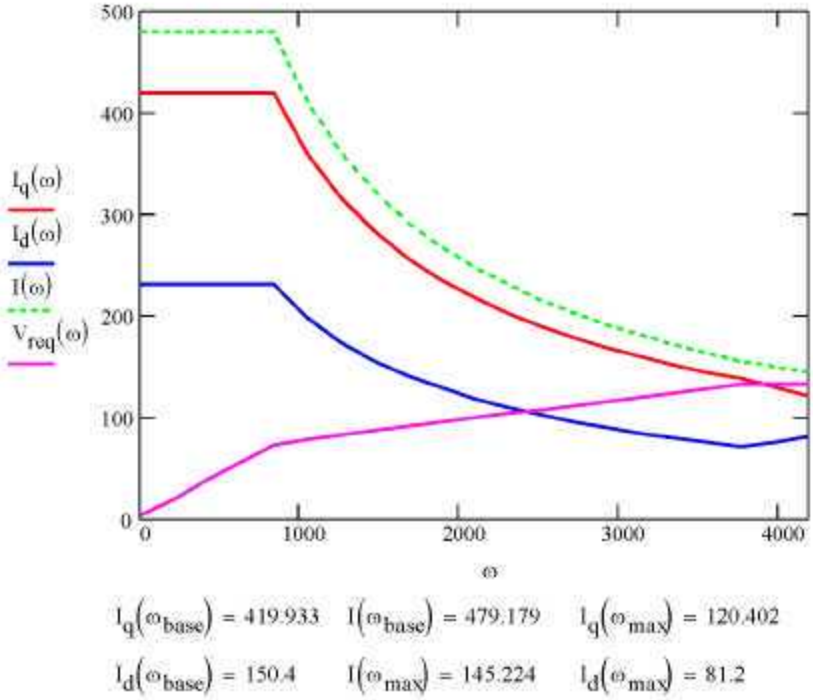


**Fig. 19. Reluctance dominant, voltage, and current requirements.**

In Fig. 18 note that the magnet-dominant design requires more d-axis current than the surface-mount design to produce its optimum torque. The saliency in the rotor incorporates the ability to produce reluctance torque in addition to magnetic torque if the phase of the current is advanced ahead of the q-axis. In the case of this magnet-dominant design, the phase for producing constant torque at the highest efficiency is 25° = ArcTan (147/311), the Arc Tangent of the d-axis current divided by the q-axis current. Also, note that this magnet-dominant design was capable of producing the required torque at under the 400 Arms requirement. The amount of current required for this design to make the maximum torque was 344 Arms.

The reluctance-dominant machine, due to its low voltage constant, did not need additional d-axis current to reduce the required voltage until near the end of the active speed range, see Fig. 19. The small amount of increased current for high speed operation, along with its low iron losses, allowed this machine to achieve high efficiency at high speeds (see Fig. 16). However, this design did require more than the maximum current to achieve peak torque. It required 480 Arms to meet the peak torque specification, higher than the other two designs.

## 2.5 TRADE STUDY SUMMARY AND CONCLUSIONS

The purpose of the trade study was to identify a design direction for the FCVT advanced traction motor and to identify aspects of each design that should be integrated into the advanced traction motor design. The results of the trade study indicated that the magnet-dominant design configuration would best fit the FCVT specifications. Table 5 compares the performance predictions for each design with the FCVT specifications. In Table 5, the values marked in red type indicate the performance predictions that did not meet the specification. The magnet-dominant design met all specifications except the peak power-to-volume specification (power density). However, please note that all of the power densities were

calculated using the most conservative volume calculation as explained in Fig. 4. Also, note that some of these designs would exceed the power density specification if calculated via the least conservative method illustrated in Fig. 4.

**Table 5. Compare three design performances with specification**

| | Freedom Car Specification | Magnet Dominant Design MGDOM11 | Reluctance Dominant Design REDOM | Surface Mount Design SURMO5 |
|---|---|---|---|---|
| **Top Speed** (rpm) | 10,000 | 10,000 | 10,000 | 10,000 |
| 325 Vdc (kW) | 55 | 55 | 55 | 55 |
| **Battery Operating Range** (V) | 200-450 | same | same | same |
| **Nominal Battery Voltage** (V) | 325 | same | same | same |
| **Maximum Current** at motor (Arms) | 400 | 345 | 480 | 428 |
| Characteristic Current (Arms) | <400 | 240.38 | 272.5 | 319.4 |
| **Efficiency** at 10% of maximum Speed and 20% of Rated Torque (1000 rpm, 52.4 Nm) | >93 | 93.9 | 93.0 | 95.0 |
| **Efficiency** at 20% of maximum Speed and 20% of Rated Torque (2000 rpm, 52.4 Nm) | >93 | 96.2 | 95.8 | 95.9 |
| **Efficiency** at 100% of maximum Speed and 20% of Rated Torque (10,000 rpm, 52.4 Nm) | >93 | 95.4 | 97.2 | 92.7 |
| **Back-EMF** at 100% of Maximum Speed (Vpeak, Line to Line) | <600 | 600 | 310 | 670 |
| **Peak Power to Volume Ratio** (kW/Liter) | >12.5 | 10.4 | 8.8 | 10.0 |
| Torque Pulsations % of peak Torque | <5 | ?? | ?? | ?? |
| **Peak Power to weight Ratio** (kW/Kg) | >2.75 | 2.774 | 2.228 | 2.795 |

The reluctance-dominant design failed to meet the specification for maximum current (480 > 400 Arms), power-to-volume (8.8 < 12.5 kW/L) and power-to-weight (2.228 < 2.75 kW/kg) ratios. The power-to-volume and the power-to-weight ratios of the reluctance-dominant design were the lowest of the three designs. Any attempt to improve the maximum current necessary to produce peak torque at the required current would involve making this design larger, further reducing the power-to-volume and power-to-weight ratios. For instance, increasing the thickness of the iron between the flux barriers and/or the thickness of the magnets would increase magnet torque and reluctance torque per unit current; however, it would also add more magnet material and increase the rotor thickness. Although because of weak magnets, the reluctance-dominant design did have the lowest iron losses and therefore the best efficiency

at 10 krpm. Unfortunately, its weak magnets are also responsible for the failure to meet the maximum current and power density specifications.

The surface-mount design also failed to meet the specification for maximum current, (428 > 400Arms). In addition, this design failed to meet the efficiency requirement at 10 krpm (92.7 < 93%) as well as back-EMF (670 > 600 V) and power to volume ratio (10 < 12.5 kW/L). However, the surface-mount design did have the best power to weight ratio of the three designs owing to its thin magnet back iron requirement. In addition, the high pole count allows reduced stator tooth and return path thickness providing more weight savings. As a result, although the final design for the advanced traction motor will adopt the magnet-dominant concept, it will utilize a higher pole count as used in this trade study for the surface-mount design to further improve the power density. In addition, the surface-mount design also had the shortest end-turns (0.7 in.) as opposed to 1.18 in. for the magnet-dominant design and 1.29 in. for the reluctance-dominant design. The shorter end-turns are also attributed to the higher pole count and lead to less volume, weight and axial space claim. Table 6 compares the motor parameters and major dimensions for each of the three designs.

**Table 6. Compare three design motor parameters**

| | Magnet Dominant Design | Reluctance Dominant Design | Surface Mount Design |
|---|---|---|---|
| Pole Pairs | 4 | 4 | 8 |
| Slots per Pole | 6 | 6 | 3 |
| Back-EMF Constant @ 100 C | 60 | 31 | 68 |
| Resistance (Ohms L-L) at 100 C | 0.0251 | 0.0106 | 0.019 |
| Phase Inductance Lq (uH)* | 465.5 | 245.6 | 96 |
| Phase Inductance Ld (uH)* | 227 | 101.2 | 89 |
| Saliency Ratio | 2.05 | 2.43 | 1.079 |
| Overall Diameter | 8.865 | 9.35 | 9.05 |
| Stack Length | 2.85 | 2.95 | 3.83 |
| Endturn Length | 1.18 | 1.29 | 0.7 |
| Overall Length | 5.21 | 5.53 | 5.23 |
| Volume | 5.27 | 6.22 | 5.51 |
| Stator Weight | 22.3 | 22.4 | 24.9 |
| Rotor Weight | 8.7 | 9.7 | 6.0 |
| Magnet Weight | 1.9 | 5.0 | 2.2 |
| Winding Weight | 10.9 | 17.3 | 10.3 |
| Total Weight (kg) | 43.7 | 54.4 | 43.4 |
| Total Weight (lbs) | 19.8 | 24.7 | 19.7 |
| NdFeB Magnet Type | Sintered | Bonded | Sintered |
| Magnet Strength Used for Modeling (Residual Induction in Teslas) | 1.15 | 0.6 | 1.15 |
| Max Operating Temp (Celcius) | 180 | 180 | 180 |
| Magnet Retention Required | No | No | Yes |

# 3. MAGNET COST STUDY

The purpose of the magnet cost study was to get an accurate picture of current magnet prices for NdFeB magnet materials from a variety of magnet sources, domestic and offshore. Since magnets are a relatively significant part of the total cost of a PM machine, it is beneficial to have good cost data for estimating manufacturing costs. UQM decided that the most accurate way to get cost data in volume is to have actual magnet suppliers quote a simple arbitrary shape in various volume quantities. After receiving the quotes, UQM calculated the magnet cost per pound from the official quotations. UQM requested quotes from magnet sources from the United States, Europe, Japan, and China. Also quoted were Chinese magnets distributed through a U.S. company and a U.S. company that processes finished magnets from Japanese magnet materials.

## 3.1 APPROACH

Each magnet manufacturer or distributor was given the same package of material and part specifications to quote pricing. The package included the drawing and magnetic material specifications in Fig. 20. Each manufacturer or distributor was asked to quote each magnet specification in quantities of 10k/year to 110M per year. The magnet shape, shown below, was to be quoted with four different sets of material properties. The magnet properties were chosen to a represent high energy and a high coercivity magnet in both a sintered and a bonded NdFeB magnet type. The actual magnet properties that were quoted are listed below in Fig. 20. The high-energy magnets give the highest residual induction (magnet strength) and can induce more flux in the air gap and stator. The high coercivity magnets are able to operate at higher temperatures without permanent demagnetization. Although the FCVT motor will probably utilize a magnet that has properties closer to the high coercivity magnets, we wanted to see how the price varied on the other end of the energy-coercivity spectrum. These properties have a direct tradeoff in magnet chemistry. Also, please note that no coating material was specified.

Figure 20 contains numerical values in red type which indicate the state-of-the-art for that particular type of magnet. The magnet properties that are in black type are the properties that were actually quoted by the magnet manufacturers. We did not have them quote state-of-the-art properties, because only a few companies can produce such magnets and most have not reached full-scale production on magnets with such properties. Bonded magnets, as can be inferred from Fig. 20, have inherently lower magnet strength (Br) and coercivity. Although the decrease in coercivity does not translate directly to lower operating temperatures, the lower magnet strength does translate directly to lower flux induced in the stator per unit of material.

The arbitrary prismatic shape of the test magnet was chosen in an attempt to remove the shape aspect as a variable in the cost study. The magnet suppliers were expected to create a quote based on the most cost effective manufacturing process required to produce this finished product.

| Magnet Type | Br, min (T) | BHmax (MGOe) | Hcj, min, (kOe) | Temp Range °C |
|---|---|---|---|---|
| Sintered Neo | 1.4 | 50 (60) | 10 | 60–100 |
| Sintered Neo | 1.1 | 30 | 25 (36) | 150–180 (180–240) |
| Bonded Neo | .7 | 11 | 7 | >130 |
| Bonded Neo | .4 (.6) | 6 | 12 (16) | >150 |

-Note Values in red type and parenthesis represent the State-of-the-art, not what was quoted
-No coating material specified

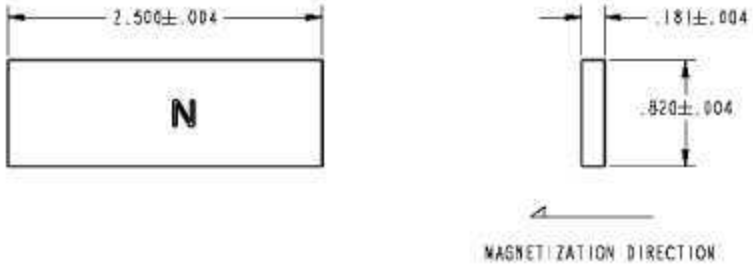


| | Density (lb/in^3) | Weight (lb) |
|---|---|---|
| Bonded | 0.2170 | 0.0805 |
| Sintered | 0.2700 | 0.1002 |

**Fig. 20. Specifications for magnet quoting.**

## 3.2 MAGNET COST STUDY RESULTS

UQM took the results of the $/unit quotes from the magnet vendors and translated those into $/lb for each material and plotted the results in Figs. 21–25. Please note that the results reflect the cost per pound of each magnet finished to shape, without a coating.

The chart in Fig. 21 compares the cost per pound data from the magnet vendors' quotes for the "Sintered High Coercivity Magnets" vs. units per year of production. This is units per year of magnets, as quoted in the shape specified in Fig. 20. As can be seen from the chart, the Chinese magnet manufacturer quoted the lowest at each volume. The price per unit volume did not change substantially from 10k to 10M units per year, from $19/lb to $17/lb for the Chinese manufacturer (red bars). The U.S. magnet manufacturer with U.S. material processing started at about $25/lb at 10k/yr and dropped to about $20/lb at 10M/yr. A U.S. company that utilizes Japanese materials quoted $27/lb at 10k and $23/lb at 10M. A premium was obviously charged to purchase Chinese magnets through U.S. distribution (yellow bars). In quantities higher than 100k/year, the Japanese were the most expensive followed by Europe.

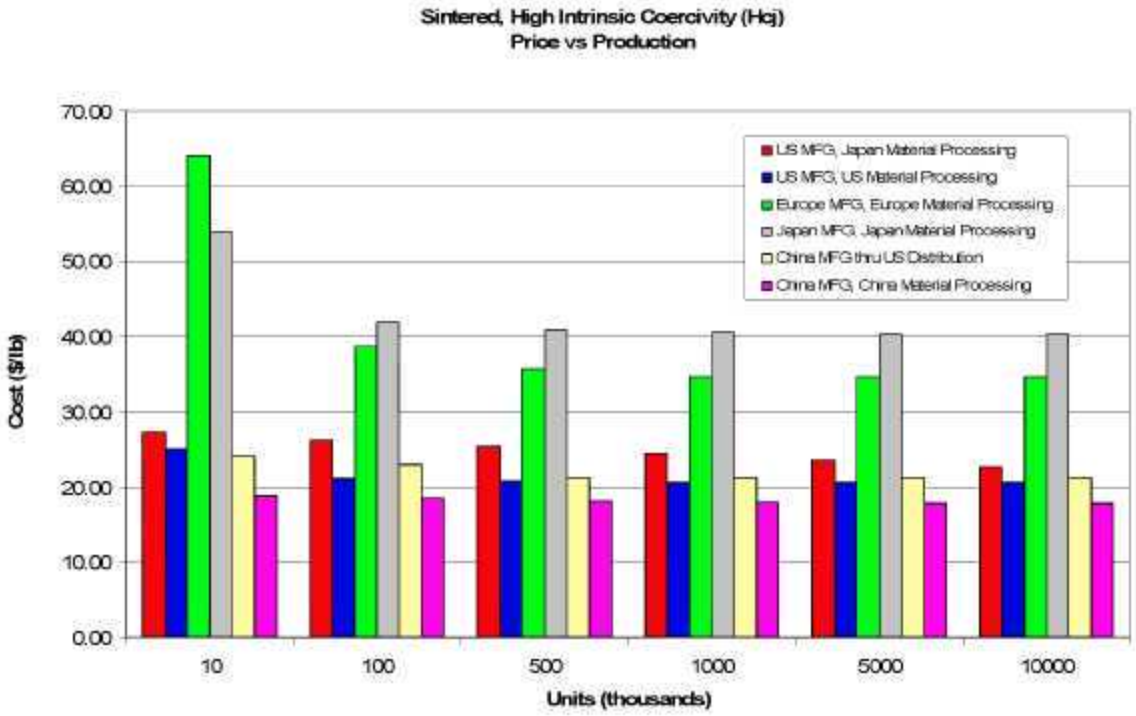


**Fig. 21. Sintered, high intrinsic coercivity price vs. production.**

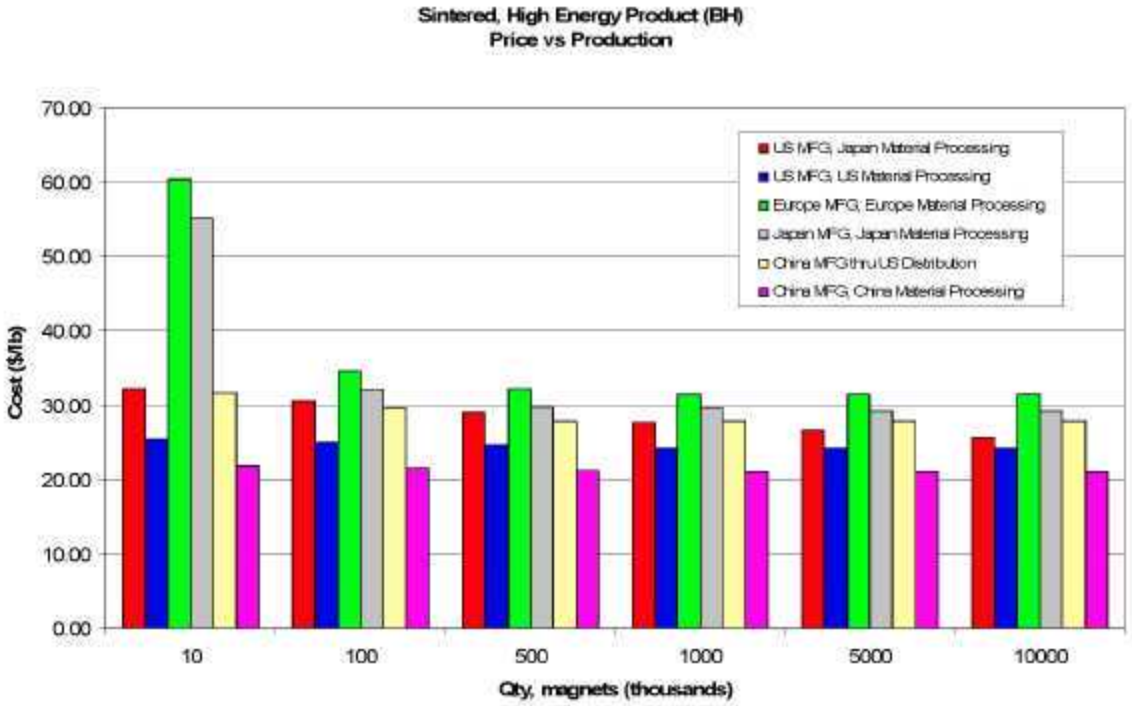


**Fig. 22. Sintered, high energy product, prices vs. production.**

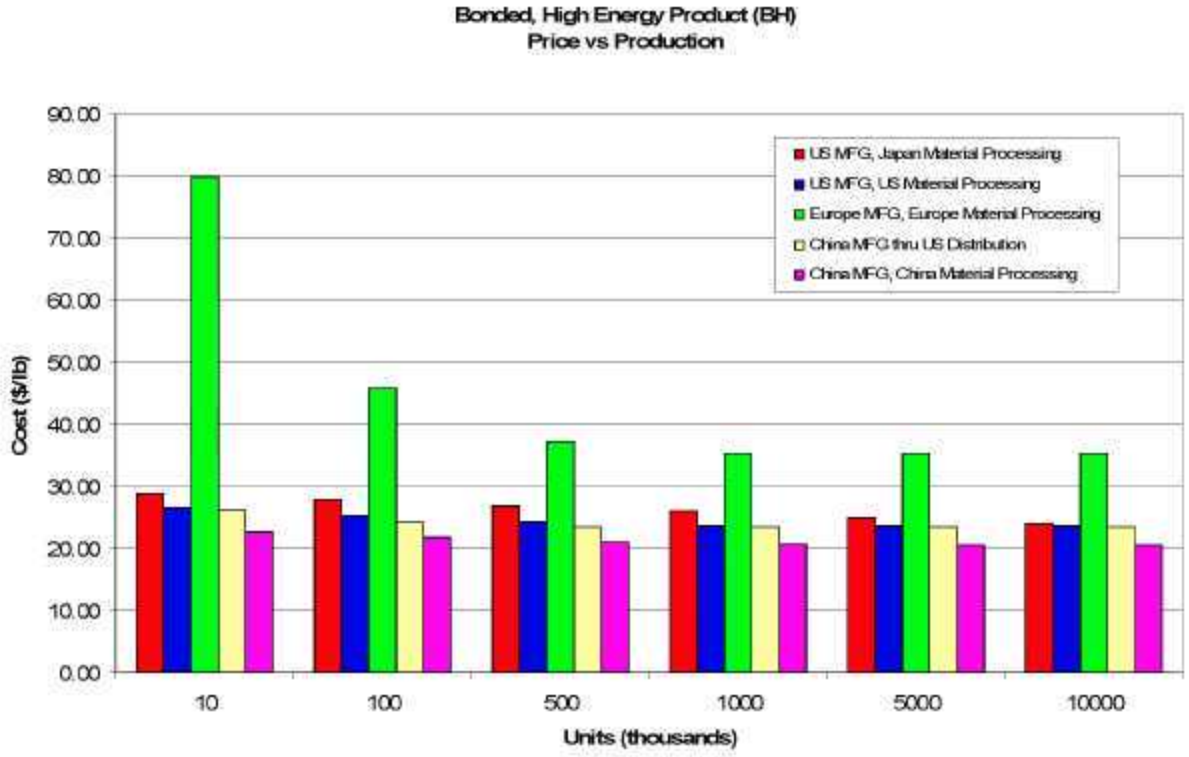


**Fig. 23. Bonded, high energy product price vs. production.**

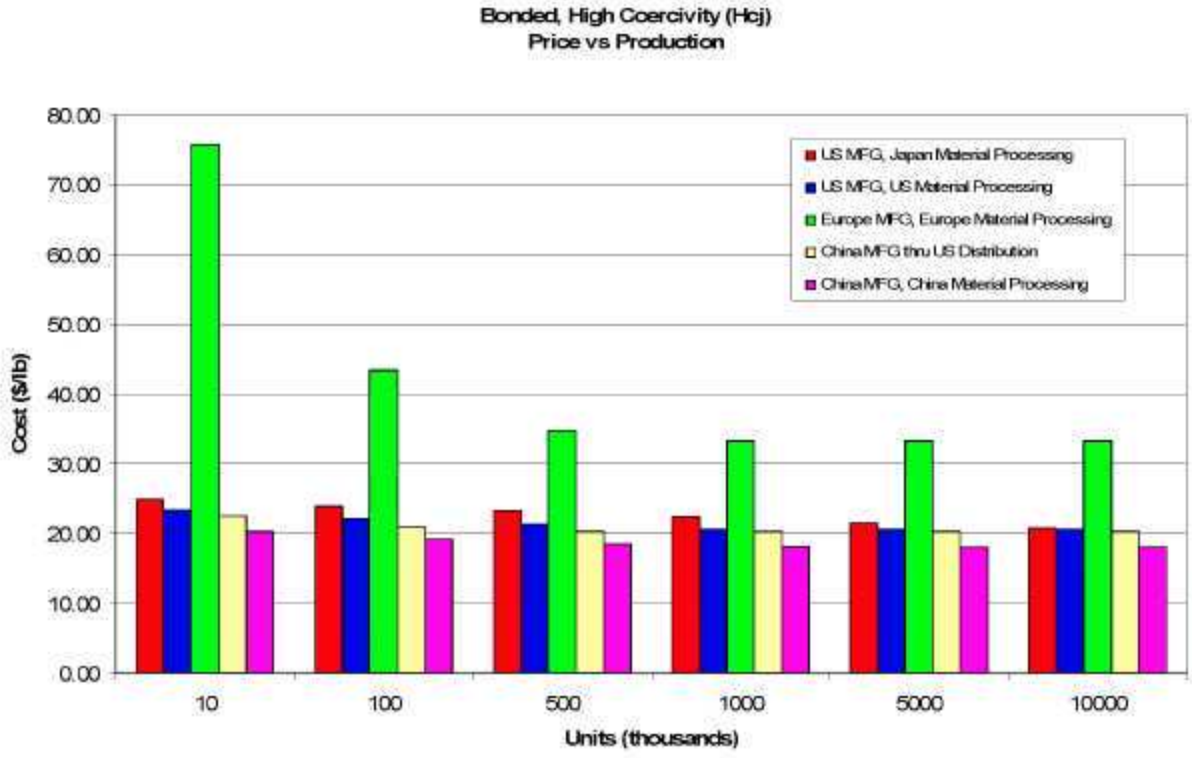


**Fig. 24. Bonded, high coercivity price vs. production.**

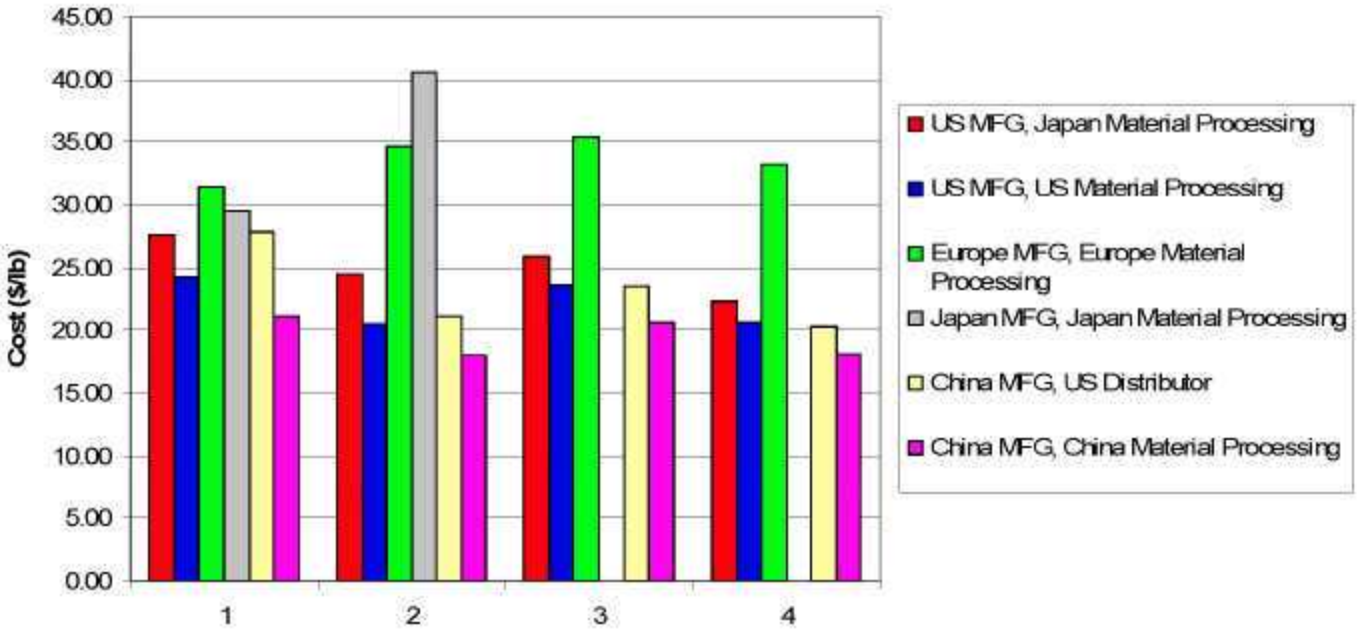


**Fig. 25. Magnet type cost comparison at 1M units/year.**

In the "sintered high energy product" magnet group (Fig. 22), the difference in price between the magnet manufacturers was not as great. At the 1M units per year quantity, the highest cost was Europe at $32/lb, and the lowest was China at $21/lb. In this case, the magnets from Europe were the highest, costing more than the magnets from Japan. China also had the lowest priced magnets in the high-energy sintered variety.

The bonded high energy product magnets from China (Fig. 23) had a similar cost per pound to the sintered high energy product magnets from China, approximately $21–23/lb for each. The bonded and sintered high energy product magnets from the U.S. also had similar cost among the various production volumes at $23–27/lb. The bonded high energy magnets from Europe were the highest priced. The Japanese company used in this study did not quote on the bonded magnets.

The bonded high coercivity magnets followed the same trend as the sintered high coercivity magnets in being less expensive than their high energy counterparts. The cost of the Chinese magnets ranged from $17–20 per pound and the U.S. magnets ranged from $20–23 per pound. Again, the prices from Europe were measurably higher than the other sources.

The bar graph in Fig. 25 illustrates the cost of all of the magnet types from each of the various magnet sources at one volume, 1M units per year. It can be seen that the cost of high coercivity magnets in both the bonded and sintered variety were nearly equal in cost per pound from the Chinese vendor at $17/lb. The same trend followed with the high coercivity magnets from the U.S. manufacturer. The bonded magnets were slightly higher, $21/lb, and the sintered magnets were $20/lb. The high energy bonded and sintered magnets are higher priced than their high coercivity counterparts. However, the bonded high energy magnets are slightly less than the sintered high energy magnets in this case, $20/lb as opposed to $21/lb from China and $28/lb as opposed to $27/lb from the U.S. magnet company.

## 3.3 CONCLUSIONS

The conclusion from the magnet cost study, as it applies to the FCVT motor development effort, supports the conclusion from the trade study that the motor development effort should utilize sintered NdFeB magnets. The reason is that the cost per pound of high coercivity sintered magnets is the same or even slightly lower than bonded magnets. As demonstrated in the trade study, a motor with bonded magnets would utilize significantly more weight in magnets as well as more total motor weight for the same performance level. This would significantly increase the magnet cost per motor. Unless substantially more bonded magnet material is used, a given motor design will produce less back-EMF and less magnetic torque than a comparable sintered magnet design.

Using the magnet weight from the trade study, the bonded magnets in the reluctance-dominant machine would cost $85.00 and the sintered magnets in the magnet-dominant machine would cost $32.30, based on $17/lb from China. This is a difference of $52.70 per motor in magnet cost alone. Also, the U.S. sources are approaching competitive pricing with China, having cost per pound within $3 of the Chinese magnets for sintered high energy magnets at the higher volumes. Having a low cost domestic source would help to hedge the logistic problems associated with sourcing components offshore.

Also, although high energy magnets offer more flux density per pound, they are usually not an option due to the high temperatures of most automotive applications. In addition, the high energy magnets (at least as the properties are defined in this study) are more expensive than the high coercivity counterparts in both sintered and bonded varieties. Therefore, the cost premium would probably offset any cost benefit due to the magnet weight reduction possible with a high-energy magnet.

# 4. ROTOR CONFIGURATION STUDY

Although at this point we are confident that the best design path for the final design is a magnet-dominant configuration, we wanted to explore different rotor configurations that could improve upon the V-shape design used in the Prius. Both the trade study and the magnet cost study confirmed that we should pursue a sintered NdFeB magnet machine; therefore, this study will focus mostly on strong PMs and strive to utilize as much reluctance torque as possible. back-EMF harmonics are also considered in the study from a subjective standpoint.

EMF waveforms were calculated for comparison. Part of the purpose of the study was to find a design that can minimize EMF harmonics and still provide very high torque per unit current. The various rotor configurations that were studied and the figures that give the results for each configuration are listed in Table 7.

**Table 7. Rotor configurations listed**

| Description of rotor configuration, geometry, and FEA model | Torque and EMF Results |
|---|---|
| Figure 26–Single V-barrier, two bridges, two magnets per pole | Figure 27 |
| Figure 28–Single U-barrier, three bridges, two magnets, 80% pole coverage | Figure 29 |
| Figure 30–Single U-barrier, three bridges, two magnets, 95% pole coverage | Figure 31 |
| Figure 32–Double U-barrier, three bridges, four magnets per pole | Figure 33 |
| Figure 34–Single U-barrier, four bridges, three magnets per pole | Figure 35 |
| Figure 36–Single U-barrier, four bridges, three magnets, non-uniform magnets | Figure 37 |
| Figure 38–U-Barrier, two bridges, three magnets per pole | Figure 39 |

## 4.1 APPROACH

For each of the rotor profiles that were modeled, the same stator profile and length was used in the evaluation of each rotor configuration. The major dimensions and characteristics of this stator profile are listed in Table 8. Whenever possible, the magnet weight was kept around 2 lbs to make direct comparisons with the other configurations. For some of the configurations, the magnet weight varies from the standard 2 lbs because of geometric restrictions. For this reason, the weights are published with the results from each configuration. The torque profile, or torque vs. phase angle, for each configuration was evaluated at 1200 A-t using FEA to measure the torque at phase angles from 0–90° electrical. In addition, the back-EMF waveform shape was also evaluated for comparison purposes. The magnet strength was kept constant among each rotor configuration. For the residual induction (magnet strength) of the magnets, 1.15T was used. Analysis was performed assuming material properties at 20°C for the rotor configuration study.

The bridge thickness varied with the designs, but the minimum thickness was not less than .040 in. in each of the designs. For some of the configurations, the bridge thickness had to be increased for strength. The stress in the bridges was checked for the top three configurations and found to be less than 160 Mpa for each.

**Table 8. Stator specifications for rotor evaluation.**

| | |
|---|---|
| Stator OD | 8.6" |
| Stator ID | 6" |
| Length | 3.5" |
| Poles pairs | 8 |
| Turns | 4 |
| Current | 300A |
| Air gap length | .03" |
| Magnet Br | 1.15 T |
| | |

For each of the rotor design configurations that were evaluated, the torque profile (torque vs. current-phase angle) was calculated at 1200 At. Zero degrees of current-phase angle is defined as being "in phase" with the back-EMF. This is the current-phase angle where the maximum magnetic torque is produced and there is zero reluctance torque. Therefore, from the torque profile of each design, the maximum magnetic torque is displayed at the origin of these plots. As the current-phase angle is advanced leading the back-EMF, the magnetic torque decreases and the reluctance torque increases for salient designs. For designs that are highly salient and effectively utilize reluctance torque, the total torque will be higher than the magnetic torque and it will be at maximum at some angle greater than zero. Although total torque is calculated in this analysis and reluctance torque is not calculated specifically, evaluation of reluctance torque can be realized based on the ratio of total torque to magnetic torque.

## 4.2 RESULTS OF ROTOR CONFIGURATION STUDY

The geometry used to model the torque characteristics of the "Single V-Barrier" design (based on the Prius design) is illustrated in Fig. 26, along with the flux line plot from FEA output. After several iterations aimed at maximizing the torque and considering the geometry implementation in the Prius design, it was determined that 80% pole coverage results in the best torque production. The magnet weight was 1.93 lb and the rotor iron comprised 8.85 lb. Note that the air pockets in the stator also resemble those of the Prius. This design was basically scaled down from the actual dimensions of the Prius motor to fit the standard stator dimensions that were chosen.

Figure 27 illustrates the torque profile and back-EMF waveform calculated for the "Single V-Barrier" design. This configuration produced 214 Nm of peak torque at 30° of phase advance at 1200 A-t of current in the windings. At 0° of phase advance, 112 Nm of magnetic torque is produced. As expected, the back-EMF waveform shape looks much like the Prius and the peak voltage is 62.5 V/krpm.

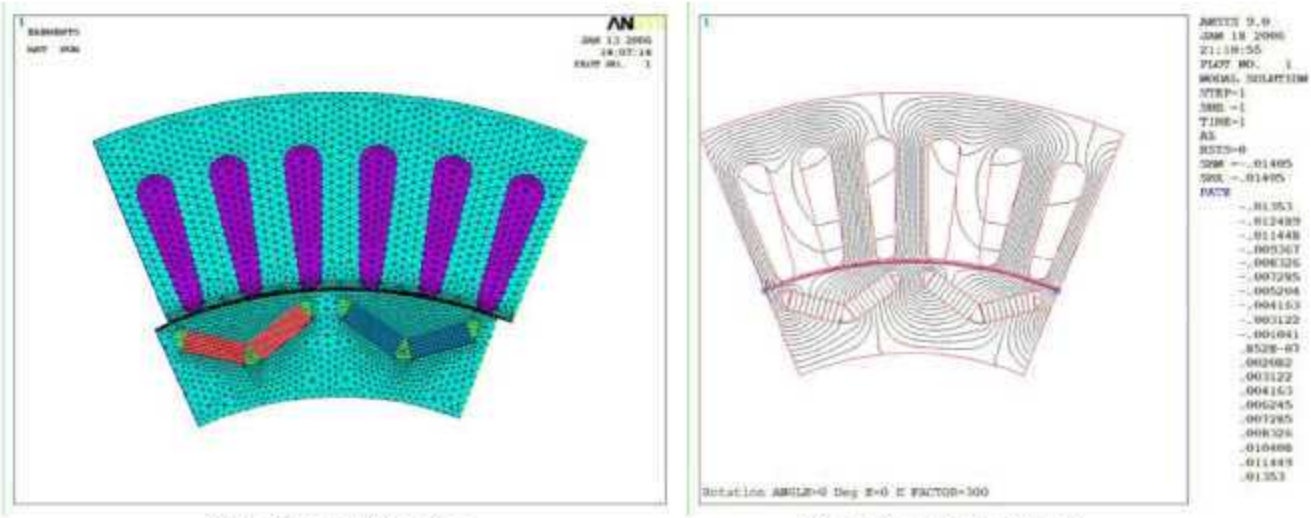

**FEA Element Mapping** **Flux Lines, Under Load**

**Wt_rtr = 8.85 lb wt_mag = 1.93 lb Pole Coverage = 80%**
**Iteration: EXP5**

**Fig. 26. Single V-barrier, two bridges, two magnets per pole.**

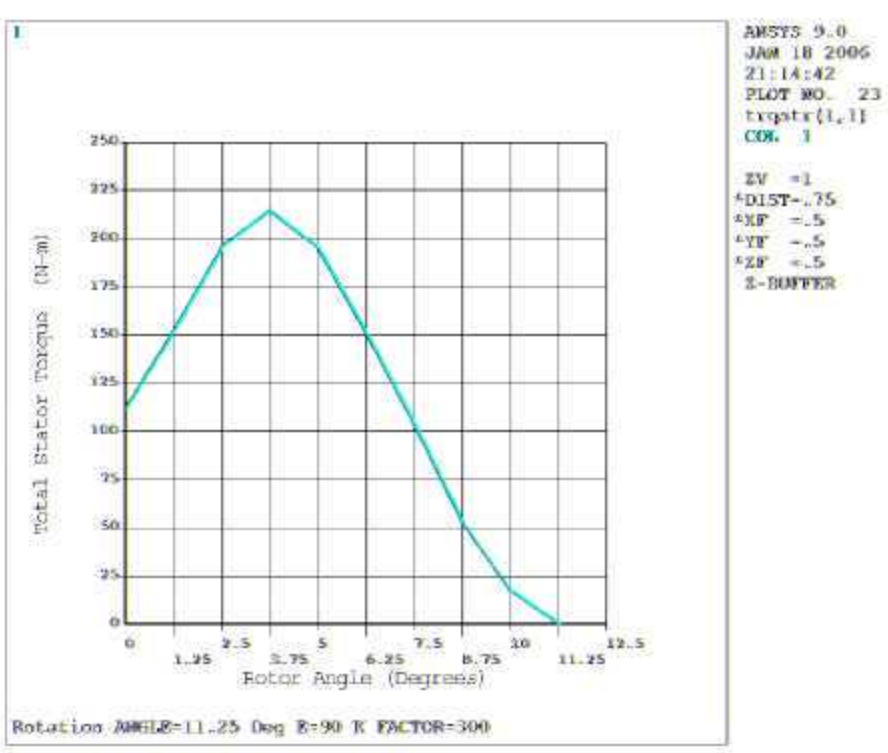


mag torq= 112.01 Rel Torq= 102.26 Total= 214.27

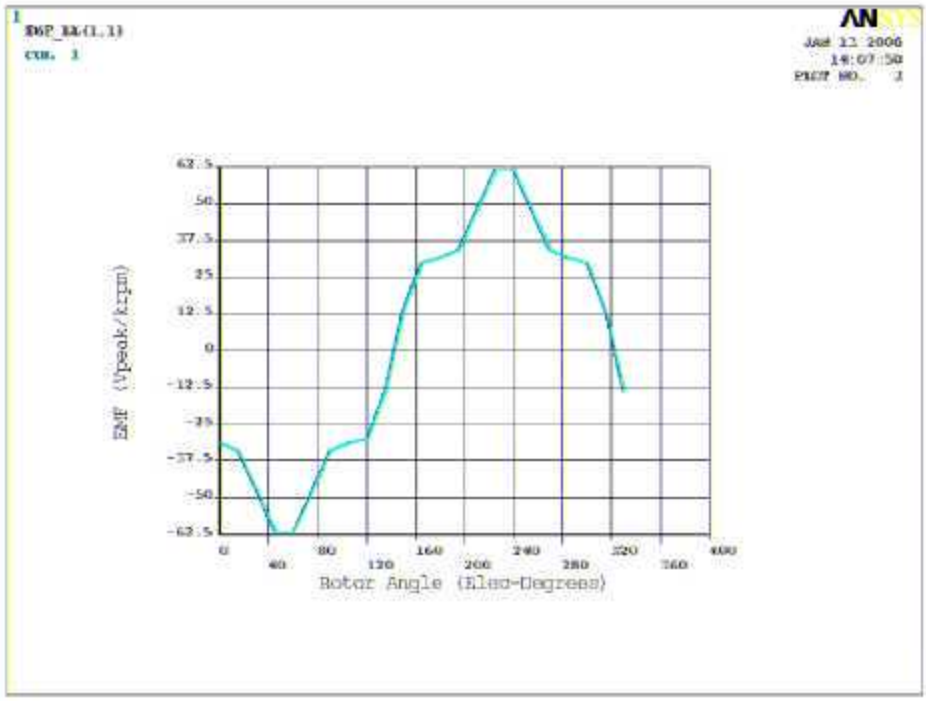


Iteration: EXP5

**Fig. 27. Single V-barrier, two bridges, two magnets per pole – torque profile and back-EMF.**

The geometry used to model the torque characteristics of the "Single U-Barrier with three bridges and 80% pole coverage" design is illustrated in Fig. 28 along with the flux line plot from FEA output. This configuration comprises magnet shapes that probably could not be produced economically as sintered magnets. The three bridge U-shape was simply used initially to experiment with the U-shaped barrier because this parametric geometry already existed. Later iterations to follow utilize the U-Barrier with magnets that can be more easily produced. The magnet weight was 2.02 lb and the rotor iron weighed 9.09 lb. The amount of pole coverage in this design was also set to 80% as in the V-Barrier design above.

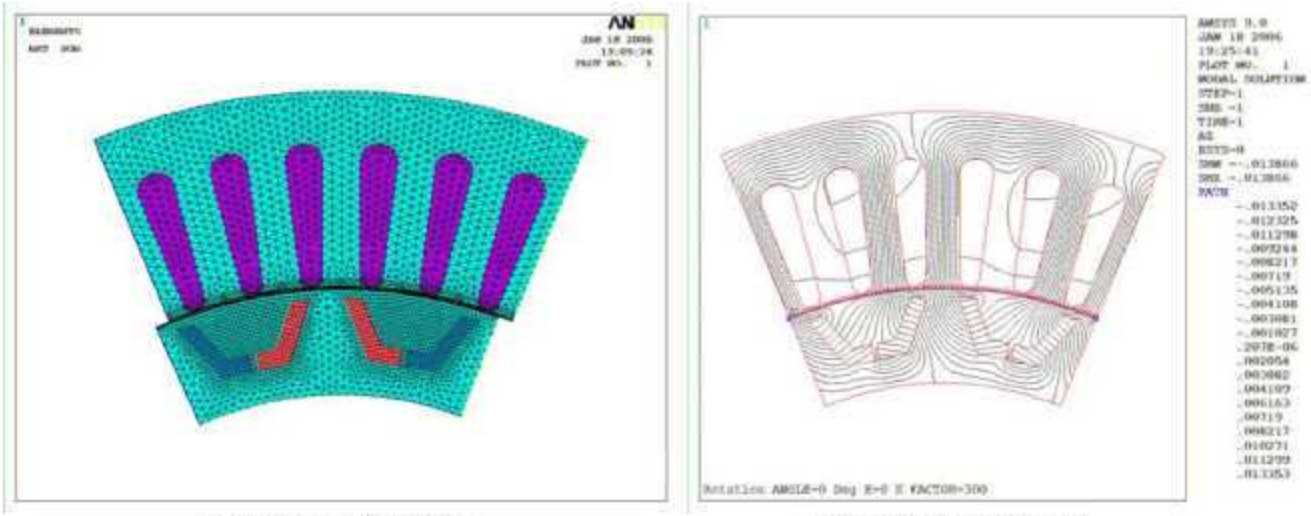

**FEA Element Mapping** **Flux Lines, Under Load**

**Wt_rtr = 9.09 lb wt_mag = 2.02 lb Pole Coverage = 80%**
**Iteration: EXP7**

**Fig. 28. Single U-barrier, three bridges, two magnets, 80% pole coverage.**

Figure 29 illustrates the torque profile and back-EMF waveform calculated for the "Single U-Barrier, three bridge design with 80% pole coverage." This configuration produced 220 Nm of peak torque at 30° of phase advance and 1200 A-t of current in the windings. At 0° of phase advance, 114 Nm of magnet torque is produced. The back-EMF waveform shape was similar to the V-Barrier design, but this configuration had a higher peak voltage at 68 V/krpm.

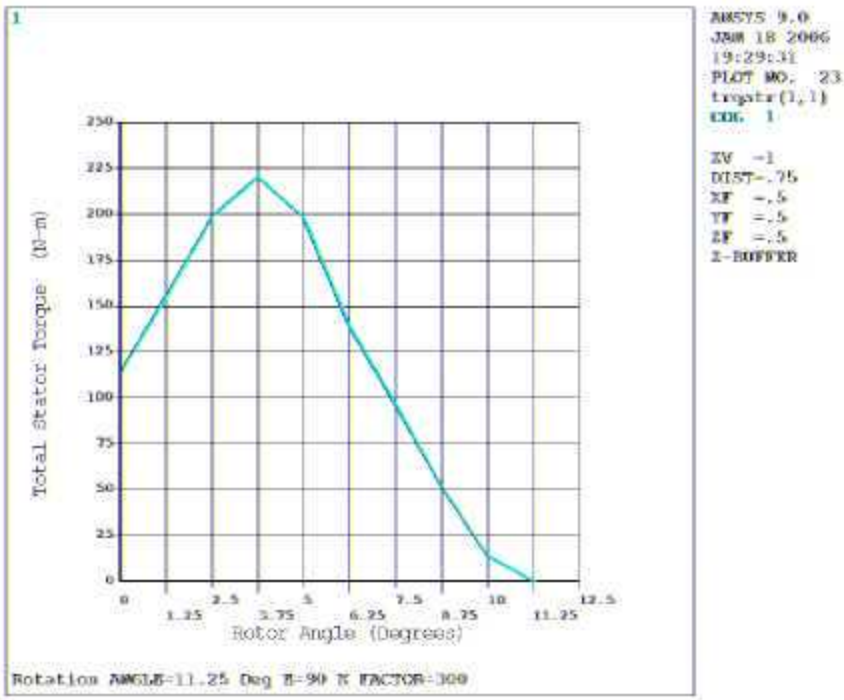


mag torq= 114.07 Rel Torq= 106.18 Total= 220.25

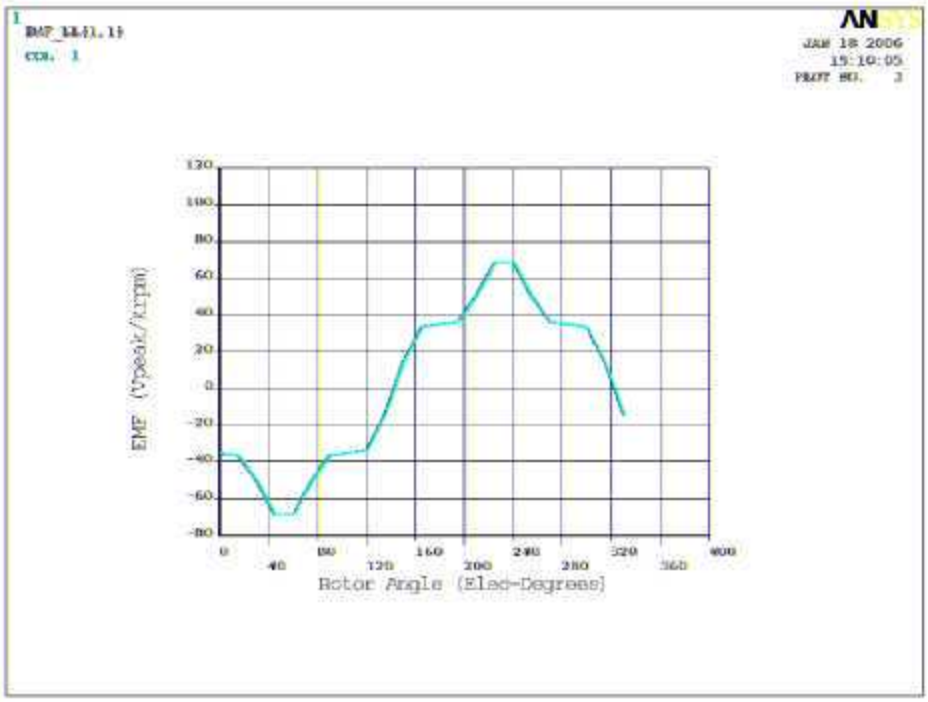


Iteration: EXP7

**Fig. 29. Single U-barrier, three bridges, two magnets, 80% pole coverage –torque profile and back-EMF.**

The geometry used to model the torque characteristics of the "single U-barrier with three bridges and 95% pole coverage" design is illustrated in Fig. 30, along with the flux line plot from FEA output. This configuration was modeled to show the effects of higher pole coverage with the U-shaped flux barrier, 95% in comparison with 80%. The magnet weight was 2.34 lb, higher than the 2 lb standard because the magnet thickness and depth were kept the same as the previous U-barrier design. The magnet weight increased due to stretching the pole coverage from 80–95%. The rotor weight was 8.76 lb.

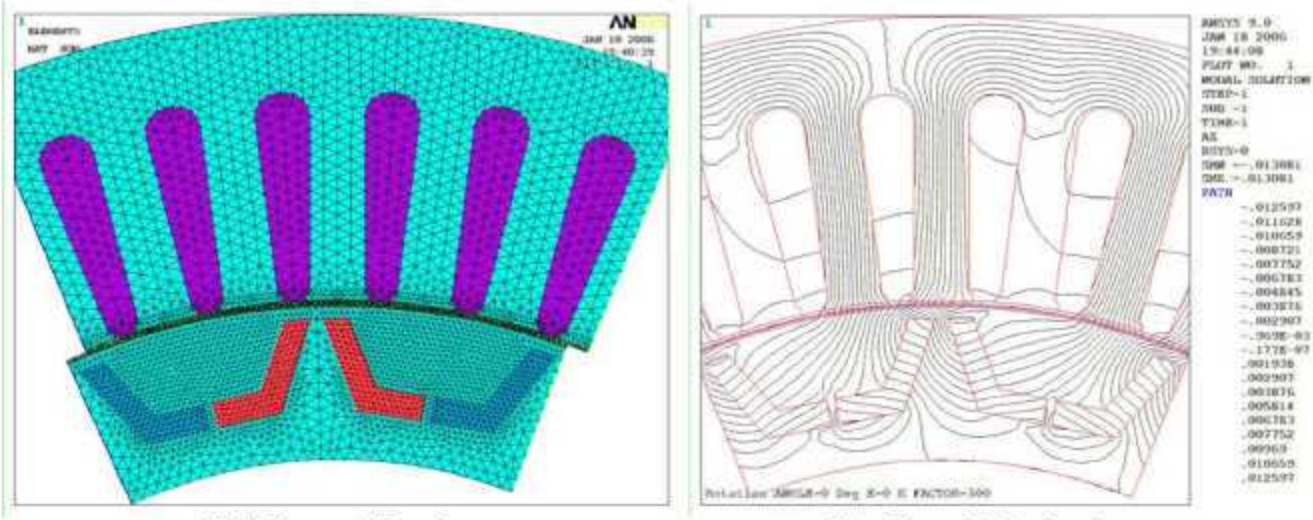

**FEA Element Mapping** **Flux Lines, Under Load**

**Wt_rtr = 8.76 lb wt_mag = 2.34 lb Pole Coverage = 95%**
**Iteration: EXP8**

**Fig. 30. Single U-barrier, three bridges, two magnets, 95% pole coverage.**

Figure 31 illustrates the torque profile and back-EMF waveform calculated for the "single U-barrier, three bridge design with 95% pole coverage." This configuration produced only 179 Nm of peak torque at 30° of phase advance and 1200 A-t of current in the windings. This is down from 220 Nm for the same design with 80% pole coverage. At 0° of phase advance, 134 Nm of magnet torque is produced, up from 114 Nm of magnet torque for the previous design with 80% pole coverage. It is obvious that even though magnet torque is up, reluctance torque has been reduced drastically because the increased pole coverage has reduced the thickness of the permeable path in the rotor allowing more magnetic saturation in the rotor. However, the back-EMF waveform shape is much closer to sinusoidal (containing less harmonic content) than the other designs with 80% or less pole coverage.

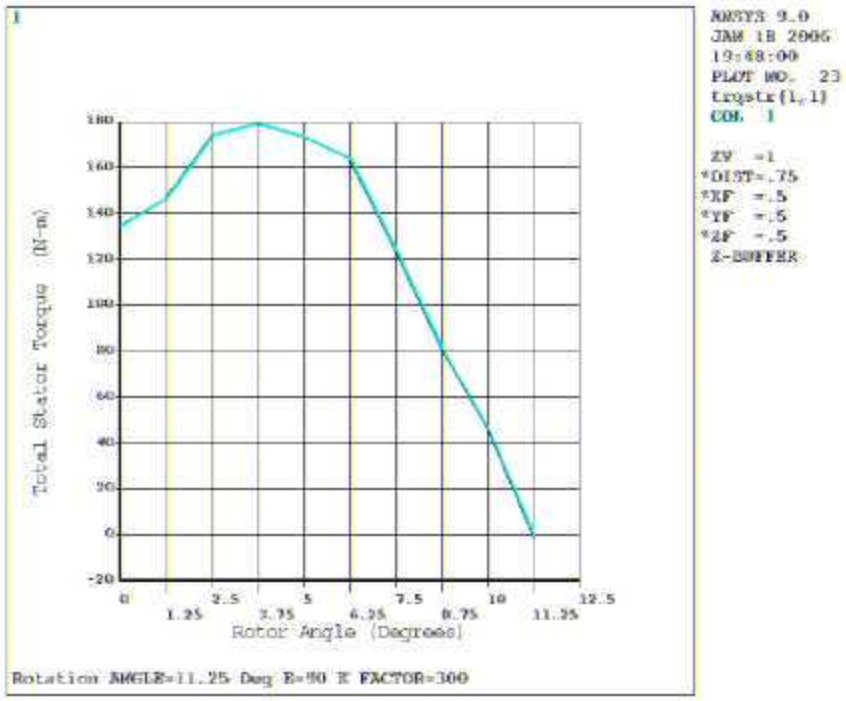


mag torq= 134.53 Rel Torq= 44.71 Total= 179.24

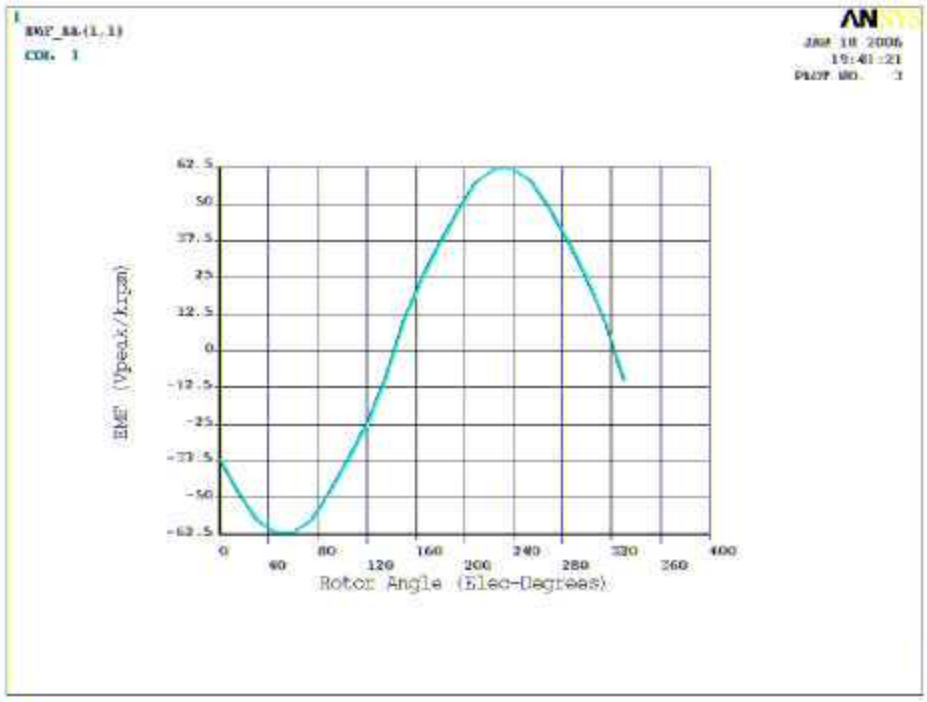


Iteration: EXP8

**Fig. 31. Single U-barrier, three bridges, two magnets, 95% pole coverage – torque profile and back-EMF.**

The geometry used to model the torque characteristics of the "double U-barrier with thre bridges" design is illustrated in Fig. 32, along with the flux line plot from FEA output. This configuration was modeled to weigh the possible advantages of having multiple flux barriers. The magnet weight was 3.06 lb, higher than the 2 lb standard, to keep the magnet thickness approximately the same as the previous U-barrier designs. Also, the magnet thickness at .110 in. is approaching the minimum magnet thickness for sintered magnets. Therefore, the only way to reduce magnet weight with two flux barriers is to reduce the size of the rotor, which has been set to a fixed value for this study.

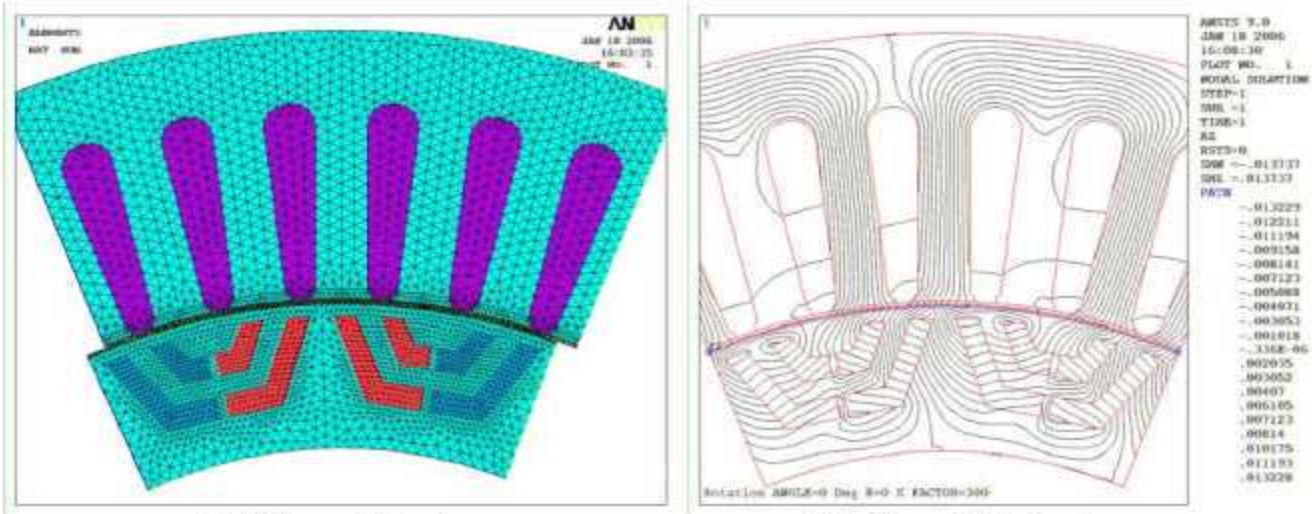

**FEA Element Mapping** **Flux Lines, Under Load**

**Wt_rtr = 8.02 lb wt_mag = 3.06 lb Pole Coverage = 90%**
**Iteration: EXP6**

**Fig. 32. Double U-barrier, three bridges, four magnets per pole.**

Figure 33 illustrates the torque profile and back-EMF waveform calculated for the "double U-barrier, three bridge design." This configuration produced 185 Nm of peak torque at 20° of phase advance and 1200 A-t of current in the windings. This is down from 220 Nm for the single U-barrier design with 80% pole coverage (Fig. 29). At 0° of phase advance, 144 Nm of magnet torque is produced, up from 114 Nm of magnet torque for the single U-barrier design with 80% pole coverage. Therefore, although magnet torque is up, reluctance torque has been reduced because the reduced thickness of the permeable path in the rotor causes more magnetic saturation. The back-EMF waveform shape is also close to sinusoidal (containing low harmonic content) compared with the other designs with 80% pole coverage.

The double barrier design could possibly be more effective with designs that allow a greater iron thickness between the magnets in the rotor. This could be accomplished with designs that are larger or have a lower pole count allowing surface across the pole. However, the double-flux barrier design will require more magnet material than a similar single barrier design increasing the weight and cost of the magnets. With the poor performance in this demonstration and the desire to use a high pole count and small size, it does not seem like multiple barriers will be a reasonable option for the final design.

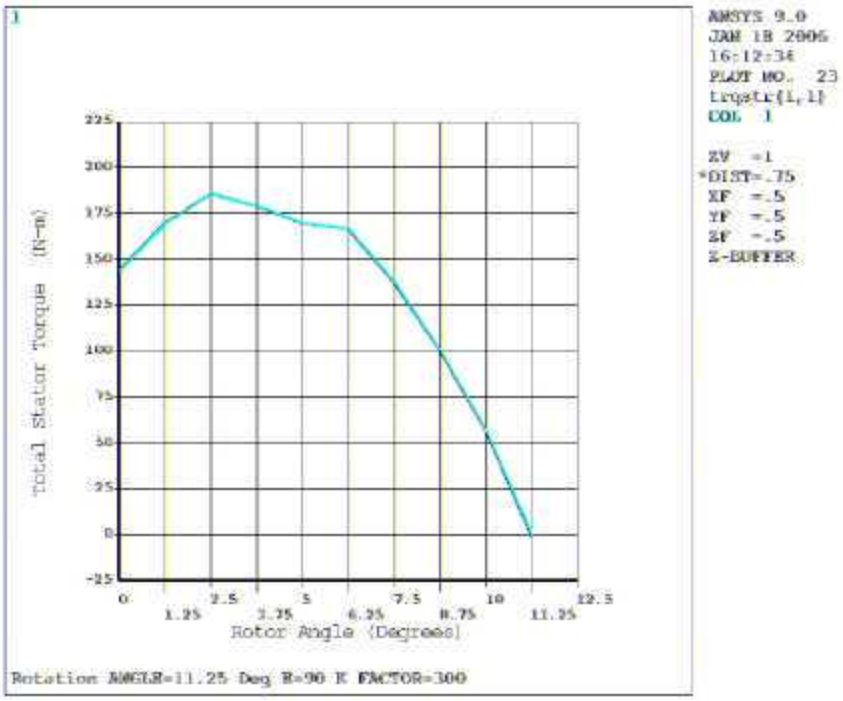


mag torq= 144.16 Rel Torq= 41.49 Total= 185.65

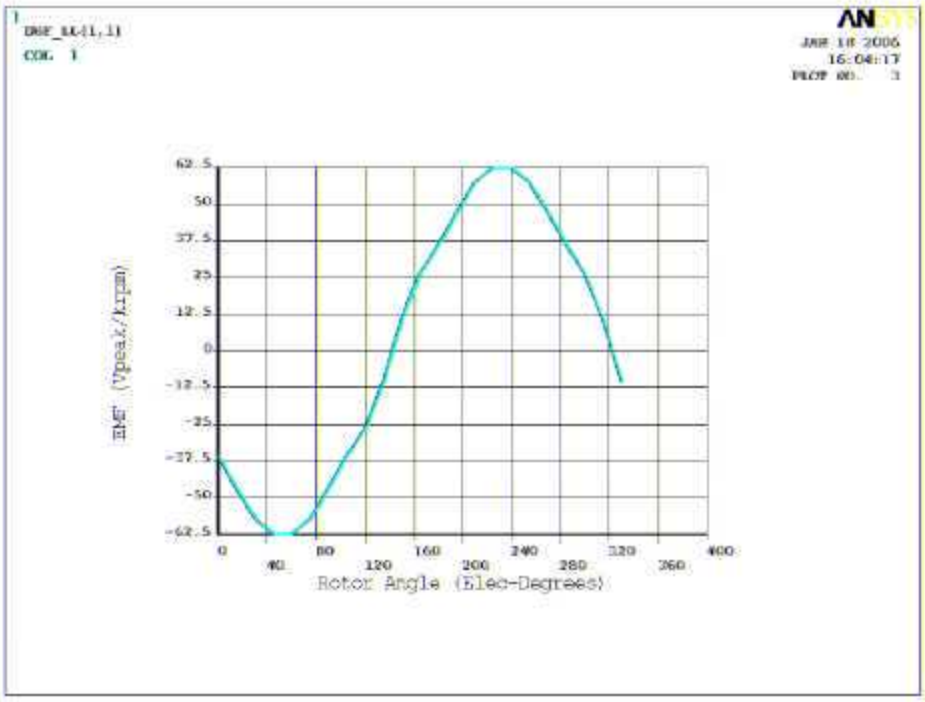


Iteration: EXP6

**Fig. 33. Double U-barrier, three bridges, four magnets per pole – torque profile and back-EMF.**

The geometry used to model the torque characteristics of the "single U-barrier with four bridges" design is illustrated in Fig. 34, along with the flux line plot from FEA output. This configuration was modeled to allow magnet shapes that are economically feasible to produce as sintered magnets. Also, four bridges will allow high strength at high speeds and the ability to carry larger magnets. The magnets in this design were consistent with the 2 lb standard, weighing only 1.92 lb. The rotor weight was 9.18 lb.

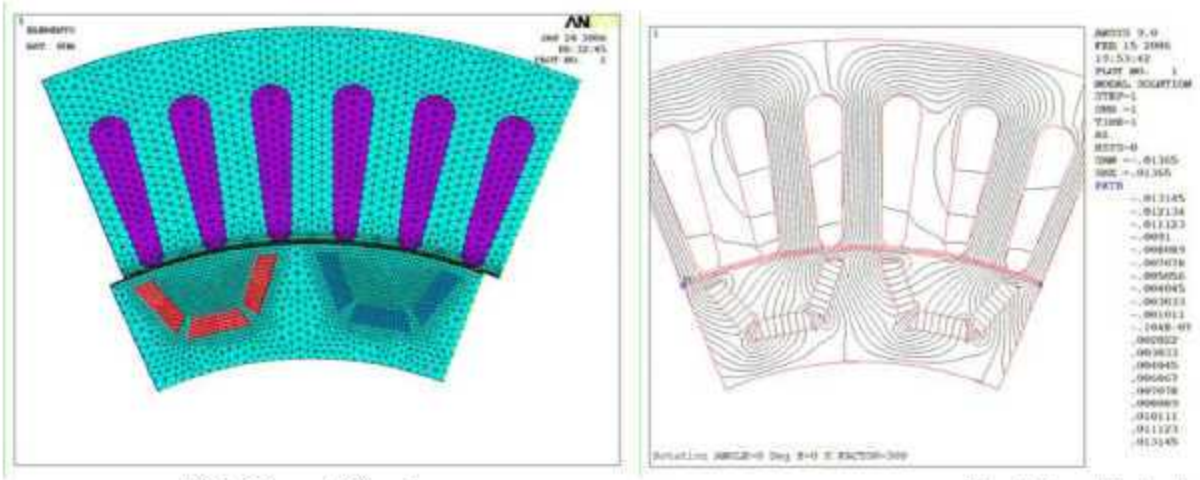

**FEA Element Mapping** **Flux Lines, Under Load**

**Wt_rtr = 9.18 lb wt_mag = 1.92 lb Pole Coverage = 80%**
**Iteration: EXP11, FD1**

**Fig. 34. Single U-barrier, four bridge, three magnets per pole.**

Figure 35 illustrates the torque profile and back-EMF waveform calculated for the "single U-barrier, four bridge design." This configuration produced 219 Nm of peak torque at 30° of phase advance and 1200 A-t of current in the windings. This is among the most torque produced by any previous rotor configurations in this study. It compares well with the single U-barrier, three bridge design that made 220 Nm with one less bridge (Fig. 29). At 0° of phase advance 110 Nm of magnet torque is produced, giving this design a good ratio of magnet to reluctance torque.

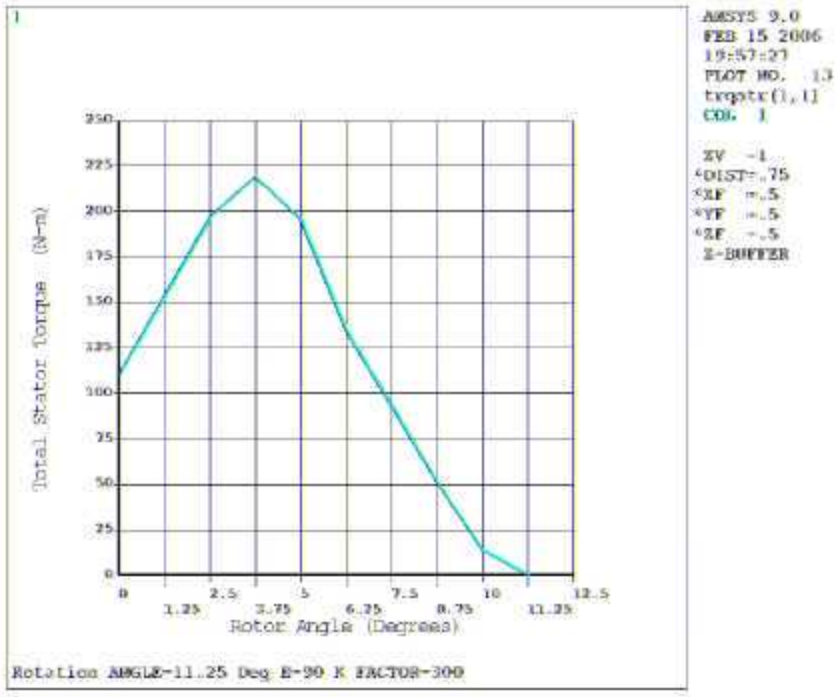


Mag torq= 110.65 Rel Torq=108.36 Total= 219.01

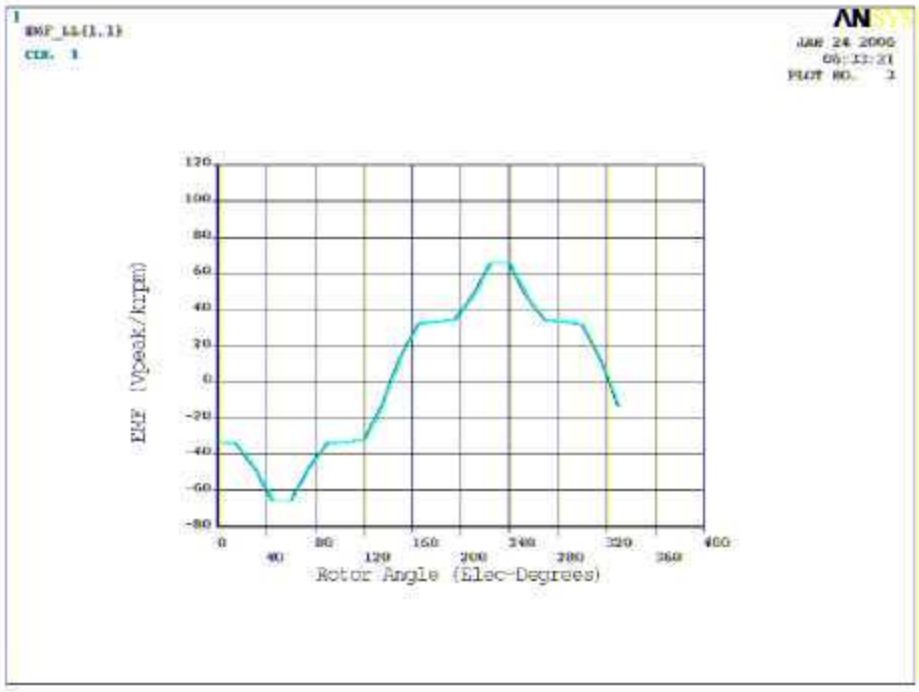


Iteration: EXP11, FD1

**Fig. 35. Single U-barrier, four bridge, three magnets per pole – torque and EMF profile.**

The geometry used to model the torque characteristics of the "single U-barrier with four bridges and non-uniform magnets" design is illustrated in Fig. 36, along with the flux line plot from FEA output. This configuration was modeled to allow a deeper U-shape than the previous design. The lower magnets in this design have been given a different length than the magnets on the sides of each pole, to allow a deeper U-Shaped barrier without a lot of change in magnet weight. The magnet weight was 2.03 lb increasing from 1.93 lb in the previous design with one uniform magnet size and shape for all of the magnets. This configuration with varying magnet shapes would require more tooling and assembly cost.

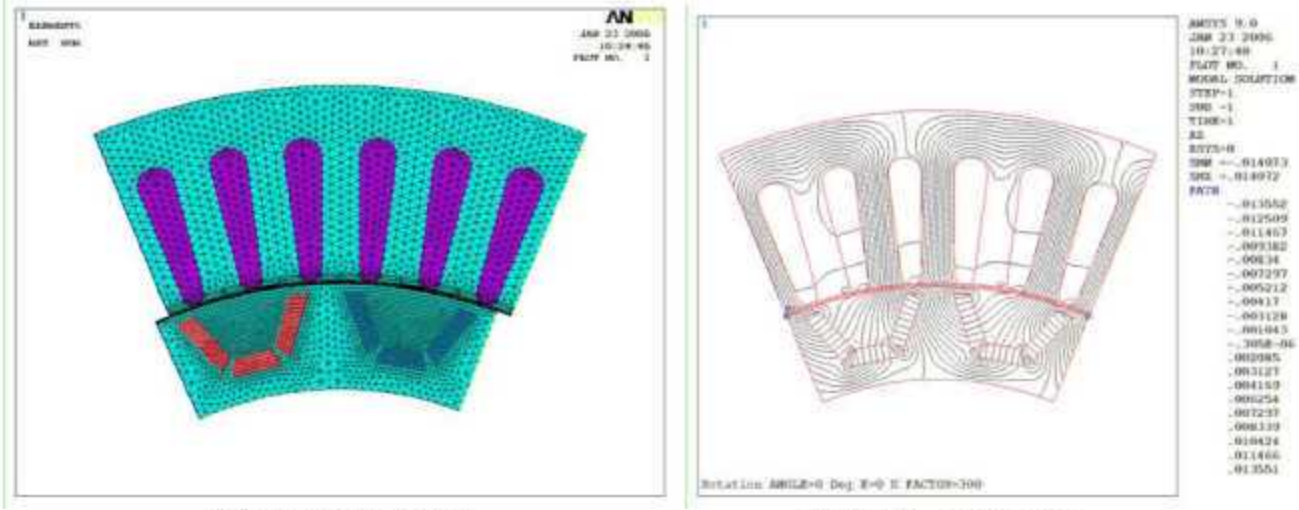

**FEA Element Mapping** **Flux Lines, Under Load**

**Wt_rtr = 9.07 lb wt_mag = 2.03 lb Pole Coverage = 80%**
**Iteration: EXP10**

**Fig. 36. Single U-barrier, four bridges, three magnets non-uniform magnets.**

Figure 37 illustrates the torque profile and back-EMF waveform calculated for the "single U-barrier, four bridge design with non-uniform magnets." This configuration produced 230 Nm of peak torque at 30° of phase advance and 1200 A-t of current in the windings. This is 11 Nm higher than the previous design with uniform magnets (Fig. 35). Although there was a decent gain, this configuration does use slightly more magnet material and has non-uniform magnets that may be more expensive.

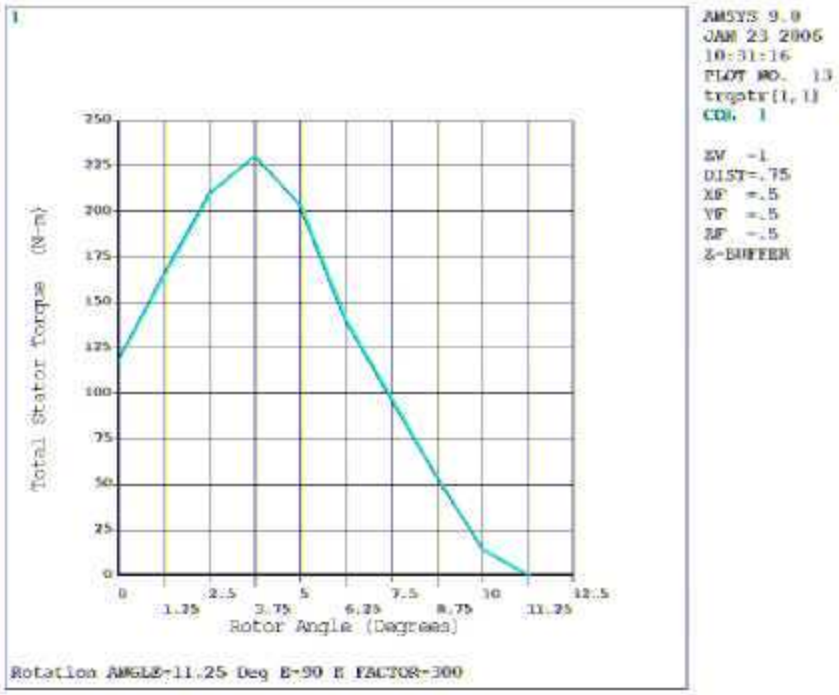


mag torq= 118.39 Rel Torq=111.86 Total= 230.25

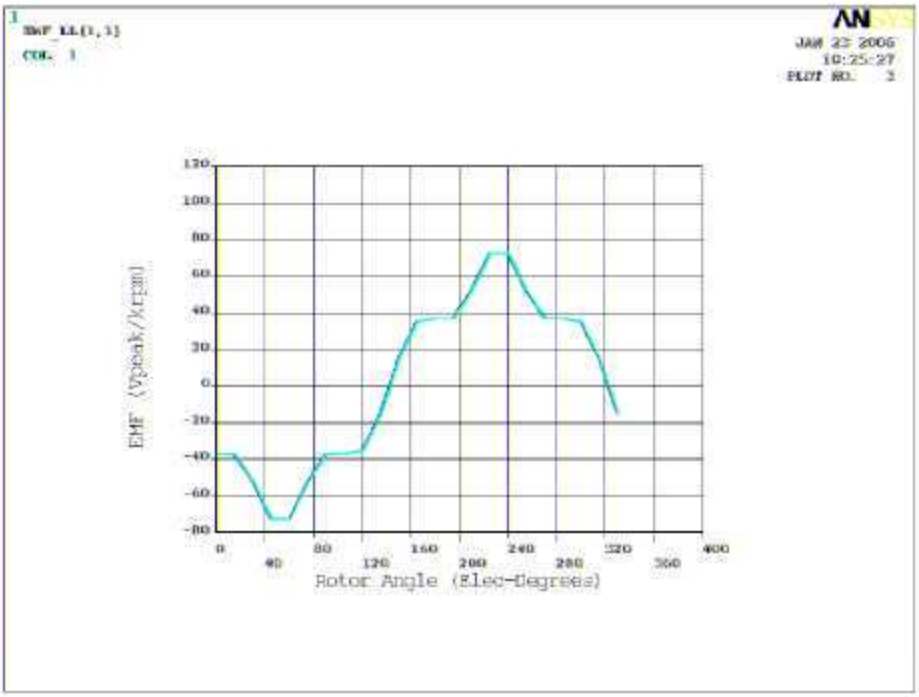


Iteration: EXP10

**Fig. 37. Single U-barrier, four bridges, three magnets (non-uniform magnts) – torque profile and back-EMF.**

The geometry used to model the torque characteristics of the "single U-barrier with two bridges" design is illustrated in Fig. 38, along with the flux line plot from FEA output. This configuration was modeled to determine the gains that can be realized by eliminating bridges. The tradeoff with eliminating bridges is obviously a decrease in strength. However, this design demonstrates how a two-Bridge design can be achieved at high speed. The U-shape is shallow so that the iron between the magnets has low mass. Also, the bridge varies in thickness and the magnets are shaped in such a way that their load is carried on the thicker part of the bridge. The magnet weight was 2.00 lb, and this design was checked structurally and determined to have less stress in the bridges than the V-barrier design discussed earlier in this section.

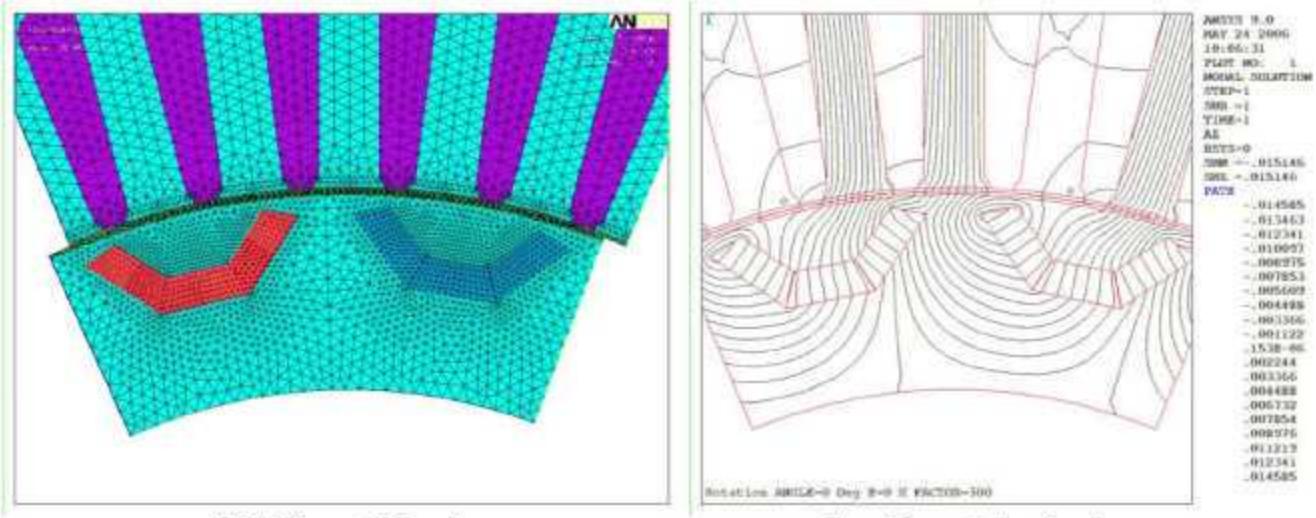

**FEA Element Mapping** **Flux Lines, Under Load**

**Wt_rtr = 10.43 lb wt_mag = 2.007 lb Pole Coverage = 80%**
**Iteration: FD6a**

**Fig. 38. U-barrier, two bridges, three magnets per pole.**

Figure 39 illustrates the torque profile and back-EMF waveform calculated for the "single U-barrier, two bridge design." This configuration produced 244 Nm of peak torque at 30° of phase advance and 1200 A-t of current in the windings. This is 30 Nm higher than the "baseline" V-barrier design (Fig. 27) and 25 Nm higher than the U-barrier with four bridges (Fig. 35).

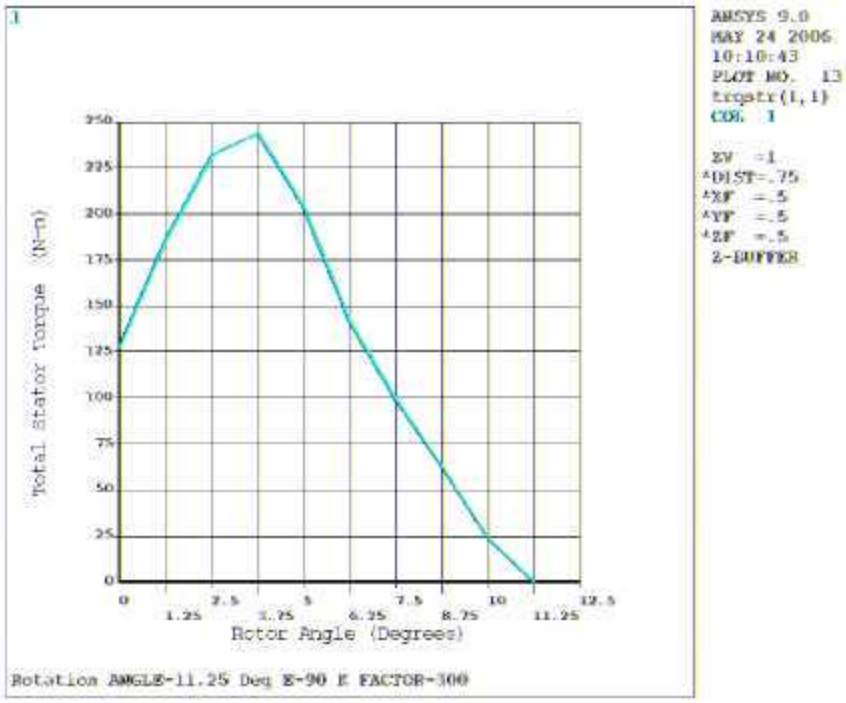


Mag torq= 128.17 Rel Torq=115.47 Total= 243.64

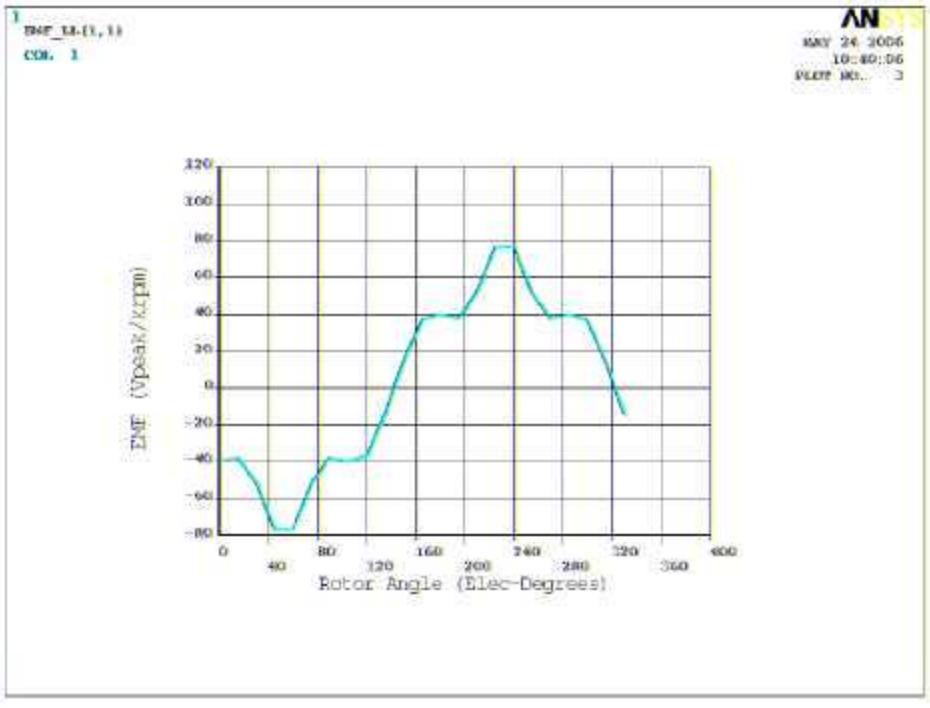


Iteration: FD6a

**Fig. 39. U-barrier, two bridges, three magnets per pole – torque profile and back-EMF**

## 4.3 CONCLUSIONS OF ROTOR CONFIGURATION STUDY

Figure 40 illustrates the torque profile for the three best rotor configuration candidates on the same chart. From this data, it is evident that the U-barrier with two bridges has the capability of providing a significant amount of more torque for the same size motor and same magnet mass. Alternatively, for a given torque this rotor configuration has the potential to yield a smaller motor with less magnet mass and/or total machine mass. The U-barrier with two bridges (Fig. 38) configuration provides approximately 15% more peak torque than the V-bBarrier design (Fig. 26) and 12% more peak torque than the U-barrier design with four Bridges (Fig. 34). Due to the apparent size reduction capability of the U-barrier with two bridges, this configuration will be slated for use in the final design.

The U-barrier with four bridges and non-uniform magnets also provided a high torque profile (Fig. 36), but not as high as the U-barrier with two bridges. Also, the non-uniform magnet sizes in this design could lead to more cost than the other designs where the shape of every magnet is the same. The U-barrier configurations with three bridges were mostly academic in nature and really did not represent a practical rotor construction. The most similar four-bridge configuration only yielded one Nm less than the comparable three-bridge configuration (see Fig. 28 and Fig. 34). The three-bridge configurations were also used to experiment with pole coverage. Although a much more sinusoidal back-EMF waveform with low harmonic content can be achieved with greater pole coverage, reluctance torque is also greatly diminished with increased pole coverage.

A three-bridge double-flux barrier configuration was also considered in this study. It was determined that this configuration does not scale down well to small machine sizes with sintered magnets and higher pole counts. The design considered here utilized .110 in. thick sintered magnets, which become very difficult to produce and handle when less than .100 in. thick. This thickness as well as the high pole count left little room on the rotor for permeable paths capable of generating significant reluctance torque (see Fig. 32). In addition, this design utilized more total magnet weight than the others. Therefore, to lower the pole count of the machine and/or increase the size in order to effectively use a double barrier would defeat the major goals of downsizing the machine and using less magnet mass.

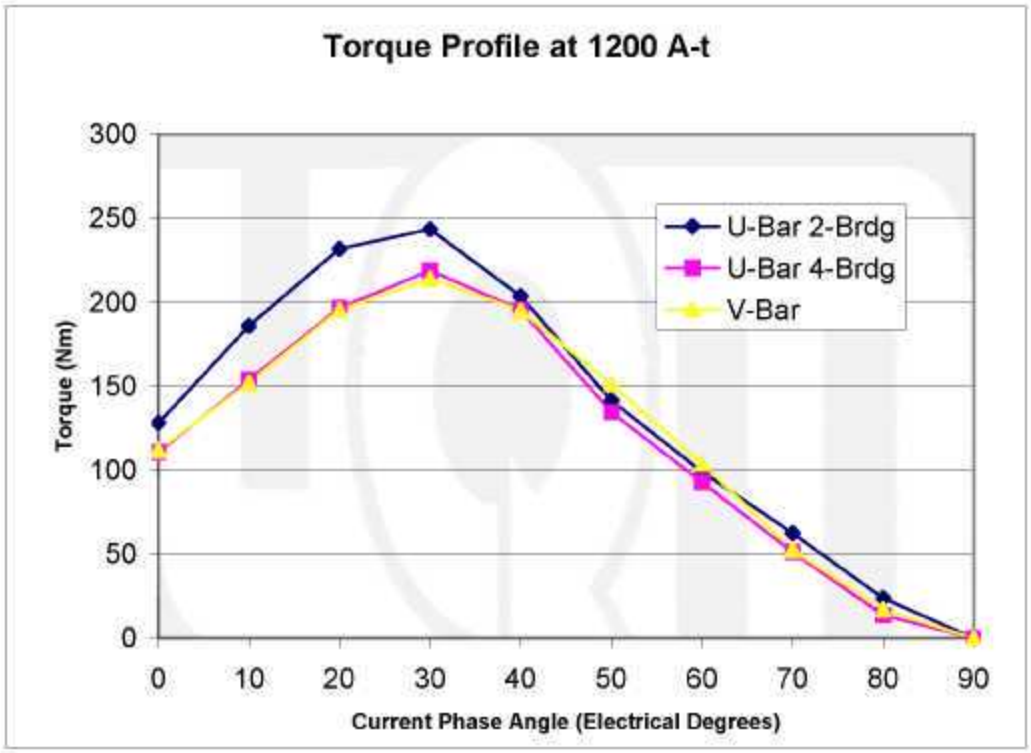


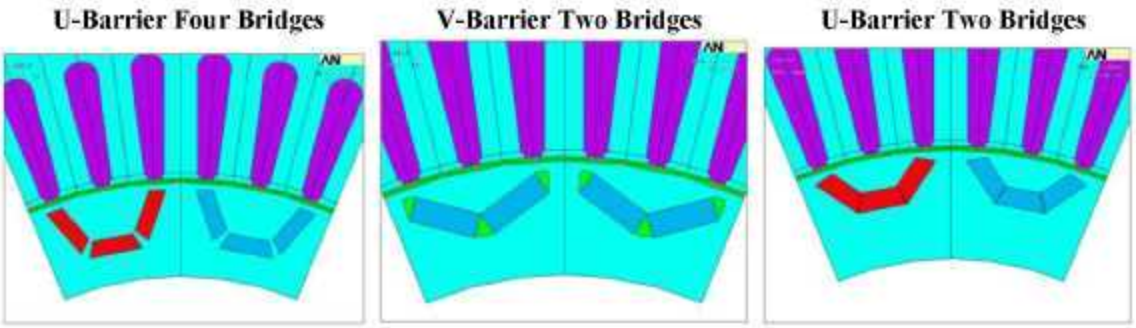


**Fig. 40. Torque profiles of the top three rotor configurations.**

# 5. DESIGN ITERATIONS

Many design iterations were generated in the development of the final design. There are too many of them to present them all here; the published design iterations in this section illustrate the pros and cons of the possible pole count selections. Other design iterations that were not published were generated with a varying amount of analysis. For example, if the torque profile for a given design iteration is not acceptable, the design iteration would be dropped without further analysis. Analysis is performed on a given design iteration until it is found to be unacceptable or it is apparent that improvements can be made.

## 5.1 ITERATIVE DESIGN METHOD

All simulations in this section and following sections are conducted assuming an operating temperature of 150°C. This temperature was chosen as a target steady state design point considering that 105°C is the required maximum inlet temperature and 150°C will allow for a reasonable temperature rise. All design iterations presented here were adjusted such that the maximum required torque, 262 Nm, is reached with 400 Arms leg current. The maximum allowable current according to the specification is 400 Arms, see Table 4. Designs were adjusted in length or turns to make 262 Nm at the maximum current to minimize the inductance and allow peak performance down to 200 V supply voltage. Higher turn counts and inductance will bring down the current but will not allow low voltage operation.

Motor performance was predicted through means of evaluating the motor parameters, inductance profile (q- and d-axis inductance vs. current), and torque mapping in FEA. These values were then used in conjunction with vector analysis to predict motor performance. The design equations were not used to predicted torque, given that they have no means of accounting for magnetic saturation at various current-phase angles and with complex geometry. For this reason, the torque map was generated in FEA to assure that saturation was properly accounted for. The performance models calculated the necessary current at a given operating point from the torque maps. The vector diagram was also evaluated for each point using the inductance values that corresponded to the current demand. The vector analysis determines what phase angle is necessary for operation at a given operating point and if the system will be voltage limited at that point.

## 5.2 EIGHT POLE-PAIR DESIGN ITERATIONS

The requirement for full power operation down to 200 V of supply voltage drove the selection of many design features and contributed in determining the pole-pair selection as well. UQM took the approach that the highest pole count that would still allow the efficiency and power requirements to be met would lead to the most compact and power dense design, saving materials and cost. Therefore we started with eight-pole pairs, a relatively high pole count for a 10 krpm machine. Some of the reasons that a high pole count leads to smaller size and greater performance include:

1. End-turn length is reduced because coil pitch is lesser at higher pole counts.
    a. End-turn length greatly affects volume of the motor.
    b. It also affects the overall axial space that the motor takes in the system.
2. Less magnet weight per pole allows bridges to be fewer and smaller.
    a. Smaller bridges provide less flux leakage from the magnets.
    b. Smaller/fewer bridges also provide more saliency and reluctance torque.
3. Smaller back-iron thickness allows lower stator weight and better thermal characteristics.
    a. Smaller stator back-iron thickness allows a shorter and less resistive thermal path from the winding to the heat sink.
    b. The stator weight is reduced overall with higher pole count designs.

The main drawback to high pole count deals with the higher iron losses that are a result of the higher frequency of the AC magnetic field in the stator which is induced by the magnets as the rotor turns. However, this loss can be controlled by increasing the nominal thickness of the magnetic path of the stator, which reduces the benefit listed above in (3). Although there is always a point of diminishing returns as a pole count increase, a higher pole count will nearly always give a net benefit in terms of power density so long as the other requirements can be accomplished, such as efficiency and the operating range for voltage, speed, and power. Furthermore, the fact that reluctance torque is utilized in this design will lessen the burden for high magnetic flux density from the field magnets.

Table 9 illustrates some of the important dimensions and machine parameters for the latest eight pole-pair design iteration.

**Table 9. Motor parameters, eight-pole pair, 3.3 length**

| | |
|---|---|
| Overall stator diameter (in.) | 8.6 |
| Inner stator diameter (in.) | 6.0 |
| Rotor outside diameter (in.) | 5.94 |
| Stator stack length (in.) | 3.3 |
| End-turn length | 0.670 |
| Total axial length (over the end-turns) (in.) | 4.64 |
| Tooth thickness (in.) | 0.305 |
| Back-iron thickness (magnet return path) (in.) | 0.400 |
| Magnet strength (residual induction Br) (T) | 1.10 |
| Magnet thickness (in.) | .110 |
| Magnet weight (lb) | 1.73 |
| Minimum bridge thickness (in.) | .055 |
| Torque density (Nm/Liter)** | 63.3 |
| Power density (kW/Liter)** | 12.5 |
| Winding turns | 3 |
| Slots per pole | 3 |
| back-EMF constant (Vpeak/krpm L-L) | 58 |
| Winding fill factor (%) *** | 77 |
| Winding resistance (Ohms L-L) | .0198 |
| q-axis inductance (μH L-L)* | 121 |
| d-axis inductance (μH L-L)* | 93 |

* Calculated using FEA at a 1200 ampere-turn load.
** Calculated using the Conservative Volume Calculation (see Fig. 4).
*** Includes insulation and copper in magnet wire, based sum of square areas.

The volume power density and torque density of this design was 12.46 kW/L and 63.3 Nm/L respectively. The low volume is attributed mostly to the very short end-turns and stack length.

The geometry and finite-element mesh for this eight pole-pair design iteration can be viewed in Fig. 41 below. This design is characterized by relatively thick stator teeth and return path iron, to control the iron losses at the inherently high frequencies for eight-pole pairs in the 10krpm speed range. The relatively small magnet thickness and low magnet weight are attributed to the high pole count as well.

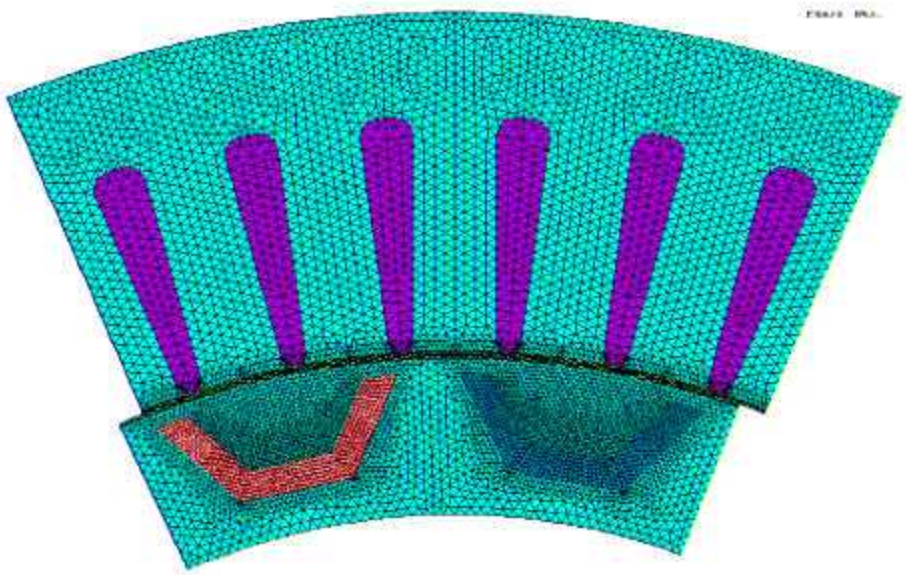

**Fig. 41. Eight pole-pair design geometry.**

Despite the high iron losses that comes with high pole count machines, the stator teeth and magnet back iron were adjusted such that the flux density was low enough to yield efficiencies of nearly 94% at 1000 rpm and 10 krpm over the 52 Nm requirement. Also, the motor efficiency peaked at roughly 96% at 4000 rpm (see Fig. 42).

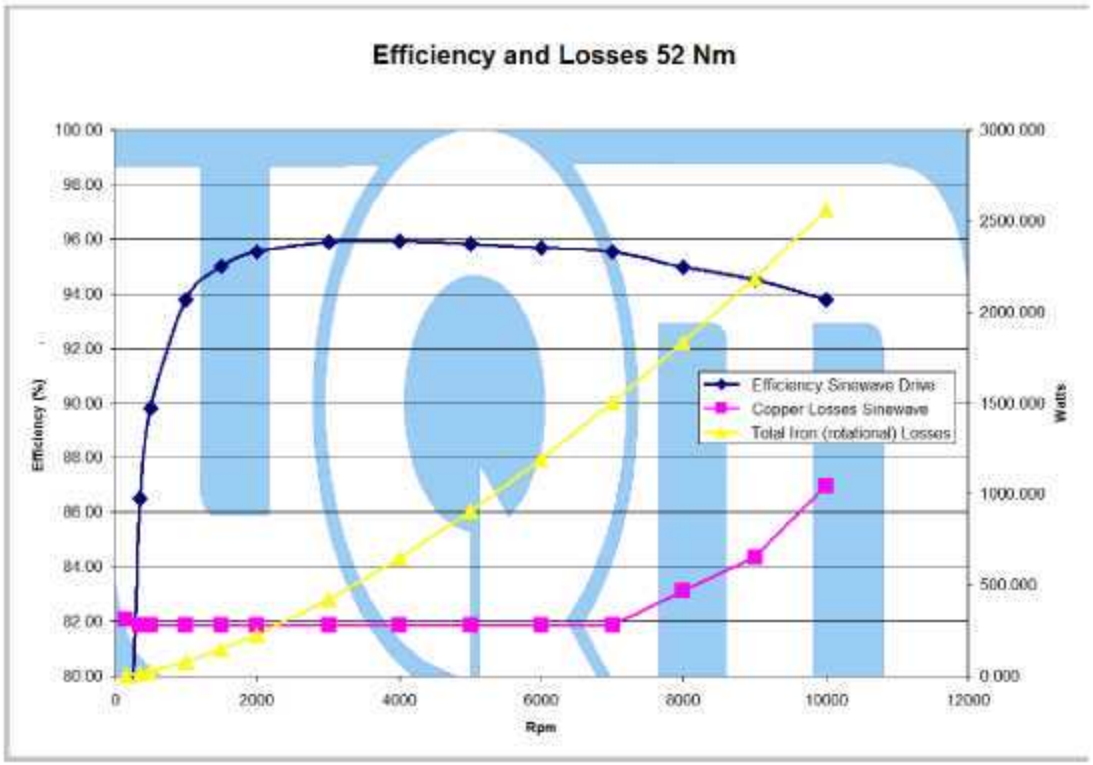


**Fig. 42. Efficiency, eight-pole pair, 3.3 in.**

However, this design iteration did not allow for full performance at 200 V. The following chart in Fig. 43, captures the voltage vector quantities for this design with a 3.3 in. stack length, operating at peak performance output (see Fig. 1 for peak performance curve). The chart illustrates the magnitudes of the voltage vectors with a 200 V supply over the full speed range.

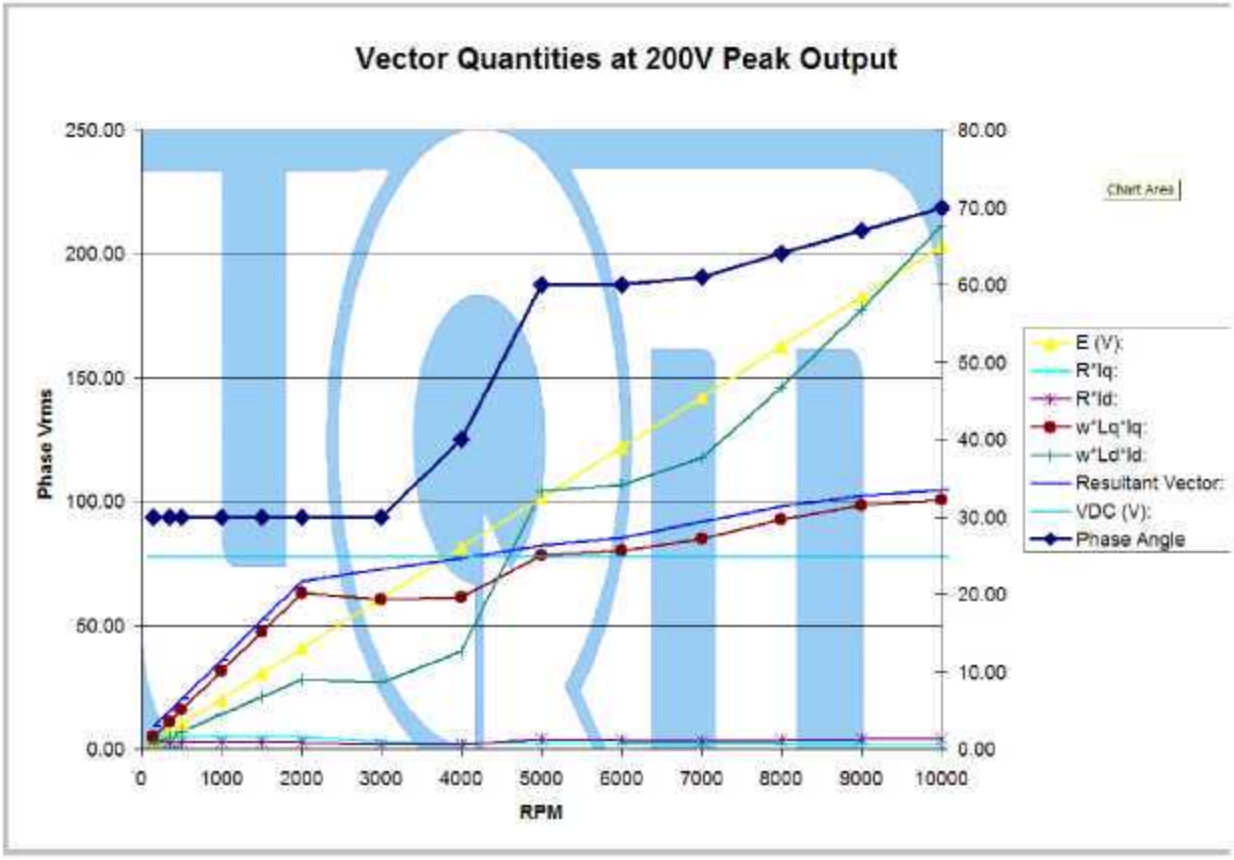


**Fig. 43. Vector quantities, eight-pole pair, 3.3 in.**

The solid blue line (resultant vector) represents the minimum voltage per phase required to operate at the given speed and at peak torque output. The solid cyan line (VDC) represents the per phase rms voltage available with a buss voltage of 200 Vdc. Note that at 4000 rpm, the blue line crosses above the cyan line indicating that the motor will require more than 200 Vdc to operate at peak output. The other blue line with the diamond marks (Phase Angle) indicates the phase angle needed to operate at the minimum voltage. In this simulation, the current-phase angle has been determined such that if it increases or decreases from this value, the minimum voltage will increase. It can be seen that the vector representing the reactance voltage from the q-axis component of the inductance (w*Lq*Iq) is significantly high, making it impossible to operate at 200 Vrms. This is true because it exceeds (VDC) line by itself at about 5000 rpm. This vector, along with the resistive voltage due to the d-axis current component (R*Id), represents one leg of a triangle whose hypotenuse is the resultant vector (or minimum operating voltage); see Fig. 44. Obviously, if this quantity exceeds the per phase voltage representing 200 Vdc by itself, peak output cannot be achieved. Therefore, the machine's q-axis inductance or the frequency (w) would have to drop to enable operation at 200 Vdc. To reduce frequency, the pole count would need to be reduced. Therefore, first an attempt was made to reduce inductance.

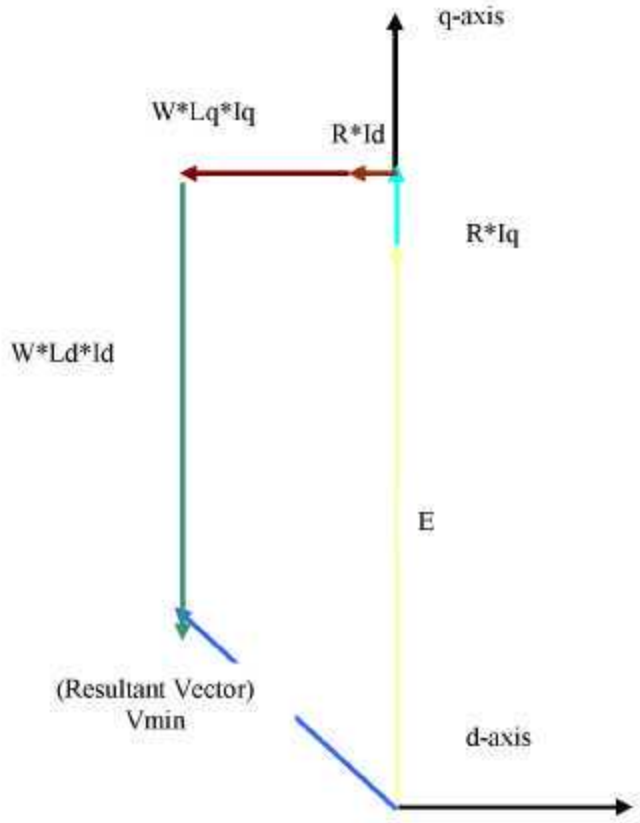


**Fig. 44. Second quadrant vector diagram.**

The inductance was reduced and this design could be modified to operate at 200 Vdc by decreasing the number of turns per slot from three down to two turns and by increasing the stack length from 3.3 in to 4.2 in. These change decreased the q-axis inductance from 121–68.4 uH. Unfortunately, with the increased length this change decreases the power density of the machine even though all other dimensions remained the same. The machine parameters for the 4.2 in. version are shown below in Table 10.

**Table 10. Motor parameters, eight-pole pair, 4.2 in. length**

| | |
|---|---|
| Overall stator diameter (in.) | 8.6 |
| Inner stator diameter (in.) | 6.0 |
| Rotor outside diameter (in.) | 5.94 |
| Stator stack length (in.) | 4.2 |
| End-turn length | 0.670 |
| Total axial length (over the end-turns) (in.) | 5.54 |
| Tooth thickness (in.) | 0.305 |
| Back-iron thickness (magnet return path) (in.) | 0.400 |
| Magnet strength (residual induction Br) (T) | 1.10 |
| Magnet thickness (in.) | .110 |
| Magnet weight (lb) | 2.20 |
| Minimum bridge thickness (in.) | .055 |
| Torque density (Nm/Liter)** | 49.7 |
| Power density (kW/Liter)** | 10.4 |
| Winding turns | 2 |
| Slots per pole | 3 |
| back-EMF constant (Vpeak/krpm L-L) | 48.5 |
| Winding fill factor (%) *** | 77 |
| Winding resistance (Ohms L-L) | .0102 |
| q-axis inductance (μH L-L)* | 68.4 |
| d-axis inductance (μH L-L)* | 52.5 |

*Calculated using FEA, at a 1200 ampere-turn load.
**Calculated using the Conservative Volume Calculation (See Fig. 4).
***Includes insulation and copper in magnet wire, based sum of square areas.

In addition to reducing the power density from 12.5 down to 10.4 kW/L, the efficiency was also reduced at high speeds dropping from more than 94% at 10 krpm to 93%: see Fig. 45. This design still meets the requirements for efficiency and peak power at 200 V (see Fig. 46); however, the power density dropped to less than what is desired for this design. Essentially, too many compromises needed to be made to make the eight pole-pair design meet the requirements, negating the benefits of the high pole count and indicating that eight-pole pairs fall within the realm of diminishing returns for this set of requirements. Note that in Fig. 46, the blue line vector quantity representing the minimum required voltage lies below the line for buss voltage (VDC) over the entire speed range.

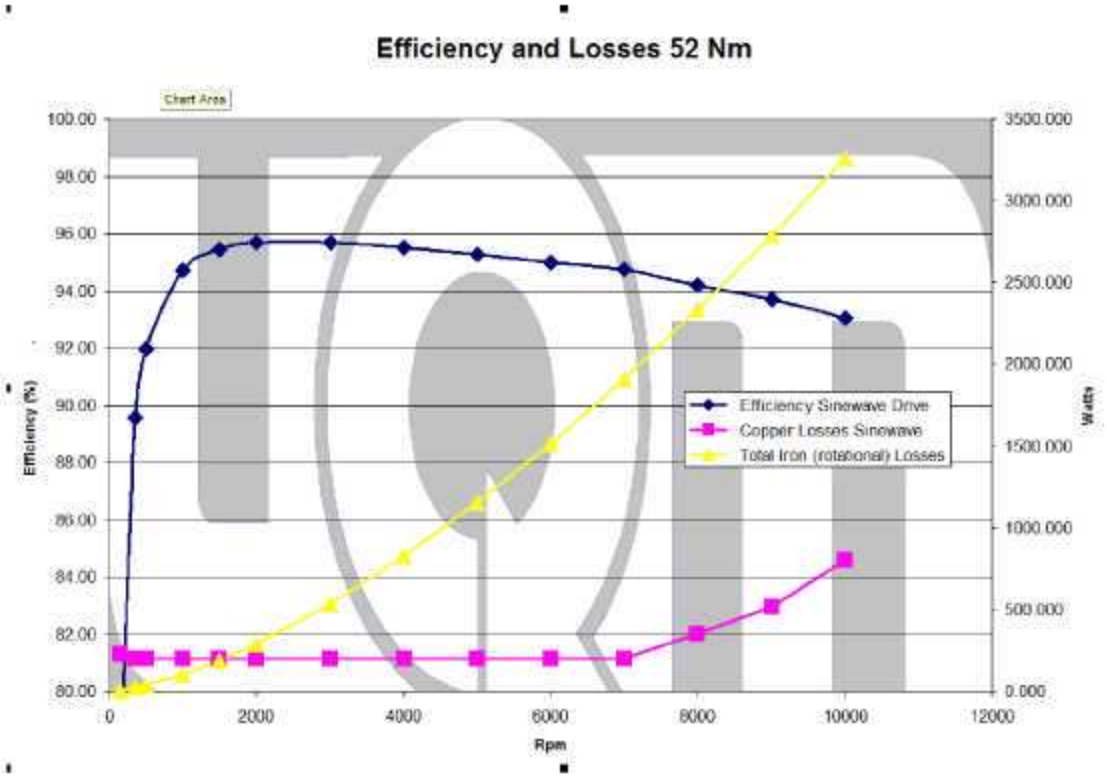


**Fig. 45. Efficiency, eight-pole pair, 4.2 in.**

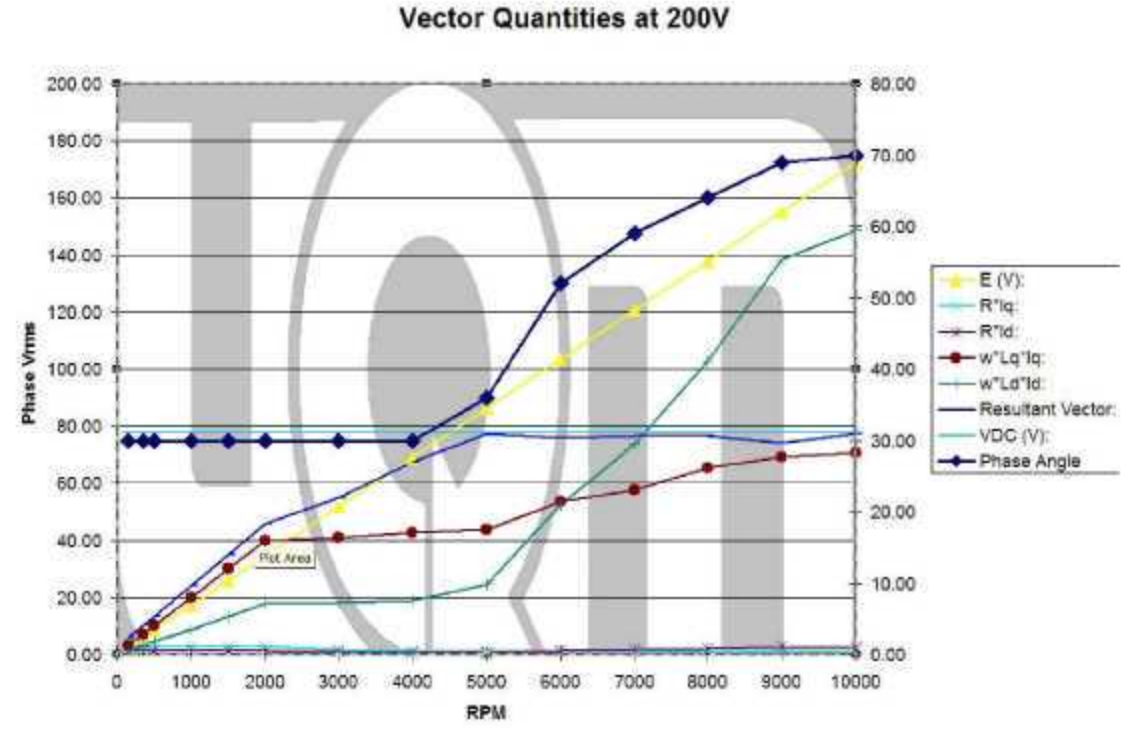


**Fig. 46. Vector quantities, eight-pole pair. 4.2 in.**

## 5.3 FOUR POLE-PAIR DESIGN ITERATIONS

The next step was to take a step back and determine if a four pole-pair design would meet the requirements knowing that the Prius motor and other motor designs have used this pole selection successfully. Although a four pole-pair design was generated in the trade study, that design was not intended to operate at full power down to 200 V. Therefore, the four pole-pair configuration was reiterated in order to meet that requirement. The resulting dimensions and motor parameters are displayed in Table 11.

**Table 11. Motor parameters, four-pole pair, 3.9 in. length.**

| | |
|---|---|
| Overall stator diameter (in.) | 8.865 |
| Inner stator diameter (in.) | 5.425 |
| Rotor outside diameter (in.) | 5.365 |
| Stator stack length (in.) | 3.9 |
| End-turn length | 1.20 |
| Total axial length (over the end-turns) (in.) | 6.30 |
| Tooth thickness (in.) | 0.25 |
| Back-iron thickness (magnet return path) (in.) | 0.52 |
| Magnet strength (residual induction Br) (T) | 1.10 |
| Magnet thickness (in.) | .165 |
| Magnet weight (lb) | 2.54 |
| Minimum bridge thickness (in.) | .055 (four bridges) |
| Torque density (Nm/Liter)** | 41.13 |
| Power density (kW/Liter)** | 8.63 |
| Winding turns | 3 |
| Slots per pole | 6 |
| back-EMF constant (Vpeak/krpm L-L) | 57.0 |
| Winding fill factor (%) *** | 77 |
| Winding resistance (Ohms L-L) | .0175 |
| q-axis inductance (μH L-L)* | 261 |
| d-axis inductance (μH L-L)* | 126 |

*Calculated using FEA at a 1200 ampere-turn load.
**Calculated using the Conservative Volume Calculation (See Fig. 4).
***Includes insulation and copper in magnet wire, based sum of square areas.

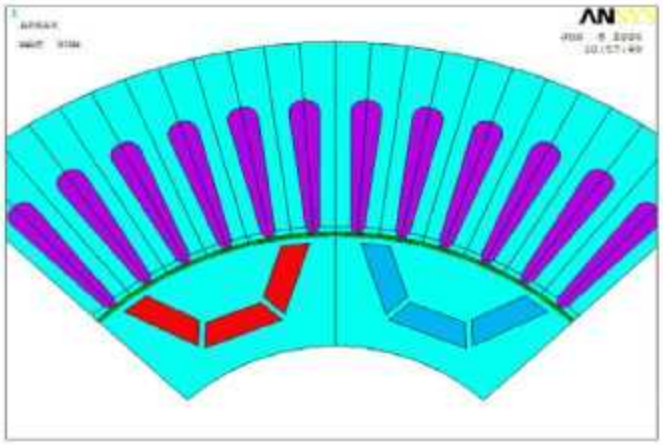

The motor design needed to be upsized from the original design generated in the trade study in order to produce the required torque at 400 Arms with a lower turn count. The turn count had to drop from four turns per slot to three to reduce the inductance and meet the 200 V requirement. The resulting design had an increased diameter and length from the magnet-dominant design in the trade study. The predicted end-turn length was characteristically high for a four pole-pair design, 1.2 in. All of these things contributed to a relatively low power density, 8.6 kW/L.

Also notable is that the rotor needed to employ four bridges in order to hold larger magnets and the total magnet weight exceeded 2.5 lb.

The efficiency of this four pole-pair design met the efficiency requirements at 52 Nm across the speed range. The efficiency at 1000 rpm was slightly above 95% and slightly below 95% at 10 krpm. The chart shown in Fig. 47 illustrates the efficiency and loss profile for this design.

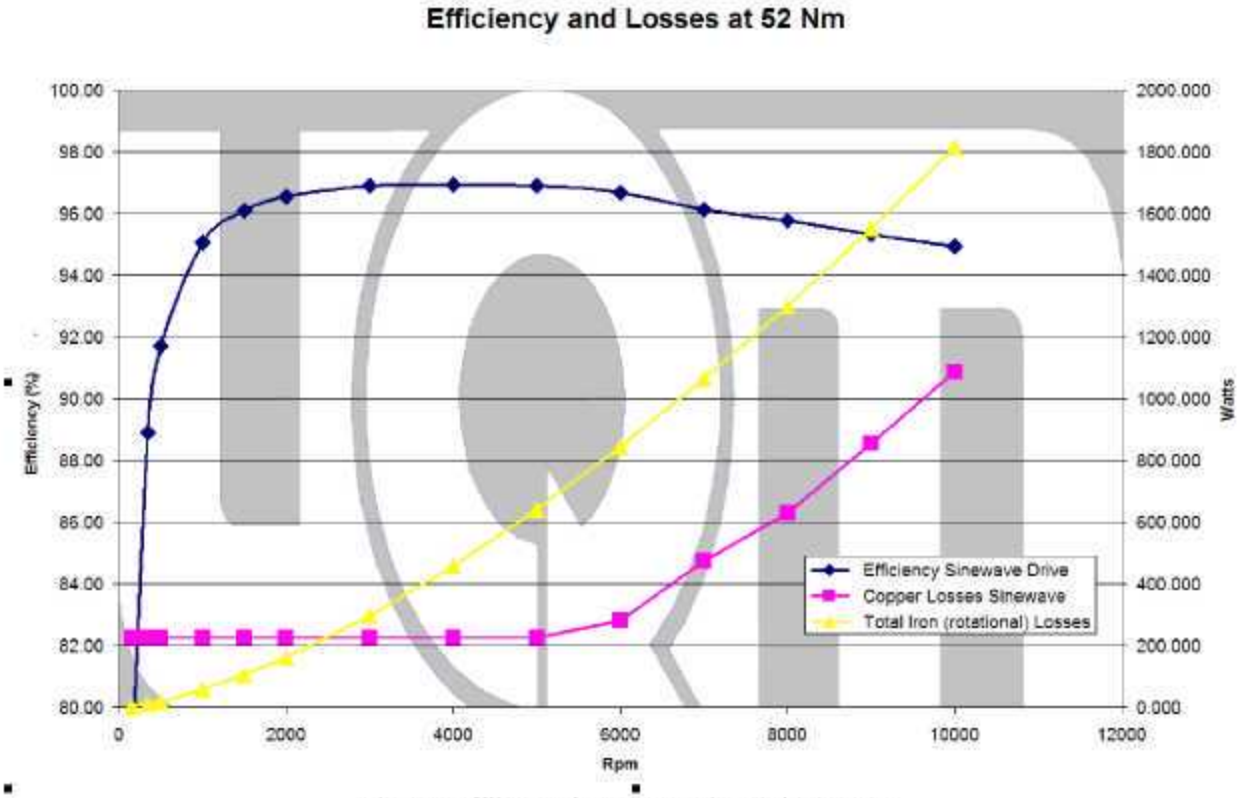


**Fig. 47. Effiiency, four-pole pair, 3.9 in. length.**

This four pole-pair design does meet the requirement for full power at 200 V. Figure 48 illustrates the vector quantities as the machine operates along the peak-power profile (Fig. 1). Note that the minimum voltage required (Resultant Vector) remains below the 200 V per phase equivalent line voltage (VDC on the curve). This four pole-pair design was capable of operation at 200V even with a higher inductance, 261 uH, than the eight pole-pair design given the lower inherent operating frequency.

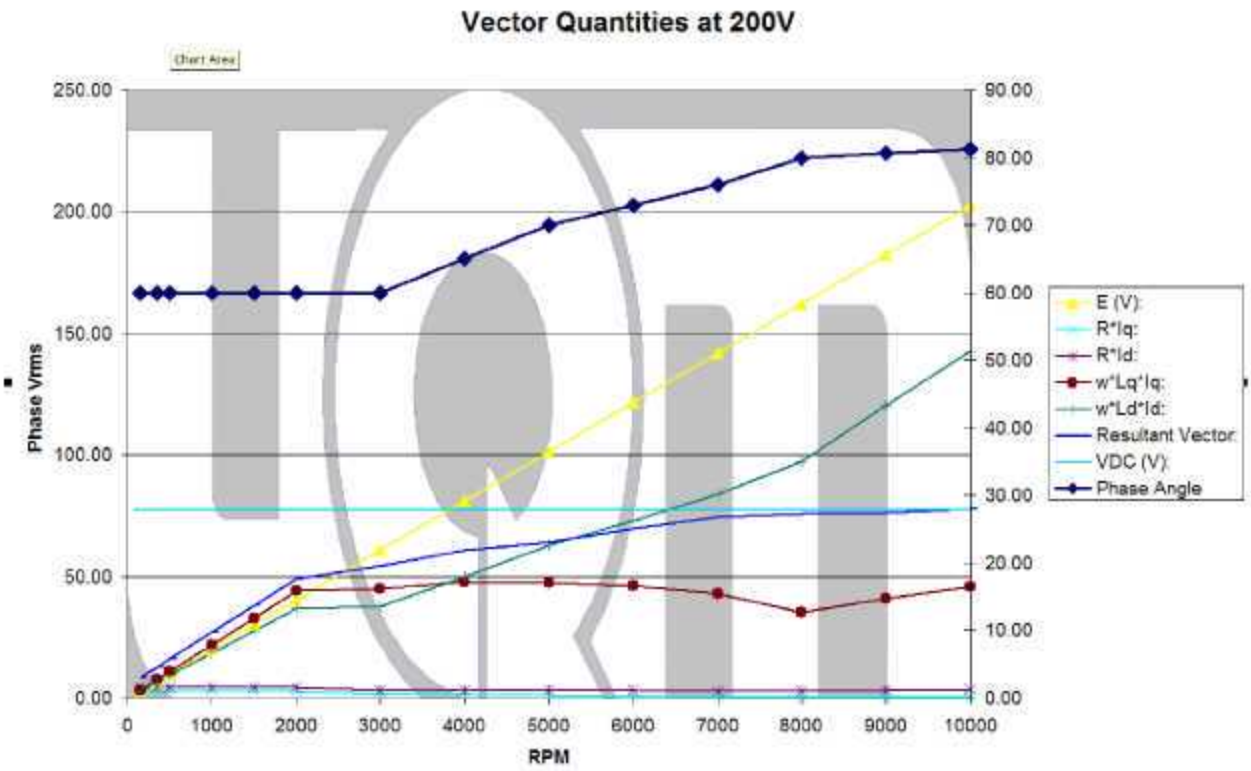


**Fig. 48. Vector quantities, four-pole pair, 3.9 in. length.**

## 5.4 SIX POLE-PAIR DESIGN ITERATIONS

Meeting the requirements of the specification at a higher power density, but a lower efficiency with the eight pole-pair design as compared with the four pole-pair design, prompted the study of pole-pair combinations between the two. The six pole-pair selection was a logical choice, having 36 slots in a three-slot per pole configuration that allows a simple winding and relatively short end-turns. Iterations of the six pole-pair design led to the final design proving to have a better efficiency and power density than the designs with the other pole combinations.

Table 12 lists the important parameters of the most recent six pole-pair design iteration that became the final design. This combination yielded short end-turns (.88 in.) and allowed a relatively short (3.4 in.) stack length as well. At 8.7 in. in overall diameter and a total volume of 5 liters, the power density is 11 kW/Liter (calculated conservatively as described in Fig. 4), better than the design iterations in either of the other pole configurations. This is with the exception of those designs that did not produce full power at 200 V.

**Table 12. Motor parameters, six-pole pair, 3.4 in. (final design)**

| | |
|---|---|
| Overall stator diameter (in.) | 8.7 |
| Inner stator diameter (in.) | 6.10 |
| Rotor outside diameter (in.) | 6.04 |
| Stator stack length (in.) | 3.4 |
| End-turn length | .88 |
| Total axial length (over the end-turns) (in.) | 5.165 |
| Tooth thickness (in.) | 0.380 |
| Back-iron thickness (magnet return path) (in.) | 0.39 |
| Magnet Strength (residual induction Br) (T) | 1.10 |
| Magnet thickness (in.) | .165 |
| Magnet weight (lb) | 2.21 |
| Minimum bridge thickness (in.) | .04 (2 bridges) |
| Torque density (Nm/Liter)** | 52.2 |
| Power density (kW/Liter)** | 11.0 |
| Winding turns | 3 |
| Slots per pole | 3 |
| Back-EMF constant (Vpeak/krpm L-L) | 47 |
| Winding fill factor (%) *** | 74 |
| Winding resistance (Ohms L-L) | .011 |
| q-axis inductance (μH L-L)* | 111 |
| d-axis inductance (μH L-L)* | 75 |

*Calculated using FEA at a 1200 ampere-turn load.
**Calculated using the Conservative Volume Calculation (see Fig. 4).
***Includes insulation and copper in magnet wire based sum of square areas.

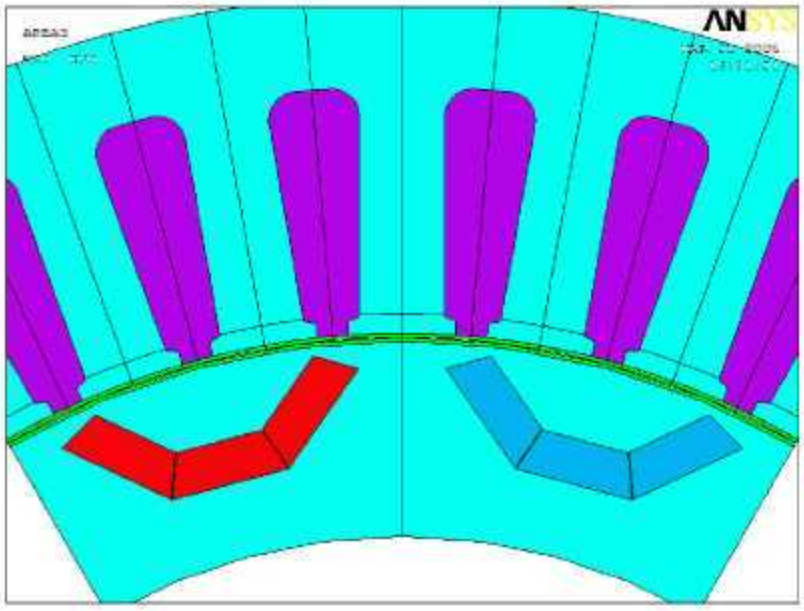

Relatively wide stator teeth (.380 in.) and back-iron (.390 in.) reduced flux density and helped to control iron losses giving good efficiency at high speeds. Figure 49 indicates that the motor will be 94.8% efficient at 1000 rpm and 95.6% at 10krpm, well above the efficiency target of 93%. The peak efficiency, 96.5% is reached at about 4000 rpm and 52 Nm.

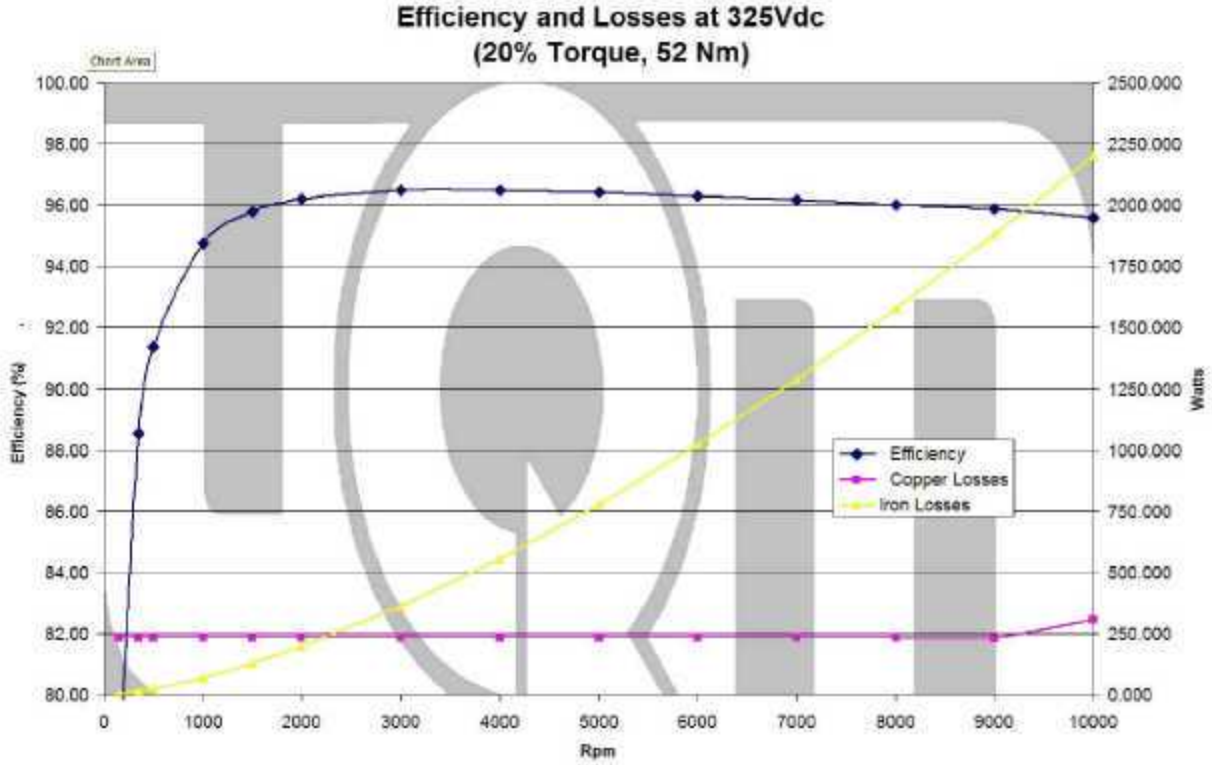


**Fig. 49. Efficiency, six-pole pair, 3.4 in. (final design).**

Also, the vector analysis indicated that operation at full power with a 200 V supply would be easily accomplished with this design. Referring to Fig. 50, the Resultant Vector or minimum voltage for operation can be maintained below the buss voltage (VDC) by phase advancing the current to a reasonable angle. The maximum angle for phase advance is 78° advanced from the back-EMF waveform. Also, current never exceeds the maximum allowable current of 400 Arms. Figure 51 plots the current at each speed along the peak power curve at 200 V.

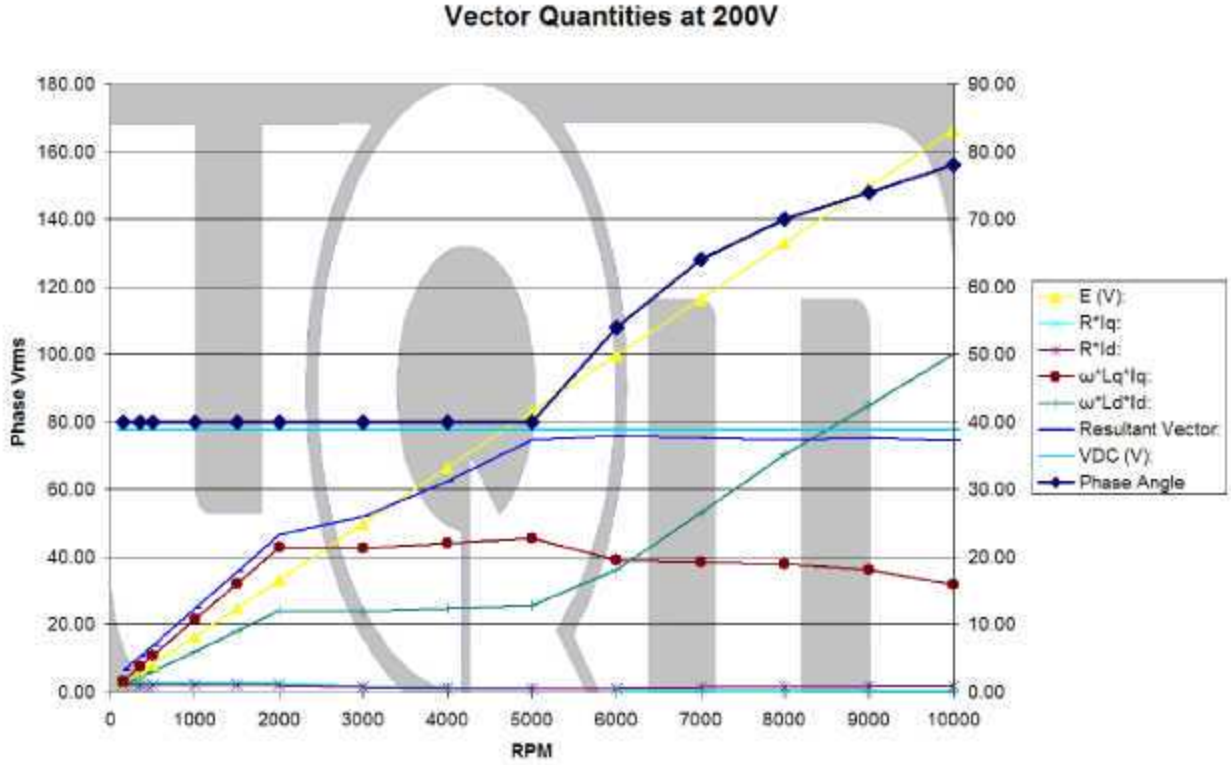


**Fig. 50. Vector quantities, six-pole pair, 3.4 in. (final design).**

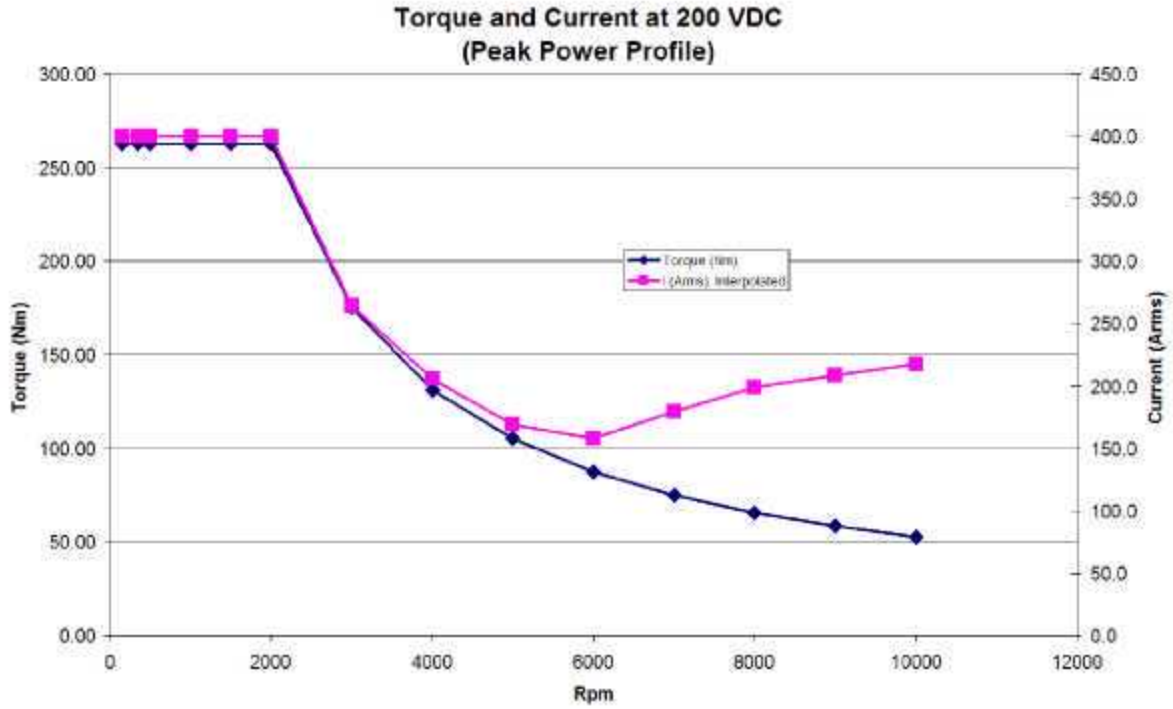


**Fig. 51. Current profile at 200 VDC, peak power.**

## 5.5 CONCLUSIONS

Although the eight pole-pair version was able to meet most of the performance specs, the girth of the iron in the magnetic circuit and the length had to be increased until the weight and volume were higher than expected. The tooth width and return path thickness had to be increased to lower flux density and therefore the iron losses. Even so, this design barely met the 93% specification at 10 krpm. In addition, the turn count was dropped from three down to two to lower the inductance and allow performance down to 200 V. The length was increased to compensate for the loss of a turn. Although the end-turns are the shortest of all the designs (.68 in.), the stack length was the longest (4.2 in.). Although higher pole counts do give a benefit in terms of size, there is a point at which raising the pole count will result in diminishing returns. The conclusion is that the designs with eight-pole pairs will result in diminishing returns for this set of specifications.

The next step was to fall back to four-pole pairs, a pole configuration that has been used in the Prius and other similar applications. The results of these design iterations were as expected. The four pole-pair design was able to meet the performance specs in terms of efficiency, peak power and voltage range of operation. However, the resulting volume and weight were too high making the power and torque densities low. Larger volume and weight are partially due to inherently longer end-turns and requirement for thick stator features. More copper, iron, and magnet are necessary to compensate for less EMF because of the lower frequency operation in comparison to the higher pole counts. Additionally, because there is more magnet weight per pole, more structural support is needed to retain the magnets at high speeds. Consequently, the bridge thickness needs to be greater. With more bridges and/or thicker bridges, more magnet flux is shunted away from the stator, reducing performance.

We decided to investigate the pole-pair combination between four- and eight-pole pairs. Six-pole pairs proved to be a good compromise between the two. Magnet weight was the lowest and the power density was the best of the three: 11.0 kW/L for six-pole pairs, 10.4 kW/L for eight-pole pairs and 8.6 kW/L for four-pole pairs. (These power densities are based on the conservative volume calculation: see Fig. 4.)

# 6. FINAL DESIGN EXTENDED ANALYSIS

## 6.1 DESIGN FEATURES IMPLEMENTED

Some of the design features implemented in the final design which aid in meeting the performance and cost targets are indicated in Fig. 52 and include:

(1) Magnets with locking features for redistributing the centrifugal force of the magnet mass and allowing thin bridges (see Section 6.5 for detailed description).
(2) Thick stator teeth and back-iron for low flux density and iron losses.
(3) Relatively large slot opening for machine winding compatibility.
(4) Radius in slots for reduced flux concentration.
(5) Small stator diameter 8.7 in. and stack length 3.4 in. for reduced cost of material consumption and space claim.

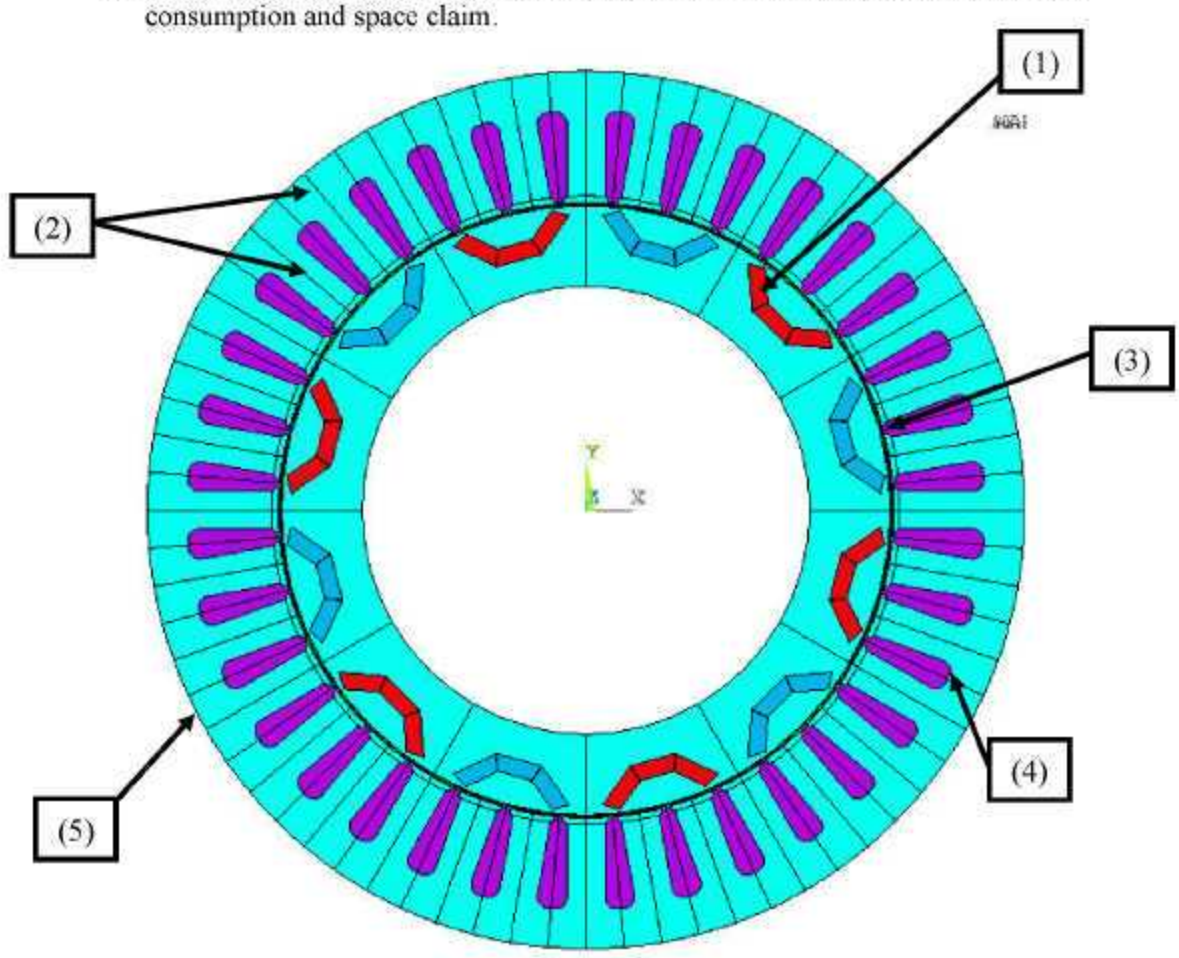


**Fig. 52. FCVT final design, physical features.**

The materials used for the electromagnetic components of the final design include the following.

(1) M19 29 gage lamination steel for the rotor and stator,
(2) Sintered NdFeB magnets with 1.1 Tesla Residual induction at 20 C,
(3) Inverter Grade magnet wire, and
(4) H-Class insulation system.

Figure 53 illustrates the flux line contours for the magnetic circuit in the final design. This flux line contour includes the flux induced by the magnets only; winding induced flux is not included in this simulation. The flux density in the teeth and stator back iron are used to calculate the iron losses of the motor as a function of speed.

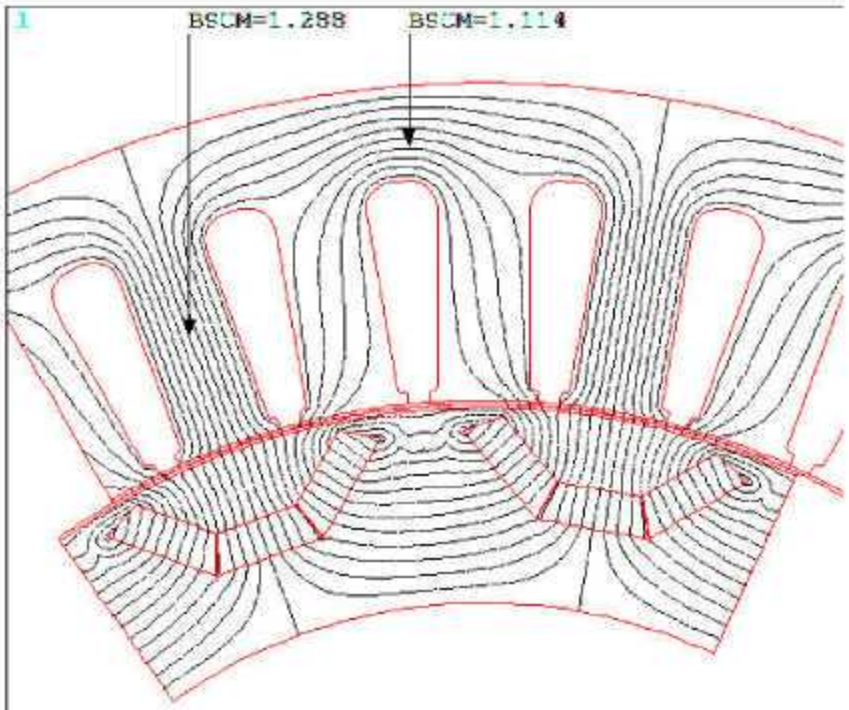


**Fig. 53. Final design, magnet induced flux contours.**

## 6.2 TORQUE ANALYSIS

The torque for an interior PM motor (IPM) varies greatly with the phase angle of the current as it is advanced with respect to the back-EMF as well as with the magnitude of the current. Therefore, to accurately model the behavior of an IPM machine, the torque profile must be mapped across phase angles from 0–90 electrical degrees phase advanced from the EMF. This must also be done at a variety of currents within the operating range, using FEA and the nonlinear B vs. H curves to account for magnetic

saturation (see Fig. 54). This information, along with the inductance profile (Section 6.3) is used to produce the efficiency and loss simulation (see Fig. 49) and the vector analysis simulation (see Fig. 50). From Fig. 54 it can be seen that the maximum torque occurs at 40° of phase at all of the current levels. For this reason, the vector analysis in Fig. 50 starts at 40° and increases only when a higher phase angle is needed to control the minimum voltage requirement.

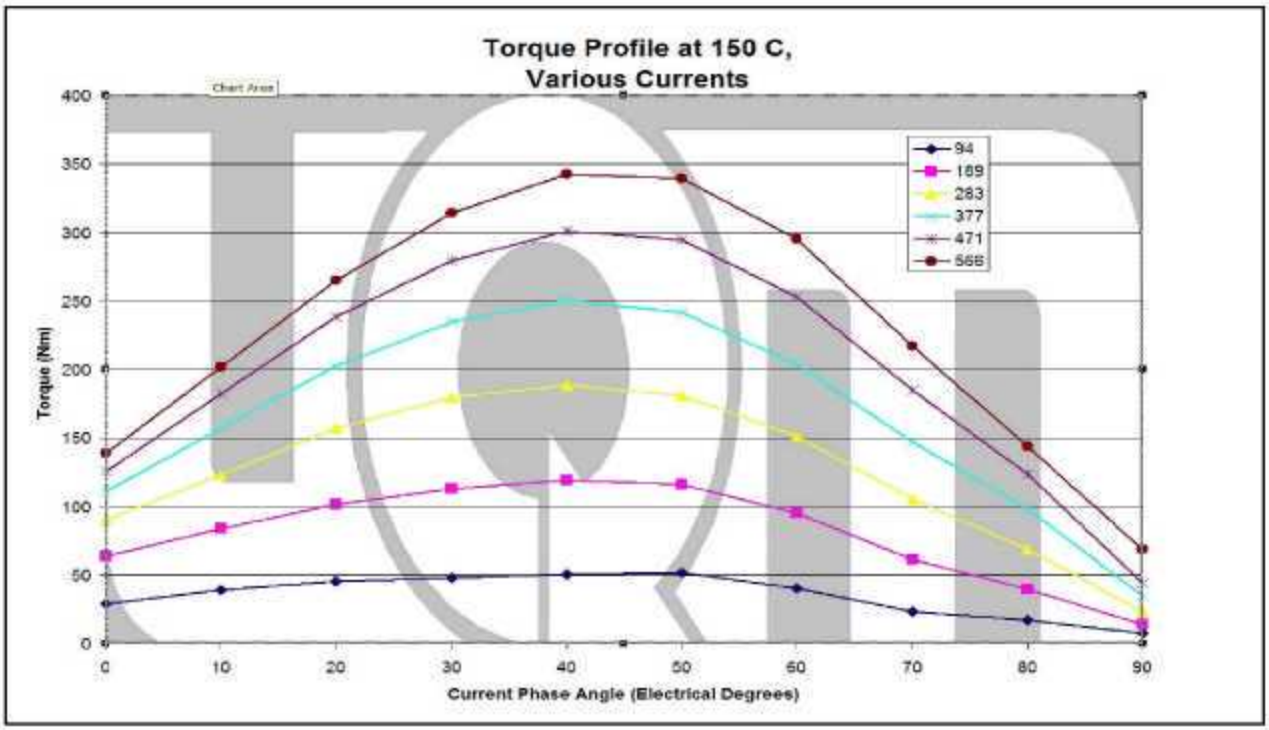


**Fig. 54. Final design torque profile.**

## 6.3 INDUCTANCE ANALYSIS

Figure 55 illustrates the relationship of inductance with phase current for each of the q-axis inductance components. The q-axis inductance is more highly affected by magnetic saturation than the d-axis inductance, reducing the amount of reluctance torque available as the current increases. This trend is also evident in the torque profile map in Section 6.2. Notice that as the current increases, the lines of torque get closer together indicating a lower torque value per unit of current. This inductance map is used in the simulations for vector analysis and calculation of the efficiency and losses, along with the torque profile described in the previous section and the other motor parameters.

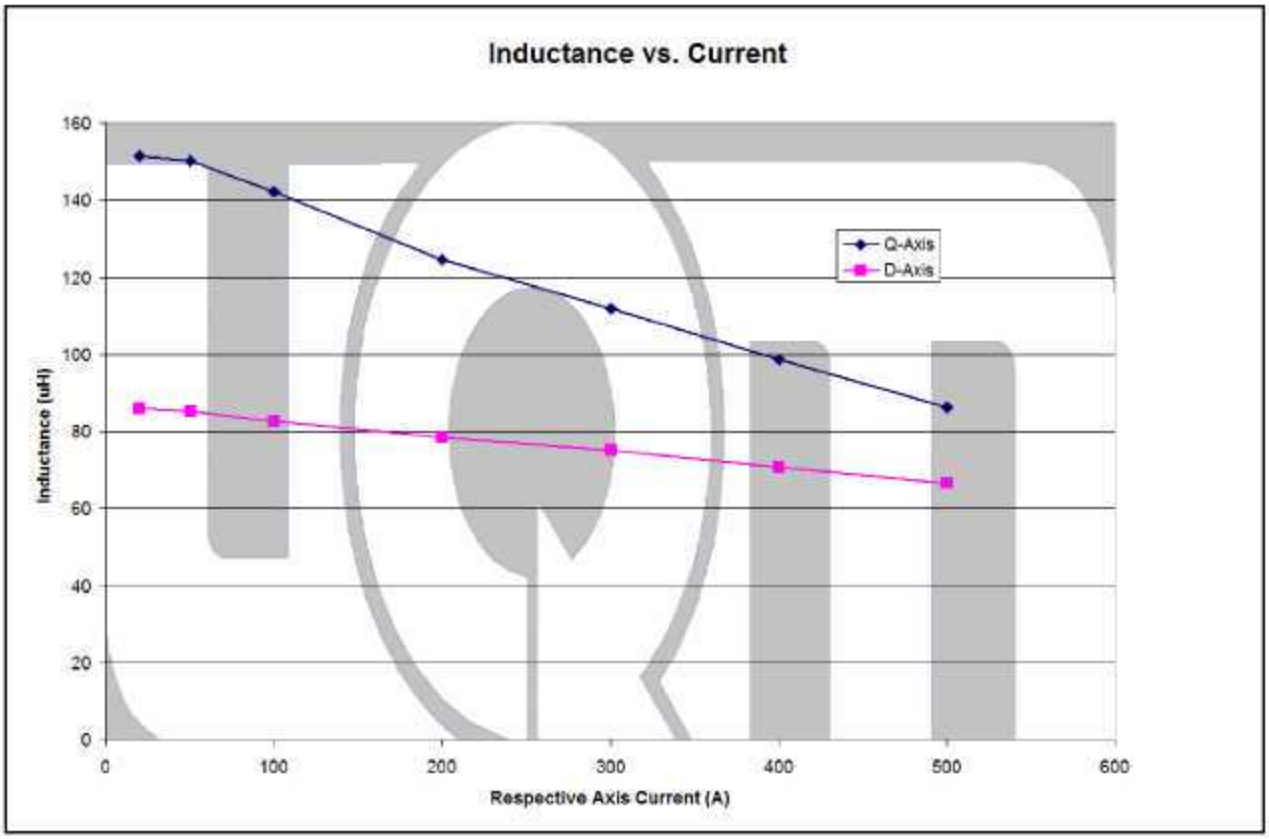


**Fig. 55. Final design, inductance vs. current.**

## 6.4 ACTUAL PEAK POWER

Due to the requirement of the motor to operate down to 200 V at 55 kW, as well as continuous 30 kW operation the resulting final motor design is capable of achieving a higher peak power than required. Figure 56 illustrates the power available from the motor as the base speed is moved up in the speed range. If base speed is moved from 2000–3000 rpm, the motor can achieve 82.5 kW or up to 110 kW at 4000 rpm. Vector analysis shows that 82.5 kW is available down to 200 V, and 110 kW is available down to 235 V. From the motor analysis, it is conclusive that the motor can achieve these power levels intermittently, as long as the power devices in the inverter can supply the input power.

The two requirements that drove the design and allowed much higher intermittent power included the 400 Arms maximum current requirement and the 55 kW (full power) requirements up to 10 krpm with a 200 V buss supply. The 30 kW continuous requirement however, ultimately drove the overall size see Section 6.6.1. It is the 200 V requirement that necessitated low inductance and therefore a low turn count.

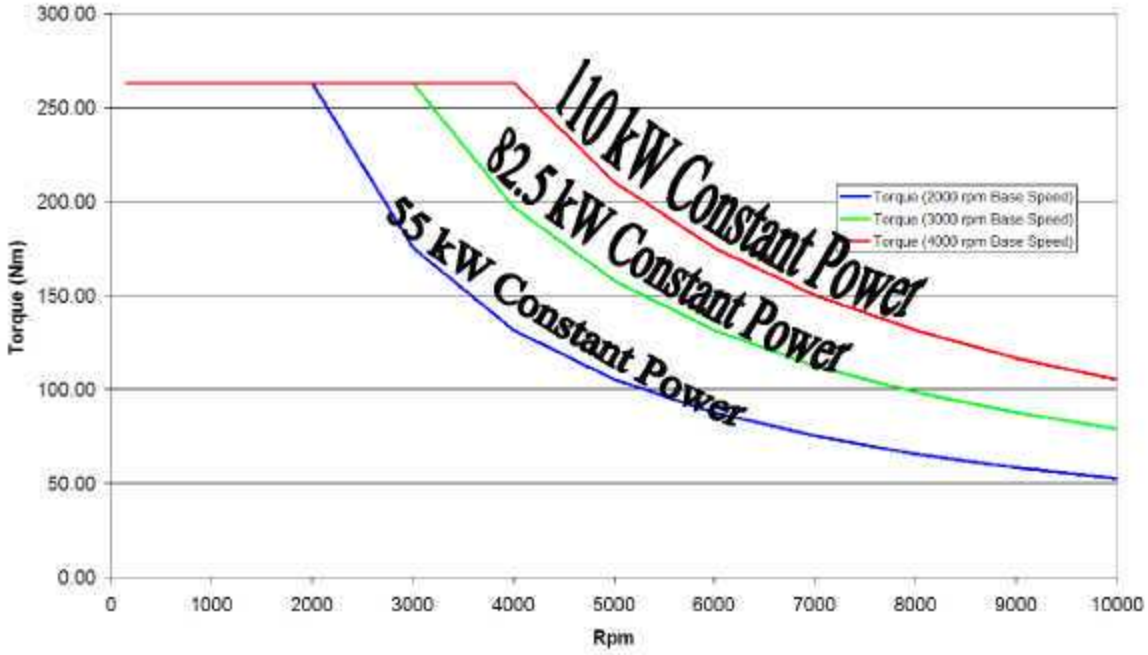


**Fig. 56. Actual peak operating profile.**

## 6.5 STRUCTURAL ANALYSIS

A finite-element structural analysis was completed for the rotor of the final design as it was for several of the design iterations in the rotor configuration study (Section 4.3). One or two poles of the rotor were modeled and a finite-element mesh was distributed across the geometry. Contact elements were added to the inside surfaces of the flux barriers (cutouts in the rotor iron). These contact elements were also added to the outer edges of the magnets. This arrangement simulates the magnets having contact with the edges of the flux barrier when the rotating rotor forces them radially outward. A simulated rotational speed of 10 krpm was induced in the model and the stress field distribution was solved. Figure 57 illustrates the Von Mises stresses across the rotor geometry for the final design. As expected, the highest stress in the rotor occurs at the minimum bridge thickness. The maximum stress is 180 MPa, allowing a 170 MPa margin with respect to the 350 MPa yield strength of the silicon steel lamination material.

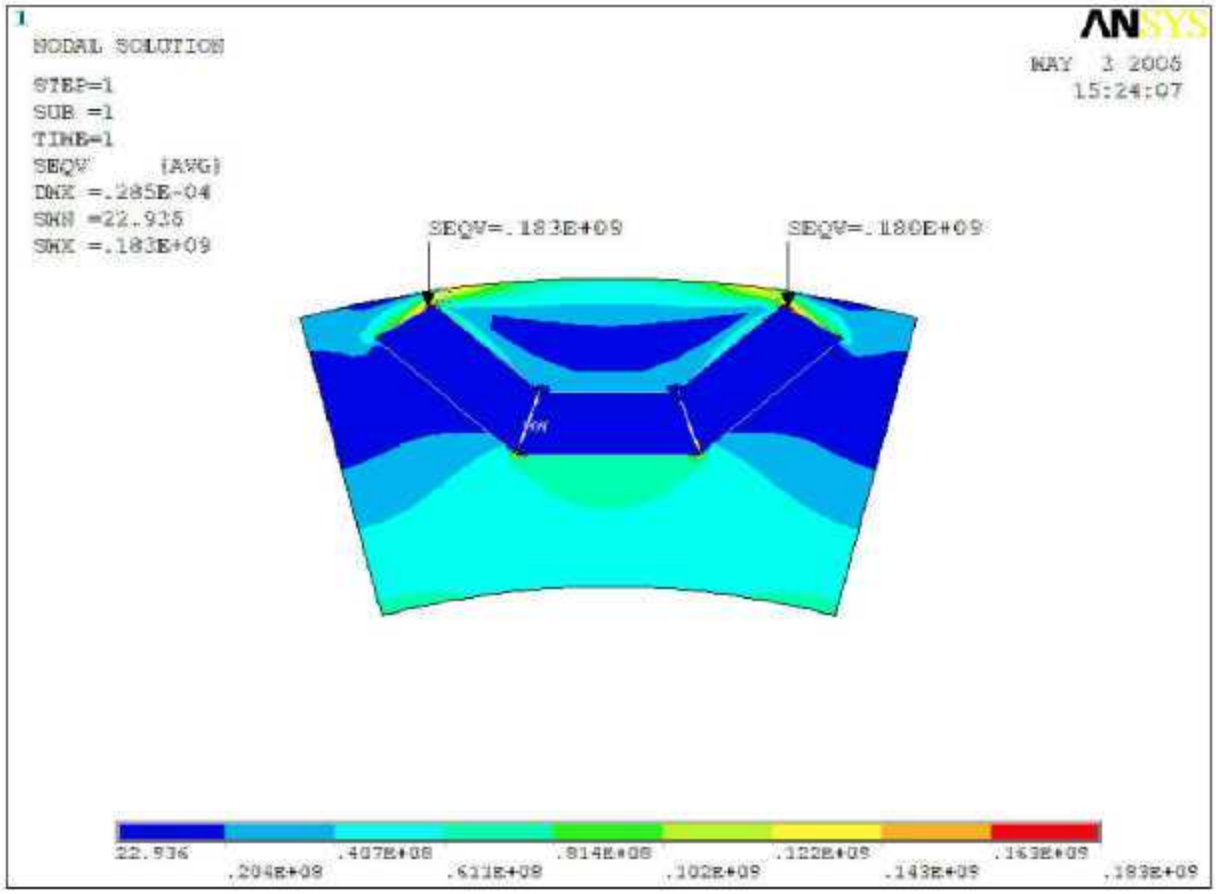


**Fig. 57. Final design, Von Mises stresses, actual deflection.**

The final design employs a bridge thickness that varies across the bridge. The minimum thickness is very small for a 10 krpm design, .04 in. This is possible because of the geometry of the magnets and the non-uniform bridge thickness. The ends of the three magnets are beveled in such a way that the middle magnet locks in place against the ends of the side magnets. The other end of side magnets contact the bridge and distribute the force of the magnets evenly across the bridge where the thicker part of the bridge is forced to carry most of the force from the magnets. This mechanism is illustrated in Fig. 58, where the deflection of the structure is exaggerated in such a way that we can see where deflection occurs. Notice that the magnets do not move against the section of iron between them and the air gap. This is due to the locking mechanism which allows the minor bridge thickness to carry only the force of this iron section and mush less of the magnet weight. It is this structural feature that allows the bridge thickness to be very small such that it can enhance the machine's ability to produce reluctance torque and reduce the shunting of magnet flux.

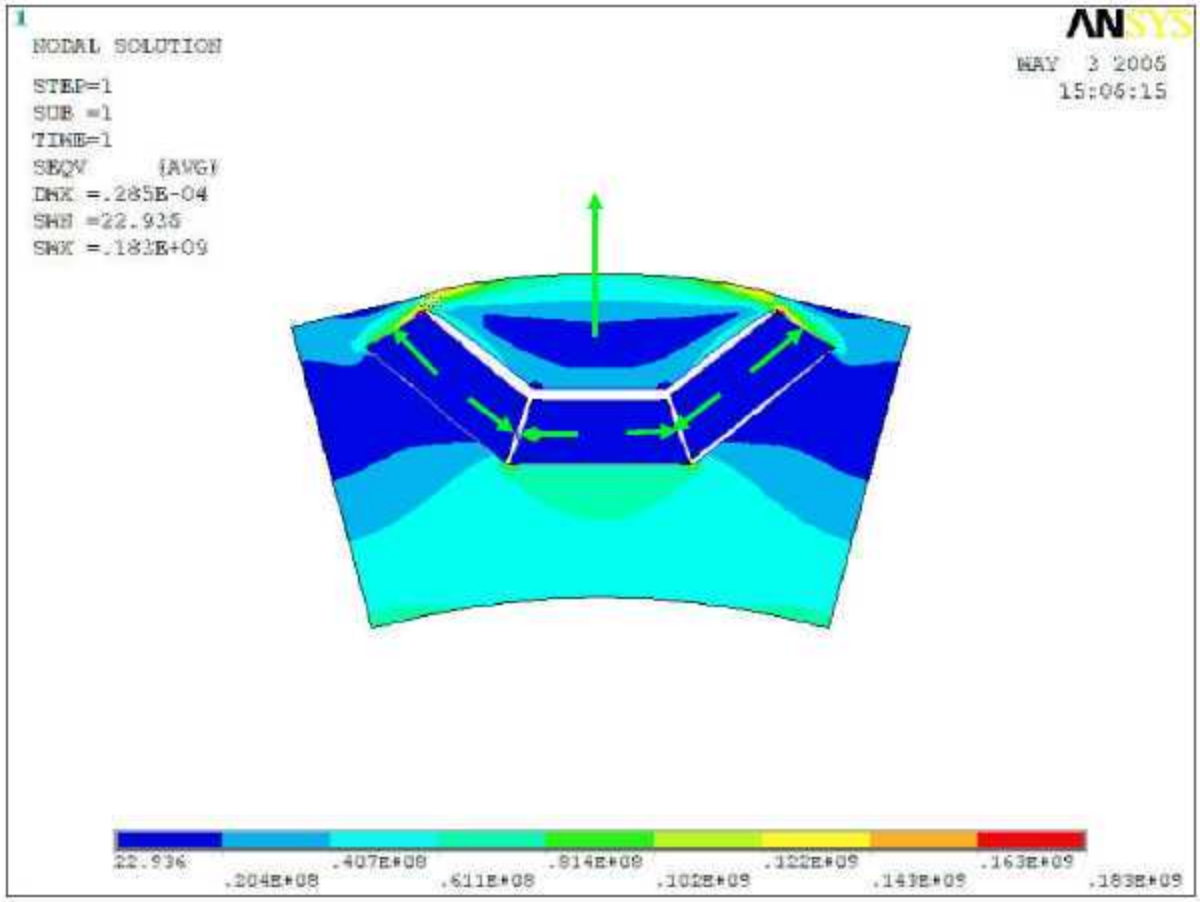


**Fig. 58. Final design, Von Mises stresses, exaggerated deformed shaped.**

Structural adhesive, lining the inner walls of the flux barrier between magnets and iron, is expected to improve the structural rigidity further; however, each of these simulations assume no structural adhesive. Figure 59 shows the Von Mises stresses for a rotor speed of 14,000 rpm, when the stress in the minor part of the bridge approaches the yield strength of the material, 350 MPa. Although the rotor will likely not fail at 14,000 rpm, its strength may be compromised due to possible permanent deformation of the material in these areas.

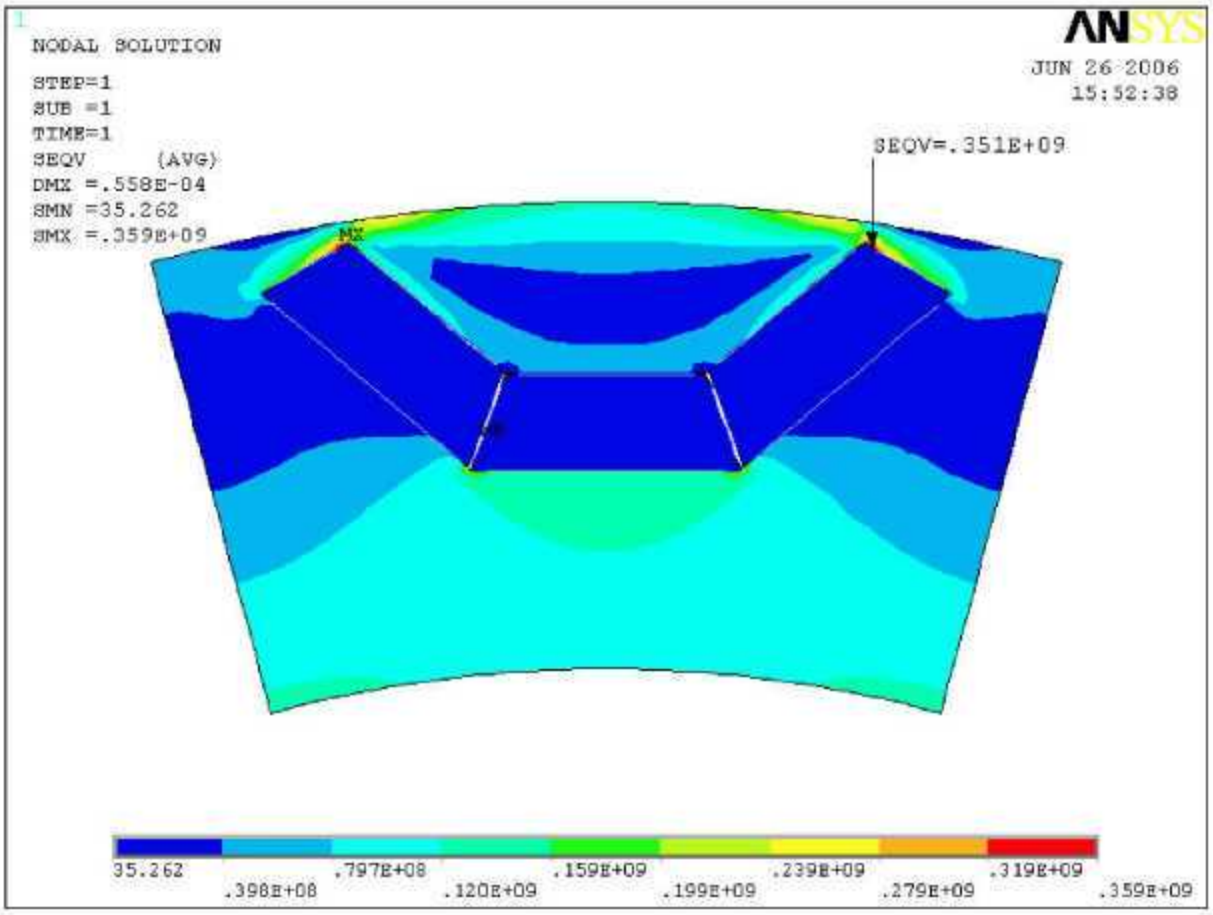


**Fig. 59. Final design, Von Mises stress, spin-to-yield.**

## 6.6 THERMAL ANALYSIS

Thermal analysis was also completed for the final design, to confirm that it is capable of meeting the continuous power requirements and the duration requirement for peak power. The predicted losses and efficiency for the machine were calculated while operating along the continuous operating curve at, 30 kW constant power (Fig. 2) and assuming that the machine is operating at a nominal temperature of 150°C. These losses are applied to the thermal FEA models and the steady state solution is obtained to predict the steady state temperature that the machine would sustain in the given operating conditions. The operating points of interest are at each end of the constant power curve, at 2000 rpm and at 10 krpm and 30 kW. Similarly, to determine how much time the machine can spend at the peak power of 55 kW (Fig. 1), a transient FEA analysis is run with losses calculated at 2000 rpm and 10 krpm at a power level of 55 kW. The requirement for duration at 55 kW is 18 seconds. The ambient temperature in each of the simulations at the inner surface of the water jacket is 105°C. The heat transfer coefficient for the water jacket was calculated to be 1420 W/m^2-k, assuming 105°C water-glycol at 10 liters per minute.

The thermal modeling was conducted assuming a simple water jacket that is thermal fit around the outer diameter of the stator. This cooling configuration would be the most likely choice if the motor is to be implemented in a stand alone configuration. If the motor is to be integrated into a transmission, as has

been common among current HEVs, the motor will most likely be cooled in a transmission fluid or oil bath, with a smaller water jacket only on the side of the motor that sees less oil splash (similar to the current Prius cooling system). UQM chose to simulate the water "jacket only" cooling configuration because we believe this to be a less effective cooling system than an "oil splash" cooling system. Therefore, we believe that the results indicated here are conservative and the continuous power would improve with an "oil splash" type of cooling system.

### 6.6.1 Steady State Thermal Analysis

Figure 60 shows the results of the SS thermal analysis at 2000 rpm and 30 kW. Under these operating conditions, the maximum temperature is reached in the slot of the stator at 149°C. This temperature corresponds perfectly with the temperature at which the losses were calculated; therefore, there was no reason to run a second iteration with losses recalculated at a different temperature.

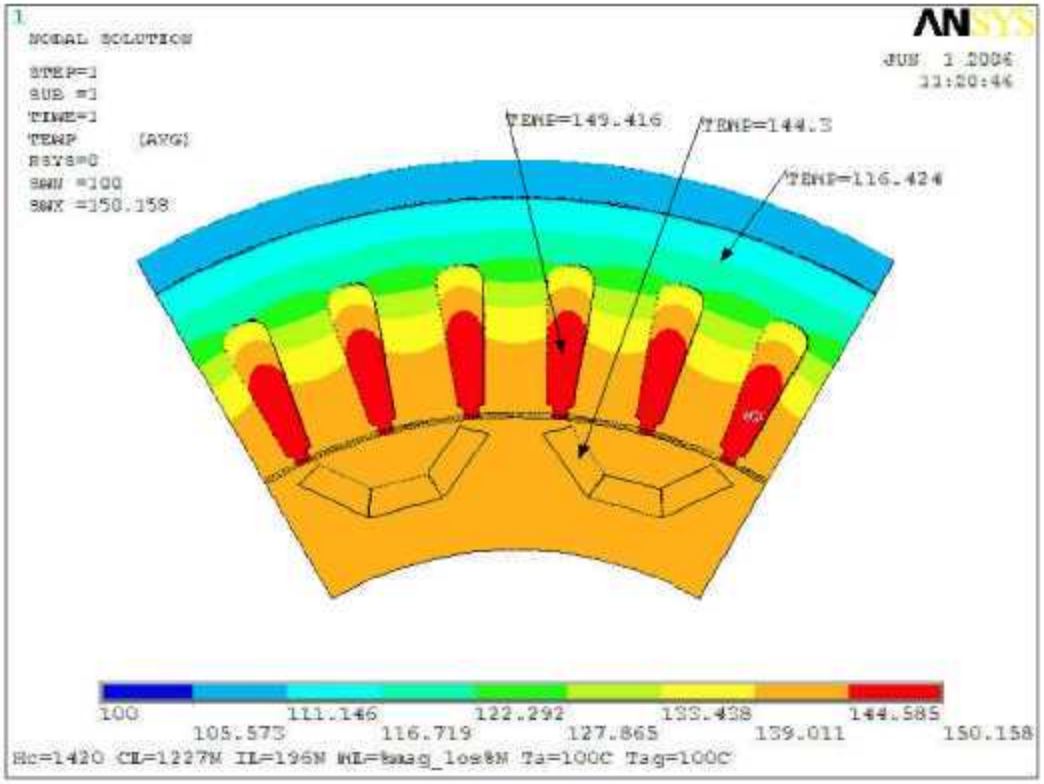


**Fig. 60. Final design, thermal analysis, 30 kW, 2000 rpm.**

Figure 61 illustrates the resulting temperature distribution from FEA at 30 kW and 10 krpm. At this operating point, the rotor and slot sections reached temperatures up to 160°C. Operating at this temperature is also acceptable given the magnet selection in this particular design. See the next section for magnet selection and demagnetization analysis.

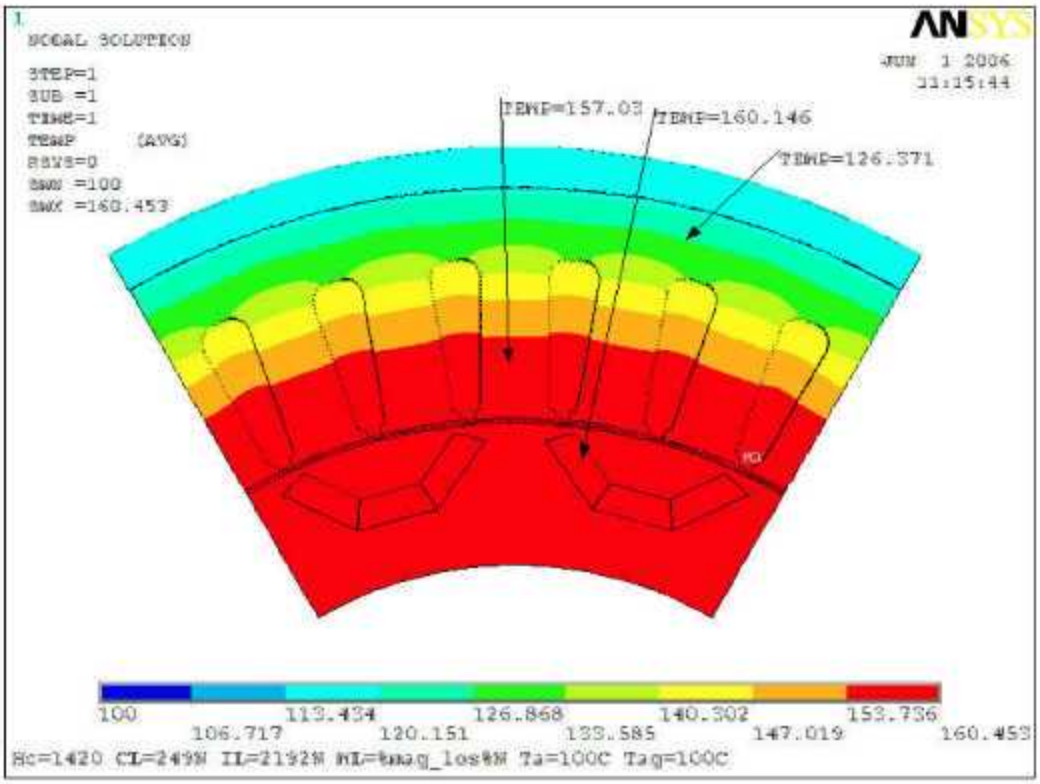


**Fig. 61. Final design, thermal analysis, 30 kW, 10,000 rpm.**

### 6.6.2 Transient Thermal Analysis

The results for the thermal transient analysis for 2000 rpm and 55 kW are displayed in Fig. 62. The analysis started with all components at 20°C and an ambient temperature of 105°C at the outer surface. The load losses were step applied at time equals zero seconds. From the figure, it can be seen that the stator winding temperature is the gating factor. Starting at 20°C, it takes 140 s for the stator windings to reach 160°C and it takes 180 s to reach 180°C. The steady state analysis suggested that the average operating temperature will be between 150°C and 160°C. This analysis indicates that it will take at least 40 seconds (180 s–140 s) to go from the average operating temperature to the absolute maximum temperature, indicating that full power is available for more than 18 s as specified in the requirements.

Therefore, for an excursion to 55 kW at 2000 rpm from an operating temperature of 160°C, requires a maximum operating temperature of about 180°C. To ensure a safe 20°C margin from demagnetization, a magnet will need to operate up to 200°C before permanent demagnetization takes place.

Similar to the 2000 rpm transient analysis at 10 krpm (Fig. 63), analysis indicates that an excursion to peak power for over 18 s is achievable. Starting at 20°C, it takes over 600 s for the stator windings to reach 160°C. Although the temperature has not stabilized after 600 s, it is apparent that the steady state temperature will be somewhere close to 160°, as it was for 30 kW and 10krpm. This is reasonable because the difference in total losses is only 100 W.

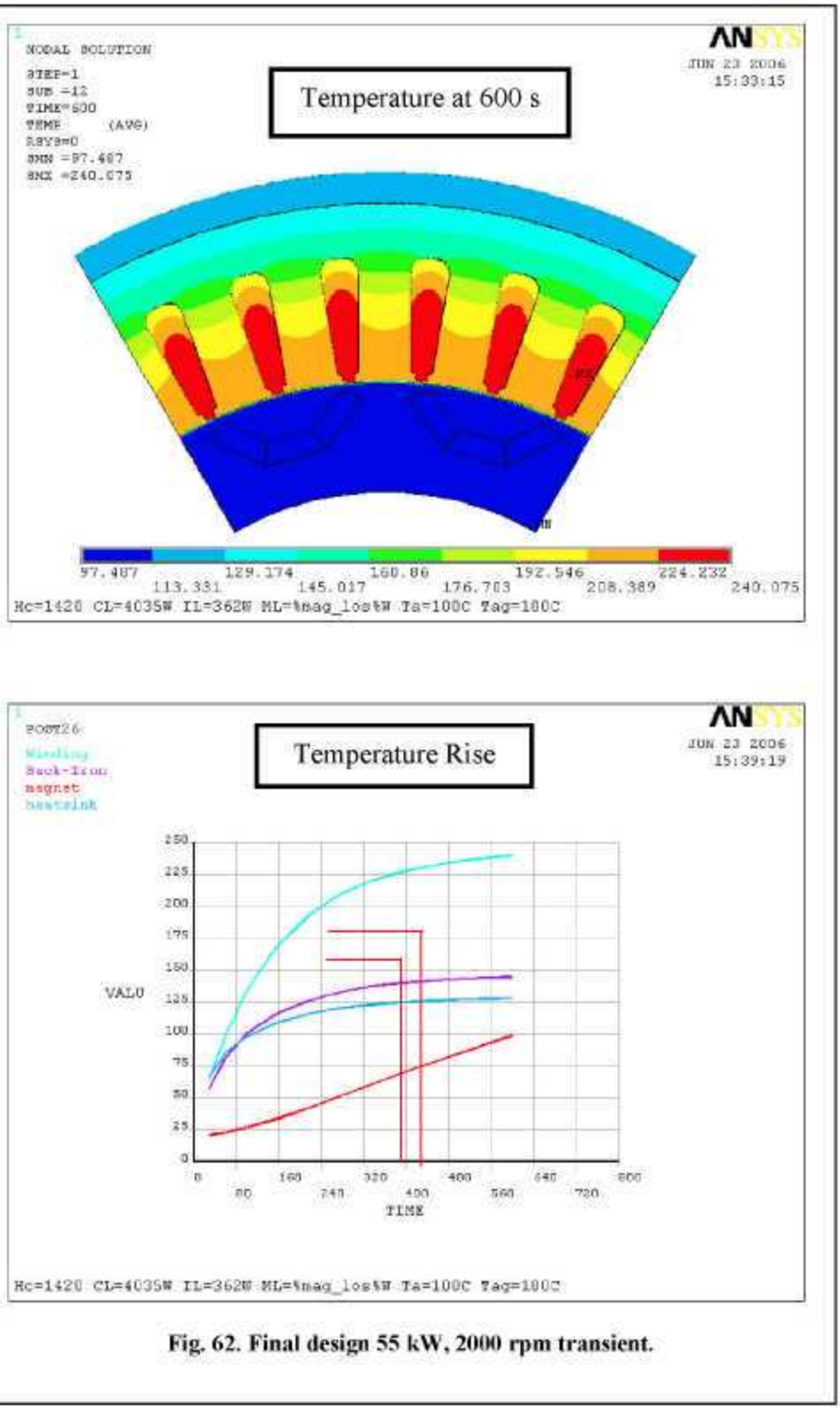


**Fig. 62. Final design 55 kW, 2000 rpm transient.**

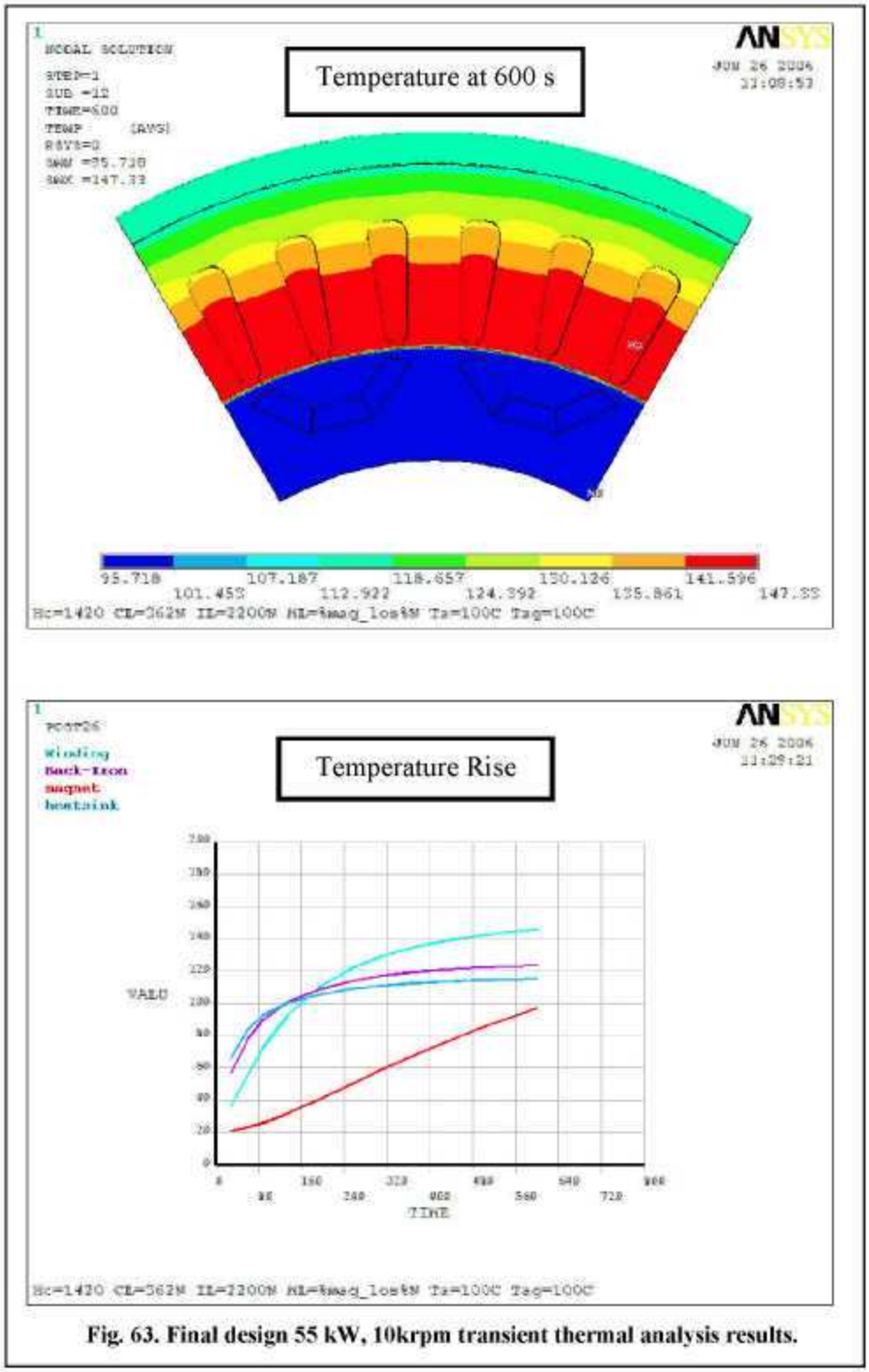


**Fig. 63. Final design 55 kW, 10krpm transient thermal analysis results.**

## 6.7 DEMAGNETIZATION ANALYSIS

The first step in the demagnetization analysis is to determine the flux density in the magnet under no load condition, with no current in the windings. Figure 64 illustrates the flux-density plot for the no load condition. The magnets are the only magnetic flux generating components in this simulation. Results indicate that the magnet flux density is at about .92 T as installed in this motor design. Next, this flux density, .92 T, is plotted on the 20°C demagnetization curve in Fig. 66. This point is taken at no load or with no external field adding or detracting from the magnet field; therefore, a line can be drawn between this line and the origin, indicating the path which the magnet flux density would travel as it goes up and down in temperature at no load.

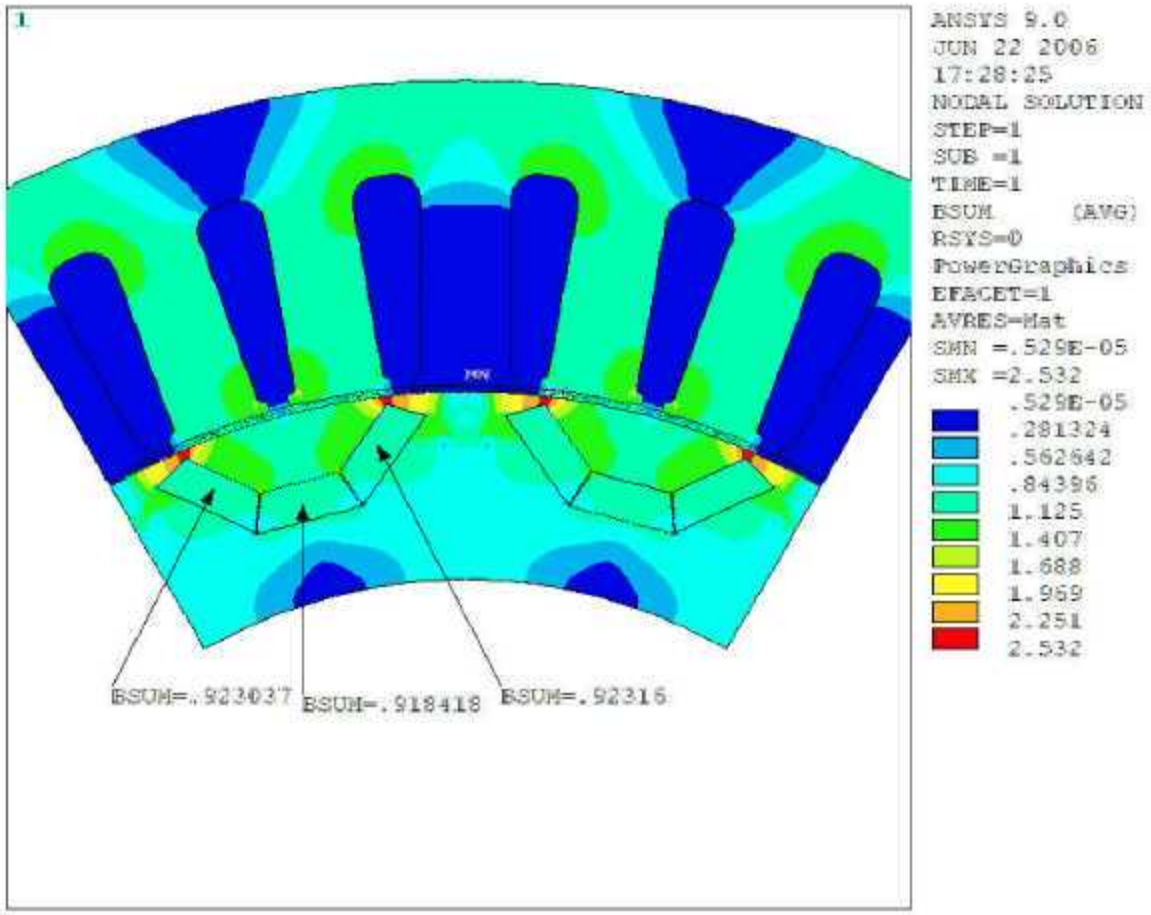


**Fig. 64. No load magnet flux density for demag analsis.**

Under load or when there is current traveling through the winding, there is an external field being applied to the magnet. This field can act to either weaken or strengthen the magnet flux. In this case we are interested in the worst case in which the magnet flux is weakened. Therefore, at full power and 90° of phase advance, another flux-density plot was generated and the magnet flux density was evaluated

(Fig. 65). Since this model was solved with the magnet flux density corresponding to 20°C, this flux-density point is also plotted on the 20°C curve. Next, a line is drawn through this point and parallel to the no load operating line. This is the red line in Fig. 66. Note that the flux-density drops drastically with high levels of phase advance current. Now the red line indicates the different levels of magnet flux density at this operating point, as the magnets vary with operating temperature. Note that most of the demagnetization curves are straight lines that slope toward the negative y-axis. Some of the higher temperature lines curve at the end. This indicates operating points where permanent demagnetization will occur. If the red line crosses one of the demagnetization lines after the curve, permanent demagnetization will occur and the motor should not be operated at this temperature.

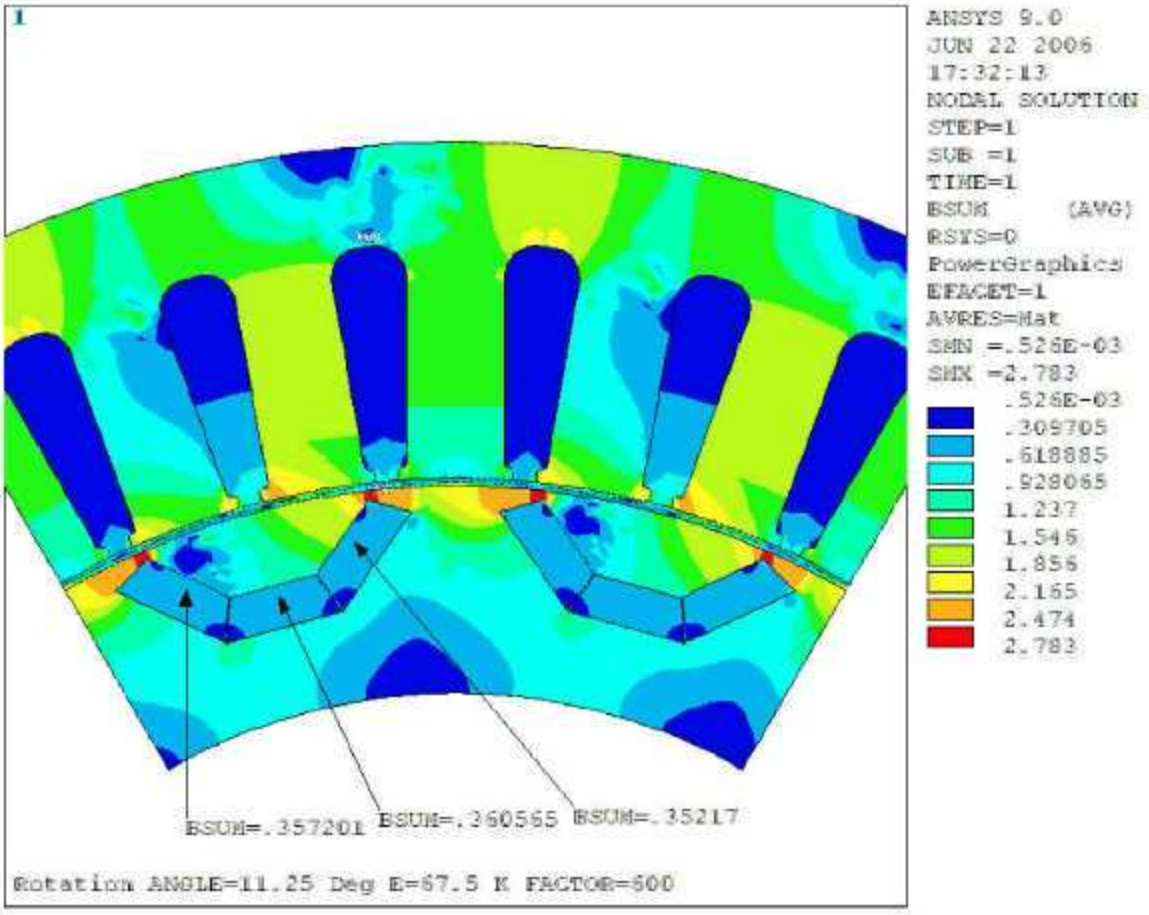


**Fig. 65. Worst case magnet flux density for demag analysis.**

Figure 66 illustrates a demagnetization curve from a Japanese magnet manufacturer that would be appropriate for this design. It has a magnet remanence of 1.11T at 20°C. Analysis of the final design was completed assuming a magnet with 1.10 T flux density at 20°C. Also, it can be seen that the red line crosses the 200°C demag curve just before it starts to bend, indicating that after 200°C, the magnet will begin to experience permanent demagnetization. This is also appropriate for this design because the steady state operating temperature is set between 150 and 160°C. Short excursions to 180°C would also be allowable with this magnet, as a 20 °C margin between absolute demagnetization temperature should be maintained.

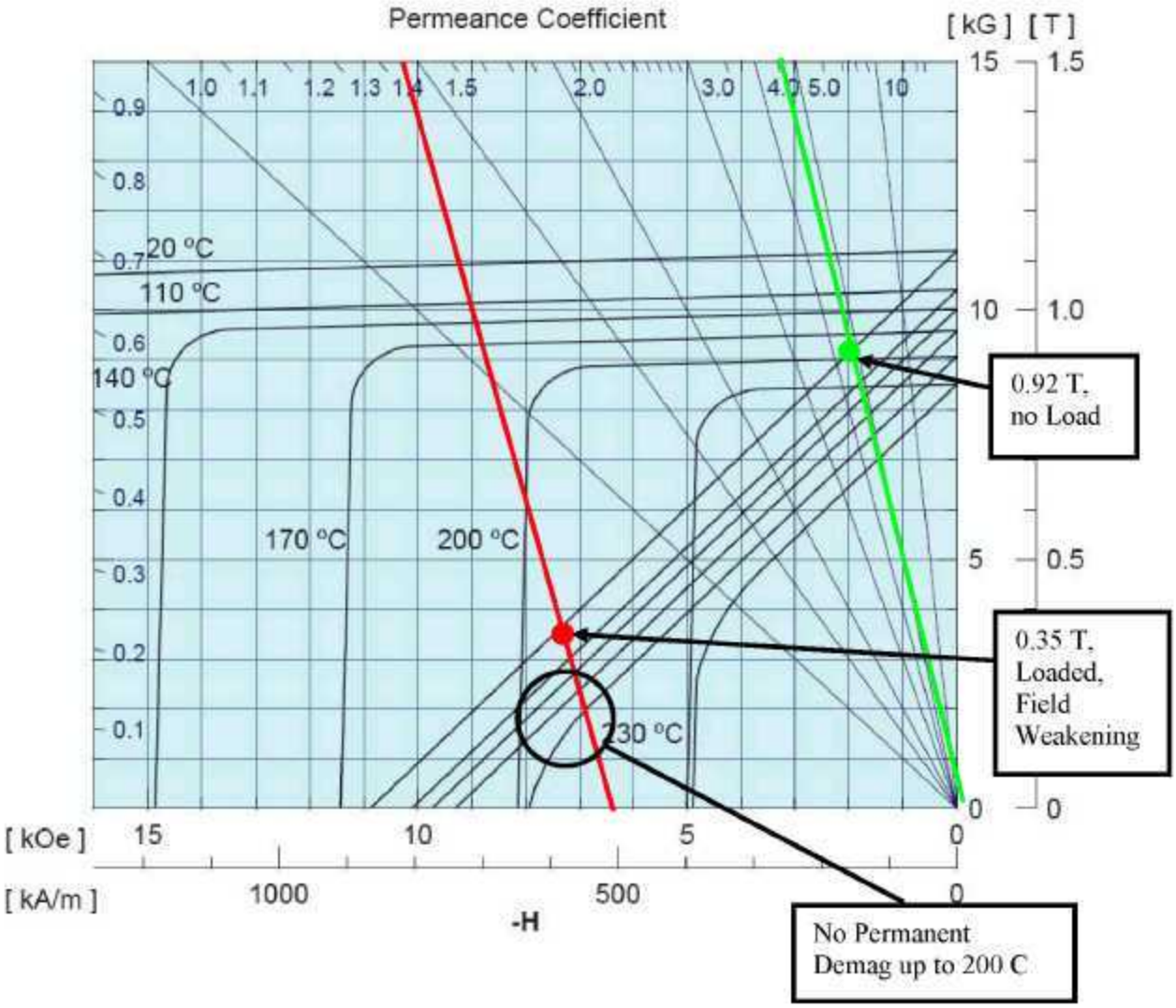


**Fig. 66. 32 MGOe Japanese magnet MFG, demagnetization curve.**

Figure 67 is a demagnetization curve for a 28 MGOe magnet material from a Chinese manufacturer. This material would also be appropriate for the design although it has a slightly lower magnet strength, 1.06T. Using the same analysis technique described above, the 28 MGOe magnet was also found to be capable of up to 200°C operation without permanent demagnetization. These two magnet materials represent two of many different magnet material options capable of 200°C operation on the market place today.

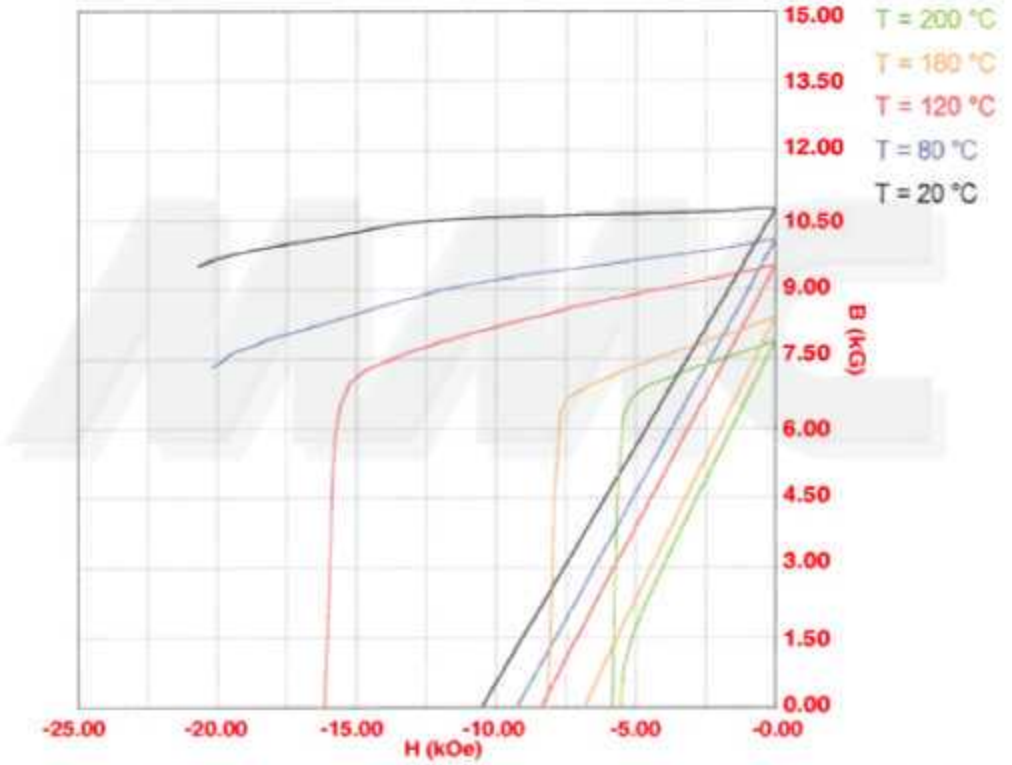


| Grade | $(BH)_{max}$ | | $B_r$ | | $H_c$ | | $H_{ci}$ | | $B_d$ | $H_d$ | $T_c$ | $T_w$ |
|---|---|---|---|---|---|---|---|---|---|---|---|---|
| | MGOe | $kJ/m^3$ | kG | mT | kOe | kA/m | kOe | kA/m | %/°C | %/°C | °C | °C |
| N28EH | 26-29 | 211-236 | 10.60 | 1060 | >9.8 | >784 | >30 | >2400 | -0.11 | -0.51 | 350-380 | 200 |

ALL SPECIFICATIONS ARE SUBJECT TO CHANGE WITHOUT NOTICE

**Fig. 67. 28 MGOe Chinese magnet MFG, demagnetization curve.**

## 6.8 COMPARISON WITH PRIUS MOTOR

The Prius motor is held in high regard in the industry and probably considered state-of-the-art in terms of electric propulsion for hybrid electric cars. For this reason, it makes sense to compare the motor design developed in this program to the Prius's benchmark, in order to determine the value in continued development of this motor design. Since materials represent the most significant part of the cost in automotive volume production, size reduction is paramount. Table 13 compares some of the major dimension and figures of merit of the two motors. In this section, all comparisons are made at the active materials level. Note that overall diameter and length are greatly reduced in the FCVT design over the Prius motor design. Overall diameter of the Prius motor is 10.6 in. but the FCVT design is only 8.7 in. The FCVT design is nearly 2 in. smaller in diameter and down from 6.29 to 5.14 in. in overall length. Also, the reduction in the volume of the FCVT design is approximately 40%, and weight is reduce by nearly 50% from the Prius motor. Some of this size reduction is due in part to the difference in operating profiles of the two motors. The FCVT design makes more power, 55 kW as opposed to 50 kW for the Prius motor; however, the Prius motor operates in a lower speed range and produces more torque, 400 Nm at 1200 rpm as opposed to 262 Nm at 2000 rpm for the FCVT motor. Since electric motors scale with torque more closely than with power, it should be noted that the torque density of the FCVT motor design is still 18% higher than the Prius Motor and its power density is 100% higher than the Prius.

The difference in motor parameters between the two machines includes a much higher back-EMF voltage for the Prius motor, 141 as opposed to 48 Vpeak/krpm (see Fig. 68). This gives a maximum voltage of 480 V for the FCVT design and 846 V for the Prius, necessitating a higher inverter voltage rating for the Prius system. On the other hand, the Prius motor would require a lower current rating in for the inverter, having a maximum motor current of 250 A, as opposed to 400 A for the FCVT motor.

**Table 13. Power density comparison (FCVT design vs. Prius motor)**

| | Prius Motor Design | Final Design (in progress) |
|---|---|---|
| Peak Power | 50 | 55 |
| Peak Torque (Nm) | 400 | 262.5 |
| Overall Diameter (in) | 10.6 | 8.7 |
| Rotor Inner Diameter (in) | 4.356 | 3.04 |
| Rotor Outer Diameter (in) | 6.315 | 6.04 |
| Stack Length (in) | 3.29 | 3.4 |
| Endturn Length (in) | 1.5 | 0.87 |
| Slot Length (in) | 1.3 | 0.91 |
| Overall Length (in) | 6.29 | 5.14 |
| Volume* (Liters) | 9.10 | 5.01 |
| Volume** (Liters) | 5.50 | 3.48 |
| Power Density* (kW/Liter) | 5.5 | 11.0 |
| Power Density** (kW/Liter) | 9.1 | 15.8 |
| Torque Density* (Nm/Liter) | 44.0 | 52.4 |
| Torque Density** (Nm/Liter) | 72.8 | 75.4 |
| Stator Weight (lb) | 41.2 | 21.6 |
| Rotor Weight (lb) | 11.4 | 10.1 |
| Magnet Weight (lb) | 2.8 | 2.2 |
| Winding Weight (lb) | 24.1 | 6.6 |
| Total Weight (lb) | 79.5 | 40.5 |
| Total Weight (kg) | 36.1 | 18.4 |
| Specific Power (kW/kg) | 1.4 | 3.0 |
| Specific Torque (Nm/kg) | 11.1 | 14.3 |

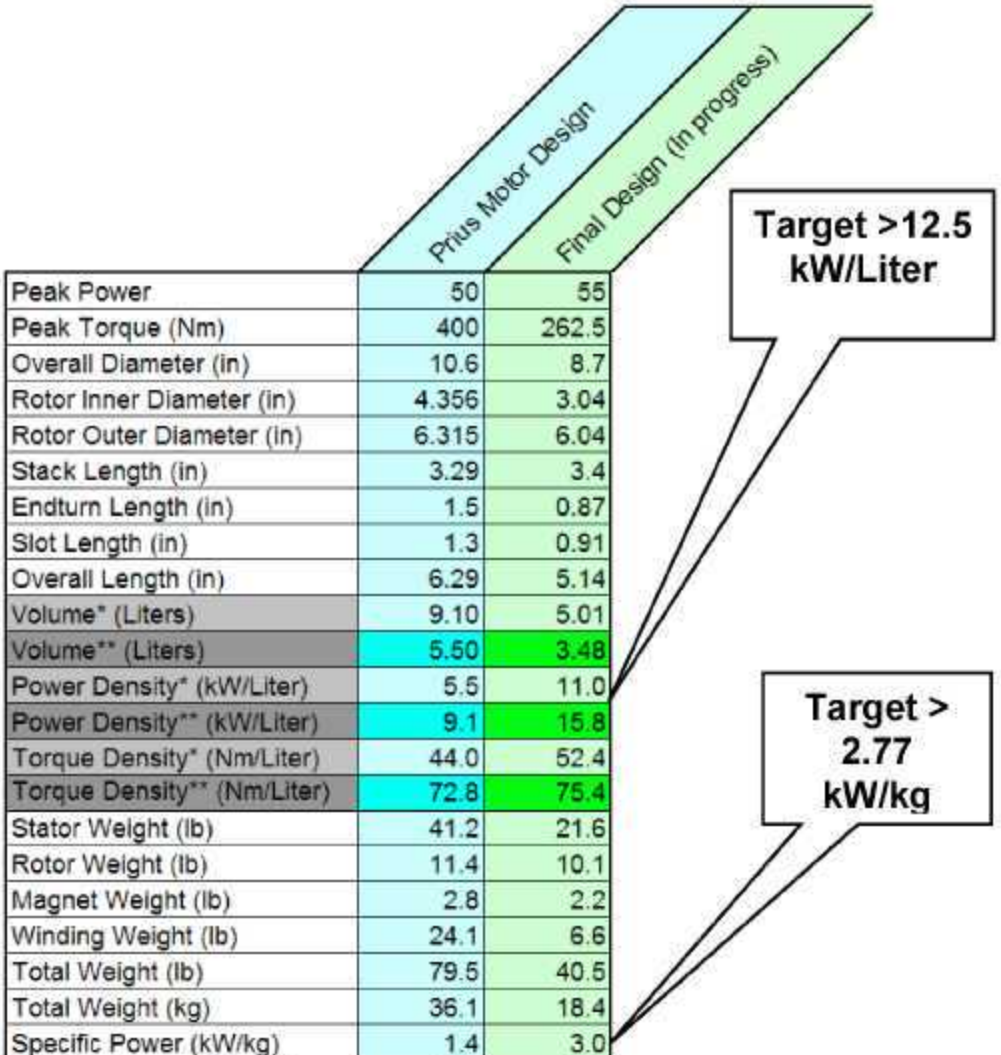


*Utilizes the most conservative method of calculating Volume.
** Utilizes the least conservative method of calculating Volume (see Fig. 4).

| | Prius Motor Design | Final Design (In progress) |
|---|---|---|
| Pole Pairs | 4 | 6 |
| Slots Per Pole | 6 | 3 |
| Back-EMF Constant @ 20 C | 141.7 | 48 |
| Resistance (Ohms L-L) at 20 C | -- | 0.011 |
| Phase Inductance Lq (uH)* | -- | 111 |
| Phase Inductance Ld (uH)* | -- | 75 |
| Saliency Ratio | -- | 1.48 |
| Slot Fill Factor | 0.84 | 0.77 |
| Residual Induction (T) | 1.12 | 1.15 |
| Maximum Current (Arms) | 250 | 400 |
| Maximum Speed (rpm) | 6000 | 10000 |
| Minimum Voltage | **200 | 200 |
| Maximum Voltage | 500 | 450 |
| Max Operating Temp (Celcius) | 170 | >180 |
| Magnet Retention Sleeve Required | No | No |
| Flux Barriers | V-Shape | U-Shape |
| Magnet Shapes | Rectangle | Rectangle |

**Boost Converter required to achieve this voltage range

**Fig. 68. Motor parameter comparison (FreedomCAR design vs. Prius motor).**

# 7. PACKAGING DESIGN

After the electromagnetic component design was finished, a complete mechanical packaging design was generated for prototyping purposes and as a model for production in a stand-alone motor configuration. Figure 69 depicts the overall envelope of the motor. The nominal length is approximately 6.6 in. and the diameter is 9.91 in. A few of the packaging design features include:

- Three 1/0 power cables exiting radially from an enclosed termination box.
- Water ports exiting radially with the power leads.
- Non-Adjustable hall effect sensor for rotor position sensing (Software adjustable phasing, FOC from halls).
- Rotor lamination embedded magnets without external magnet retention sleeve.
- Shaft/Bearing system designed for 10 krpm operation.
- Design is fully submersible with optional speedy sleeve and Viton seal at the motor shaft.
- Water/Glycol cooling jacket optimized for heat transfer. Parallel cooling channels add surface area and strength.
- Total Weight is estimated at 70 lbs. 31.7 kg.
- Total Volume is 8.34 Liters, not including termination cover and shaft protrusion.

Figure 70 illustrates a cutout view of the motor design and mechanical packaging configuration such that the part placement can be visualized on the inside of the machine. The exploded view in Fig.71 illustrates how the parts of the motor are assembled.

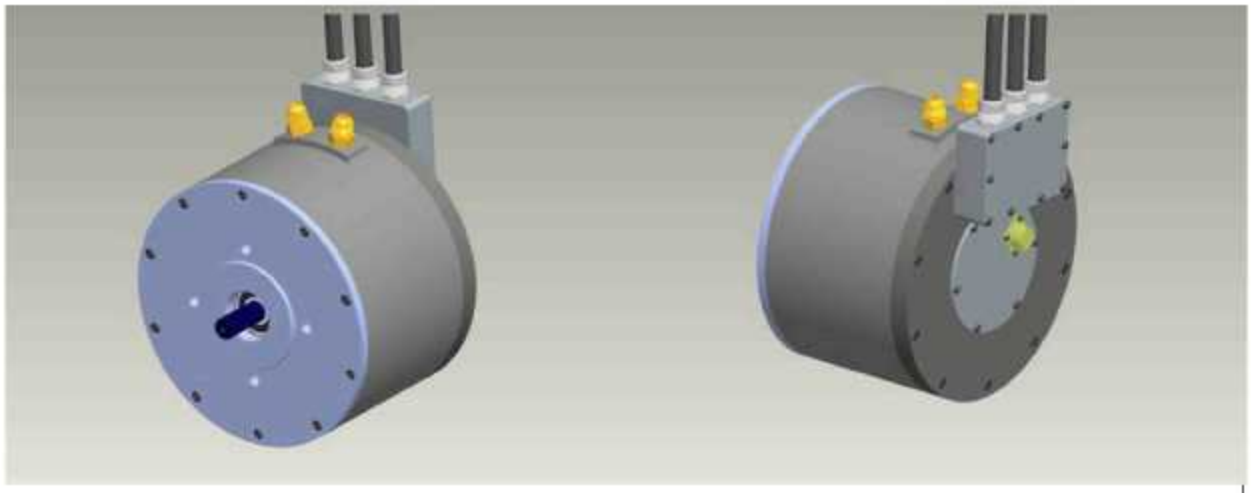

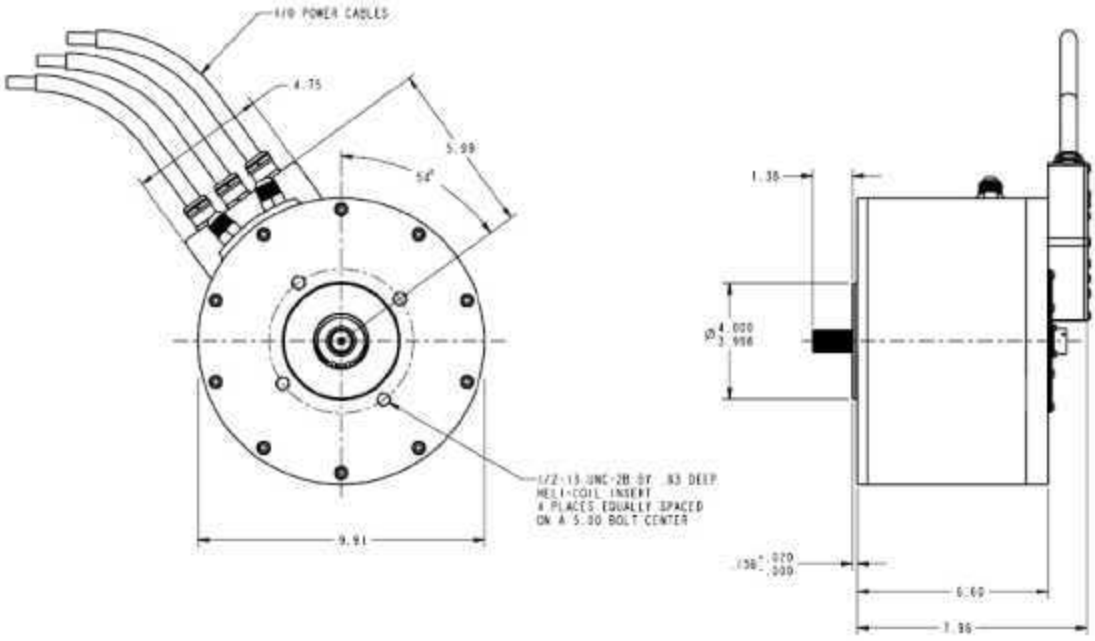


**Fig. 69. Motor assembly outer envelope.**

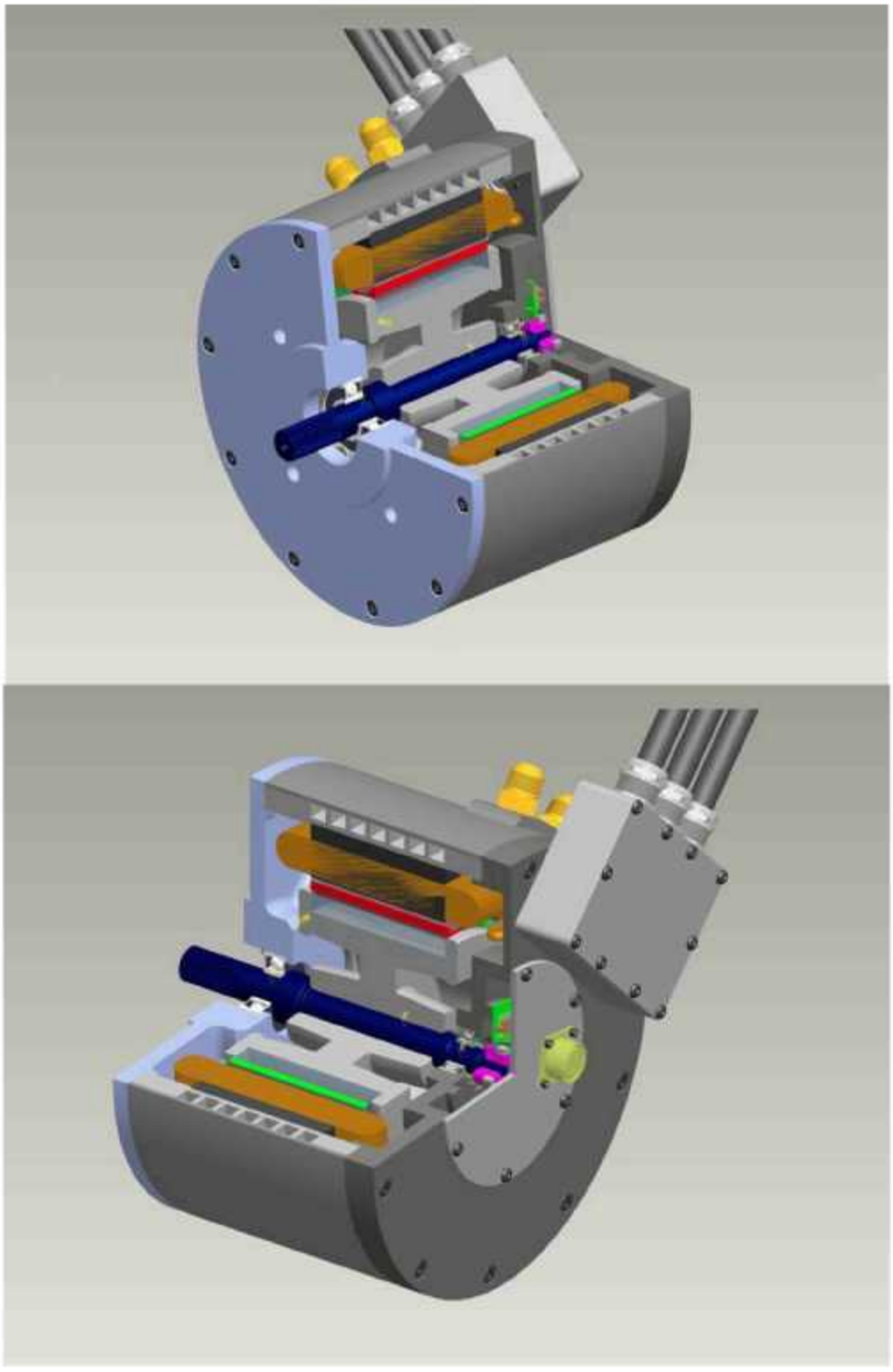

**Fig. 70. Motor assembly, cut-out view.**

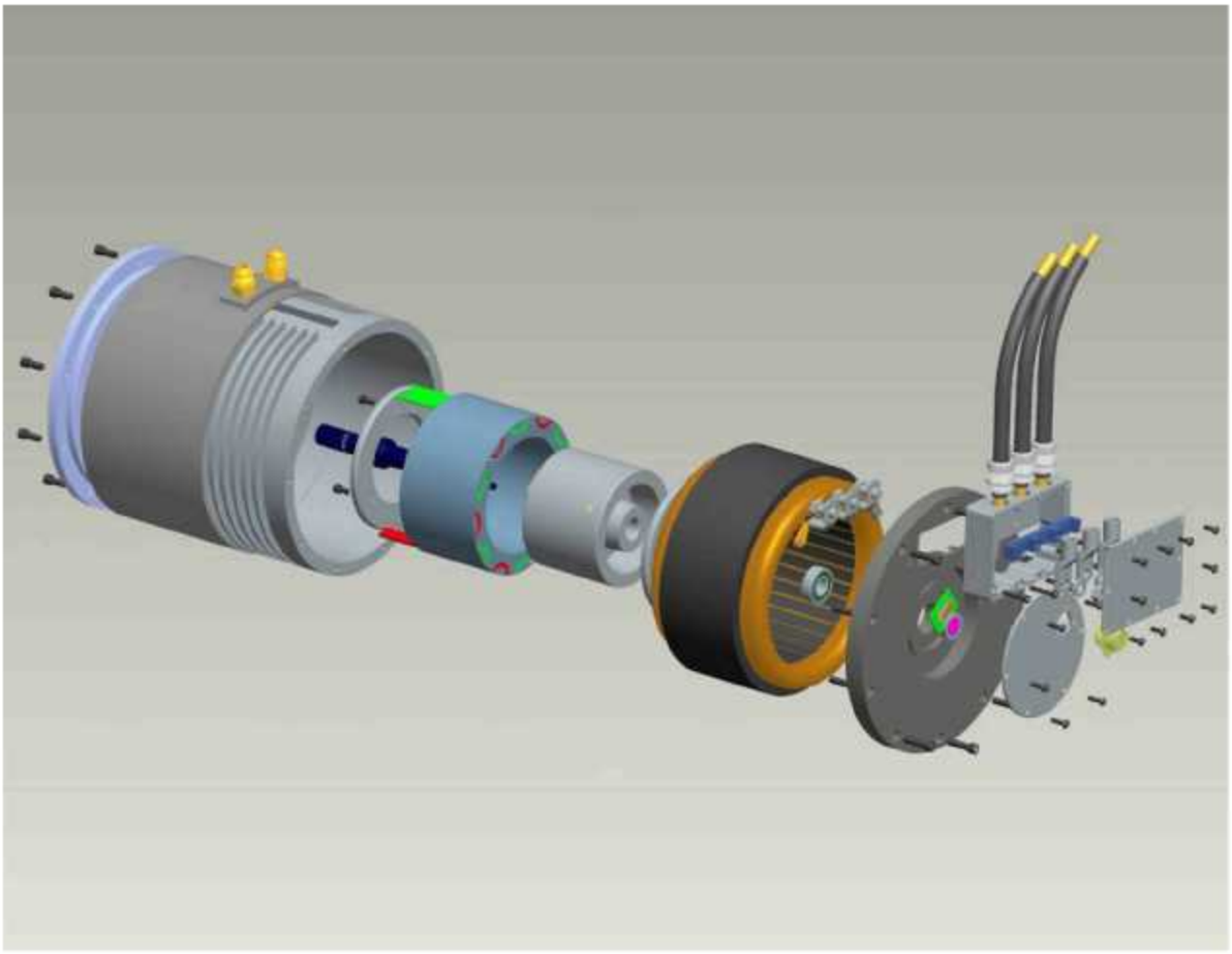

**Fig. 71. Motor assembly, exploded view.**

## 8. MANUFACTURING COST ANALYSIS

UQM chose to estimate the cost of this machine in the most likely automotive production scenario, as a Tier 3 motor manufacturer supplying to a Tier 2 transmission manufacturer. As a result, the gearing cost is not included in the estimate and the housing is at least partially integrated with the transmission as electric machines are presently being integrated in hybrid vehicles. UQM anticipates this transmission – electric machine integration trend to continue and therefore has chosen to estimate cost as a motor manufacturer would supply to the transmission manufacturer. The water jacket or heat sink is considered part of the motor, which will be included in the cost estimate. The water jacket will encompass the outer diameter of the stator laminations and the assembly is pressed in to the transmission housing or bolted to the transmission housing as an attachment. The rotor is expected to be coupled and installed on one of the primary shafts of the transmission. Therefore, a hub which supports the rotor ring will be needed to adapt to the shafting of the transmission. Obviously, exact hardware would be application specific; however, for the purpose of this cost study a conceptual rendition of the applicable motor parts are depicted in Fig. 72. This figure represents a good estimation of the necessary motor parts as supplied to a transmission manufacturer for electric machine integration within a transmission.

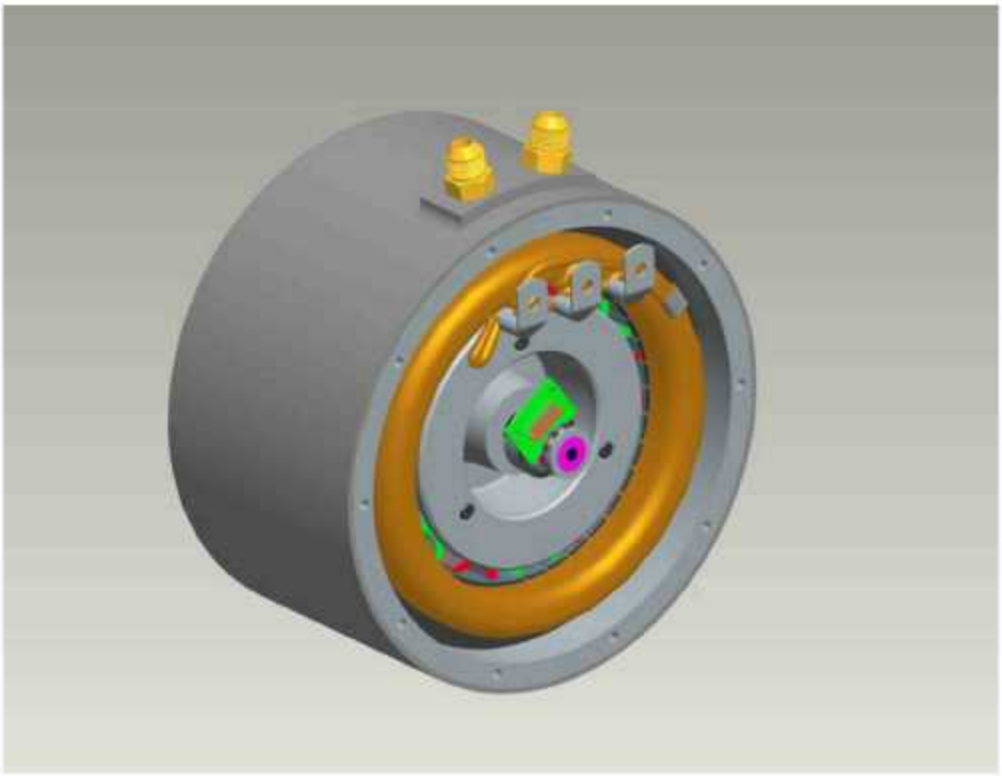

**Fig. 72. Conceptual motor assembly supplied to transmission MFG.**

A list of the parts and their estimated weights that were considered in this manufacturing cost analysis are listed below in Table 14.

**Tabel 14. Parts included in MFG cost estimate**

| Part Description | Weight of Parts/unit (lb) |
|---|---|
| Stator Lamination Stack (243 Laminations) | 21.6 |
| Rotor Lamination Stack (243 Laminations) | 10.0 |
| Magnets NdFeB | 2.215 |
| Winding Magnet Wire (Copper) | 7.0 |
| Bearings | 2* |
| 2 piece housing/water jacket (as Cast) | 5* |
| Stator Finished (Wound and Insulated) | N/A |
| Rotor Hub (as Cast) | 4* |
| Hub Machining | N/A |
| Housing Machining | N/A |
| Circuit Board with Position Sensors (Hall effects) | N/A |
| *Weights that are estimated, not actual values. | |

Material prices for copper, NdFeB, aluminum and other materials were based on current and recent market prices.

The chart below, Fig. 73, illustrates the results of the cost study generated by the UQM manufacturing group. The cost data presented here represents the cost of the motor and does not include tooling amortization or margin. The estimated unit price is $399.60, $299.73, $239.78, and $203.85 at volumes of 100k, 250k, 500k, and 1M per year respectively. The cost target for the 2010 specification was specified in at $7/kW. The chart also graphs the cost data in terms of cost/kW. The red horizontal line represents the cost target. At 55 kW peak power, the cost target is met for all quantities slightly over 100k units per year and above. As explained in Section 6.4, the final design will actually be capable of up to 110 kW peak at nominal voltage and 4000 rpm. Therefore, the cost/kW for the actual peak power is also displayed here. Considering a peak power of 82.5 kW at 3000 rpm the cost/kW is reduced to 4.84 $/kW at 100k and 2.47 at 1M. At 110 kW above 4000 rpm, the cost/kW is reduced well below the target line. For 110 kW peak, the cost/kW is 3.63 $/kW at 100k and 1.85 at 1M.

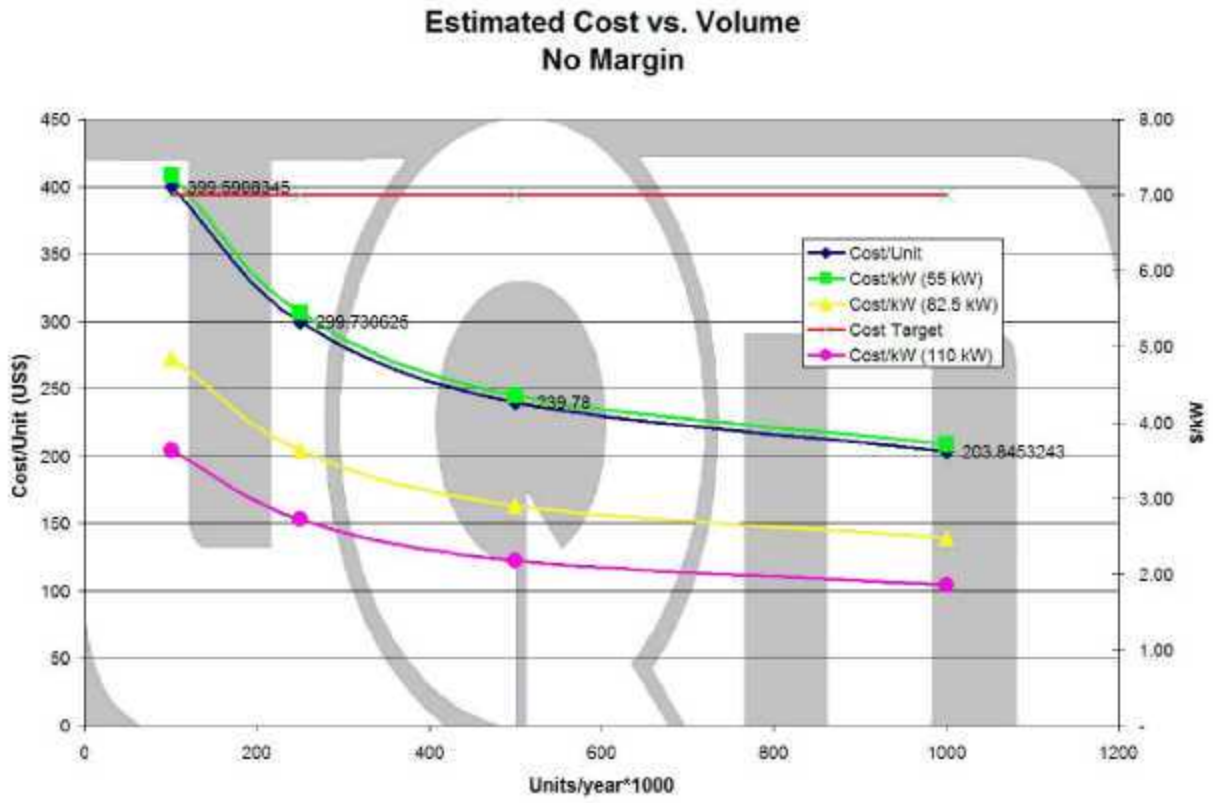


**Fig. 73. Estimatd manufacturing cost in volume.**

The percentage of the total cost for each component for the FCVT design is broken out and illustrated in the Pie Chart in Fig. 74. Note that the top three component costs include the stator lamination stack, 21%, the stator finishing (winding, insulation system and encapsulation), 16%, and the magnets, 14%. Also notice that labor and OH for final assembly are only 6% of the total cost, indicating that material costs are the predominant manufacturing cost. Therefore, reducing size is the foremost key to cost reduction.

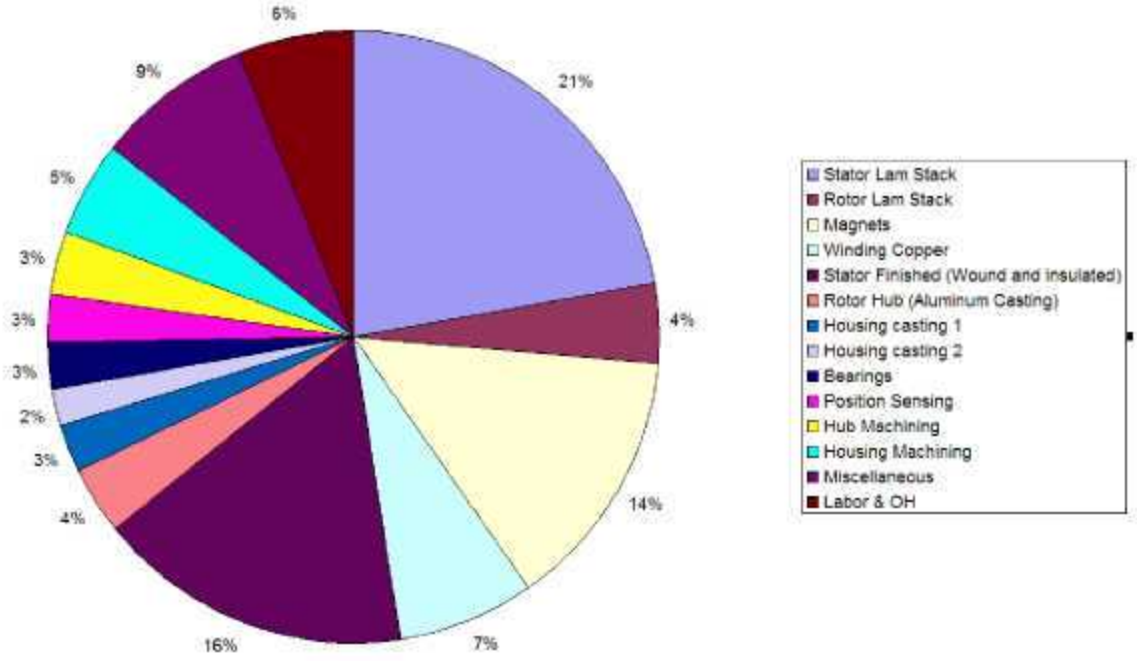


**-Note: This chart is based on 500k/year quantity**

**Fig. 74. Motor component cost percentage.**

The specification in Table 4 also lists the cost targets in terms of the active materials only, the stator core, rotor core, magnets, and windings. The cost target for these components is stated as 3 $/kW. Note that in Fig. 75 that the cost targets are met for the 82.5 and 110 kW peak power lines for all quantities per year above 100k/year. If the peak power is to be based on 55 kW, the cost targets are met at quantities greater than 450k/year. The estimated cost per motor, for the electromagnetic components are $280.47, $210.38, $168.31, and $143.08 for the manufacturing rates of 100k, 250k, 500k and 1M units per year respectively.

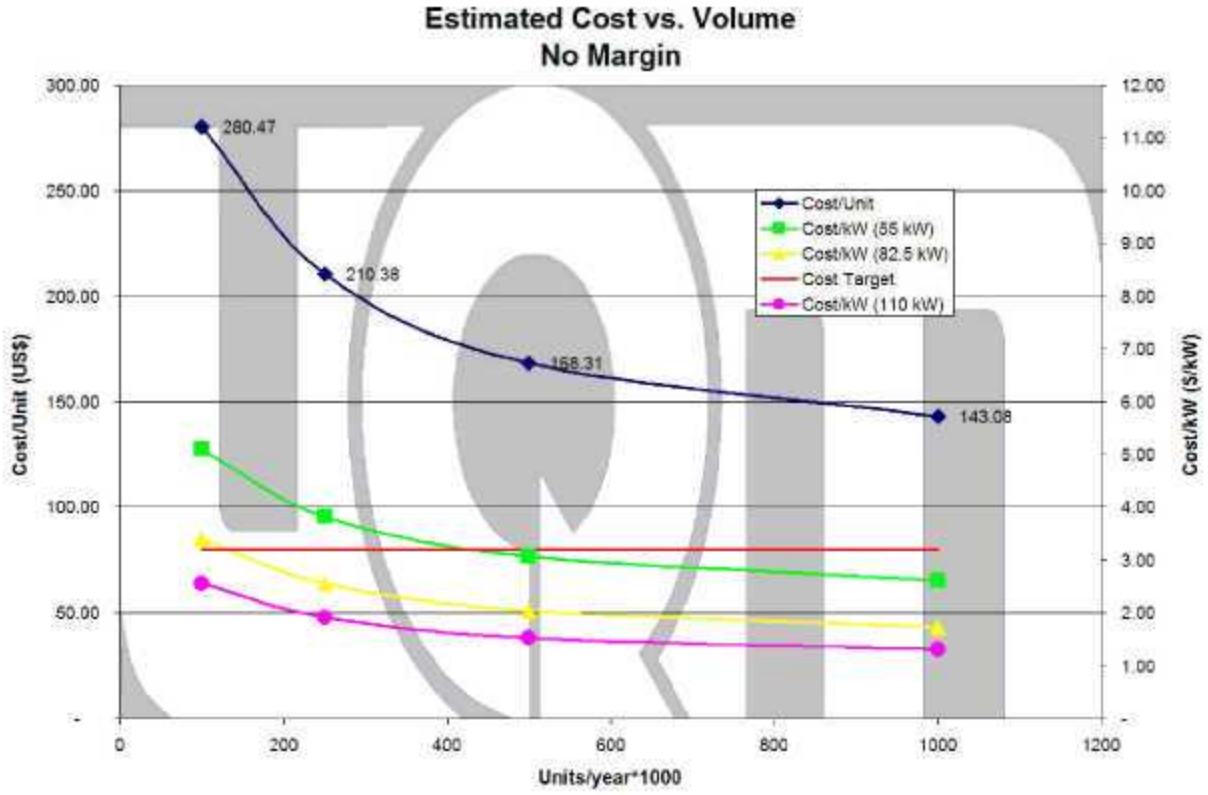


**Fig. 75. Cost vs. volume (active components only).**

## DISTRIBUTION

**Internal**

1. D. J. Adams
2. E. C. Fox
3. K. P. Gambrell
4. J. S. Hsu
5. L. D. Marlino
6. S. C. Nelson
7. M. Olszewski
8. Laboratory Records

**External**

9. T. Q. Duong, U.S. Department of Energy, EE-2G/Forrestal Building, 1000 Independence Avenue, S.W., Washington, D.C. 20585.
10. R. R. Fessler, BIZTEK Consulting, Inc., 820 Roslyn Place, Evanston, Illinois 60201-1724.
11. K. Fiegenschuh. Ford Motor Company. Scientific Research Laboratory. 2101 Village Road. MD-2247. Dearborn, Michigan 48121.
12. V. Garg, Ford Motor Company, 15050 Commerce Drive, North, Dearborn, Michigan 48120-1261.
13. E. Jih, Ford Motor Company, Scientific Research Laboratory, 2101 Village Road, MD-1170, Rm. 2331, Dearborn, Michigan 48121.
14. A. Lee, Daimler Chrysler, CIMS 484-08-06, 800 Chrysler Drive, Auburn Hills, Michigan 48326–2757.
15. J. Ley, UQM Technologies, Inc.; 7501 Miller Drive; Frederick, Colorado 80530
16. F. Liang, Ford Motor Company, Scientific Research Laboratory, 2101 Village Road, MD1170, Rm. 2331/SRL, Dearborn, Michigan 48121.
17. M. W. Lloyd, Energetics, Inc., 7164 Columbia Gateway Drive, Columbia, Maryland 21046.
18. J. Lutz, UQM Technologies, Inc.; 7501 Miller Drive: Frederick, Colorado 80530
19. M. Mehall, Ford Motor Company, Scientific Research Laboratory, 2101 Village Road, MD-2247, Rm. 3317, Dearborn, Michigan 48124-2053.
20. N. Olds, United States Council for Automotive Research (USCAR), nolds@uscar.org
21. J. Rogers, Chemical and Environmental Sciences Laboratory, GM R&D Center, 30500 Mound Road, Warren, Michigan 48090-9055.
22. S. A. Rogers, U.S. Department of Energy, EE-2G/Forrestal Building, 1000 Independence Avenue, S.W., Washington, D.C. 20585.
23. G. S. Smith, General Motors Advanced Technology Center, 3050 Lomita Boulevard, Torrance, California 90505.
24. E. J. Wall, U.S. Department of Energy, EE-2G/Forrestal Building, 1000 Independence Avenue, S.W., Washington, D.C. 20585.
25. B. Welchko, General Motors Advanced Technology Center, 3050 Lomita Boulevard, Torrance, California 90505.
26. P. G. Yoshida, U.S. Department of Energy, EE-2G/Forrestal Building, 1000 Independence Avenue, S.W., Washington, D.C. 20585.